UNIVERSIDAD POLITÉCNICA DE MADRID
Escuela Técnica Superior de Ingenieros de Caminos, Canales y Puertos

Development of 3D-printed biodegradable polymer scaffolds for osteochondral tissue engineering

DOCTORAL THESIS

Submitted for the degree of Doctor by:

Yuyao Liu
Master in Science

Madrid, 2025

UNIVERSIDAD POLITÉCNICA DE MADRID
Escuela Técnica Superior de Ingenieros de Caminos, Canales y Puertos

Doctoral Degree in Engineering of Structures, Foundations and Materials

Development of 3D-printed biodegradable polymer scaffolds for osteochondral tissue engineering

DOCTORAL THESIS

Submitted for the degree of Doctor by:

Yuyao Liu
Master in Science

Under the supervision of:
Prof. Javier LLorca

Dr. Mónica Echeverry-Rendón

Madrid, 2025

Title: Development of 3D-printed biodegradable polymer scaffolds for osteochondral tissue engineering

Author: Yuyao Liu

Doctoral Programme: Engineering of Structures, Foundations and Materials

Thesis Supervision:

Prof. Javier LLorca, Professor, Universidad Politécnica de Madrid / IMDEA Material Institute

Dr. Mónica Echeverry-Rendón, Junior Researcher, IMDEA Material Institute

External Reviewers:

Thesis Defense Committee:

Thesis Defense Date:

Viva la Vida.

Acknowledgement

"Remember that you are an actor in a play determined by the author: if short, then short; if long, then long. If he wants you to act as a beggar, then act even that with excellence, just as a cripple, a ruler or a citizen. Because that is your objective: to act the role that is given to you well. To select the role is up to someone else."

---- *Epictetus*

This thesis was carried out during my PhD between the September 2021 and September 2025 in IMDEA Materials Institute. I am very grateful to every researcher, colleague and friend who has provided me with help and care in my PhD life.

First of all, I would like to thank my supervisor, Dr. Monica Echeverry-Rendon. She is the best supervisor I have ever met, and she is always there to support me. She is a very nice and excellent person who has guided me from a polymer researcher to a biomaterial researcher. I cherish every moment with her, lunch time, coffee time, discussion time, and time in the lab. Without a doubt, she is the person who has been with me the longest and given me the most care and love. She is my supervisor but also my best friend here. No matter how I perform, she always stands by me and helps me fight for my rights and opportunities. Thank you very much, Monica! Secondly, I want to express my thanks to my supervisor, Prof. Javier Llorca, who adheres to the rigorous scientific spirit, carefully analyses my experiments, and gives me a lot of guidance. Also, he gave me a lot of suggestions and care in my personal life. He is the one who is always saying, "Tell me what you want, and I will help you get it". I know he has tried his best for me. Thank you so much, Javier! Then, I would like to say my both of my supervisors look like my parents in my PhD, who are taking care of all my thing! I love them! Also, thanks to my visiting supervisor Prof. Fergal J. O´Brien, who gave me a lot of guidance on my work. I really appreciate the opportunity that he gave me to work in RCSI, which makes me improve a lot in my research and gain a lot of knowledge.

Secondly, thanks to Dr. Juan Pedro Fernández,who gave me a lot of help on my polymer synthesis and really saved me from darkness and loneliness at the beginning of my PhD. Thanks to Guillermo Domínguez, my best friend and brother, who gave me numerous help both research and life and never complain about me (jajaja). He has been with me all the time and never let me alone. He is the most awesome friend in my life. For sure, I cannot express how much grateful I feel to him, sincerely (I almost cried when I put these words). Dr. Jesús Ordoño, my best friend and my forever reviewer No.2, who helped me a lot in my research, and he always had answers or doubts to my numerous questions or research. We have been suffered a tough time together when we started with biodevices, but luckily, we both make it! Also, I cannot express how much grateful I feel to him (I feel bad because of lack of vocabulary. I am crying now). Thanks to Claudio and Marko, who are together with me on my PhD research, gave me meticulous care and detailed guidance. Without them, I cannot make great progress on the osteochondral research. Thanks to both of you to take care of me!

Moreover, I am very grateful to all the people who help me and accompany me during my PhD life. Thanks to Prof. Deyi Wang, Dr. Jon Molina, Dr. Miguel Monclús, Dr. Pedro José Díaz Payno, Vanesa, José Luis, Miguel de la Cruz, Amalia, Manuel, Carlota, Javier García, Jimena... Thanks to my IMDEA friends, Wahaaj, Cillian, Carolina, Ignacio Rodríguez, Jorge Valilla, Marcos, Saumya, Ángela de la Camacha, Viktoriia, Pedro I, Carlos, Oscar, Thomas, Adrián, Nafiseh, Monsur, Mahdi, Ignacio Escobar, Miguel Grande Ráez, José Hobson… Thanks to my Chinese friends, Jun Hu, Shuanglan Du, Wei Shao, Biaobiao Yang, Chenying Shi, Yi Yang, Xiang Ao, Jinyi Huang, Shuai Tang, Yidi Li... Thanks to my RCSI friends, Shan An, Kulwinder Kaur, Giulio, Fransico, Javier, Jack, Bingbing and Arlyng…

Last but not least, I would like to thank the China Scholarship Council (CSC), who supported me to come to Spain and conduct my PhD work. Thank my parents and close friends who always stand behind me.

Thank to myself who did not give up!

Yuyao Liu

Abstract

Osteochondral defects caused by trauma or disease contribute to joint instability, ultimately leading to osteoarthritis. Therapies such as autologous transplantation and microfracture offer potential for osteochondral repair, but limitations remain, including donor shortages, infection risks, and immune rejection. Recent advances in tissue engineering and novel biomaterials have led to promising possibilities for osteochondral scaffolds. Notably, the osteochondral unit consists of the articular cartilage layer and the underlying subchondral bone layer, and the development of novel biodegradable polymer scaffolds with gradient structures and tailored mechanical properties is particularly attractive to enhance the repair efficiency of osteochondral defect.

In this thesis, two biodegradable polymers were investigated, flexible poly (glycerol sebacate) (PGS) and rigid poly(ε-caprolactone)-poly(ethylene glycol)-poly(ε-caprolactone) (PCL-PEG-PCL, PCEC), which were further fabricated into porous scaffolds via 3D printing. To enhance bioactivity, prechondrogenic collagen type I/II-hyaluronic acid (CI/II-HyA) and bone-active collagen type I-hydroxyapatite (CI-nHA) matrices were incorporated into PGS and PCEC scaffolds respectively, to create biomimetic CI/II-HyA@PGS and CI-nHA@PCEC composite scaffolds targeted for the cartilage layer and the subchondral bone layer. The processing, structure, mechanical properties, degradation behaviour of the isolated composite scaffolds as well as of the combined bilayer composite scaffold were systematically characterized. Additionally, the chondrogenic capability of the CI/II-HyA@PGS composite scaffold layer and the osteogenic capability of the CI-nHA@PCEC composite scaffold layer were investigated separately to evaluate the potential of the combined bilayer composite scaffold for application in osteochondral tissue engineering.

Chapter 3 presents the synthesis of PCEC copolymers with tunable mechanical properties and degradation rates. Three different crystallization regimes were found, which significantly affected the mechanical properties and degradation rates depending on PCL/PEG block ratio. Additionally, they presented

cell mitochondrial activities above 70% and cell adhesion of mouse fibroblast L929 cells, indicating good biocompatibility. Moreover, they can be manufactured into 3D-printed scaffolds with controlled microstructure, presenting the potential for applications in tissue engineering.

Chapter 4 studies the processing, structure, mechanical properties, degradation rate, and biological performance of CI/II-HyA@PGS composite scaffold. Porous CI/II-HyA@PGS scaffold exhibited an elastic modulus of 167 kPa, similar to that of native cartilage. Moreover, it maintained structural, mass, and mechanical stability during the initial cartilage regeneration period of four weeks, while degraded linearly over time. *In vitro* biological tests with rat-derived mesenchymal stem cell (MSC) revealed that CI/II-HyA@PGS scaffold displayed effective chondrogenic stimulation.

Chapter 5 examines the processing, structure, mechanical properties, degradation rate and biological performance of CI-nHA@PCEC composite scaffold. It showed a hierarchical porosity, as well as an elastic modulus of 37 MPa, similar to that of native cancellous bone. Additionally, *in vitro* degradation tests in physiological conditions demonstrated its stability during the initial bone regeneration period of eight weeks. *In vitro* biological experiments demonstrated its biocompatibility, osteogenesis and angiogenesis, indicating the ability to enhance bone defect repair.

Chapter 6 investigates the processing, structure, mechanical properties, and degradation rate of bilayer composite scaffold. It showed different compositions and morphologies, as well as a transition of compressive modulus from 0.142 MPa to 46.9 MPa at top and bottom layers, which were similar to the native tissue. Moreover, *in vitro* degradation tests in physiological conditions demonstrated its stability during the initial osteochondral regeneration period of eight weeks.

In summary, a novel bilayer biodegradable polymer scaffold was fabricated for osteochondral tissue engineering. It was made up of a CI/II-HyA matrix incorporated in a soft 3D-printed PGS scaffold as the cartilage layer, and a CI-nHA matrix incorporated into a rigid 3D-printed PCEC scaffold as the bone layer. Comprehensive characterizations revealed that the bilayer composite scaffold

exhibited biomimetic composition and structure, gradient mechanical properties, compatible degradation rate with tissue regeneration, and effective chondrogenesis in top layer and osteogenesis in bottom layer, highlighting its potential for osteochondral tissue engineering.

Resumen

Los defectos osteocondrales causados por traumatismos o enfermedades degenerativas contribuyen a la inestabilidad articular, lo que finalmente conduce a la osteoartritis. Terapias como el trasplante autólogo y la microfractura son las actuales opciones terapéuticas para la reparación osteocondral. Sin embargo, la escasez de donantes, los riesgos de infección y el rechazo inmunológico son una limitación en estos casos. Los avances recientes en ingeniería de tejidos y nuevos biomateriales han abierto posibilidades prometedoras para andamios osteocondrales. La unidad osteocondral está compuesta por una capa de cartílago articular y la capa subyacente de hueso subcondral, y el desarrollo de nuevos andamios poliméricos biodegradables con estructuras en gradiente y propiedades mecánicas adaptadas resulta particularmente atractivo para facilitar su reparación.

Esta tesis desarrolla dos polímeros biodegradables: el flexible poli(sebacato de glicerol) (PGS) y el rígido poli(ε-caprolactona)-poli(etilenglicol)-poli(ε-caprolactona) (PCL-PEG-PCL, PCEC), que posteriormente fueron fabricados en forma de andamios porosos mediante impresión 3D. Para mejorar la bioactividad, se incorporaron matrices de colágeno tipo I/II-ácido hialurónico (CI/II-HyA) precondrogénicas y colágeno tipo I-hidroxiapatita (CI-nHA) osteoactivas a los andamios de PGS y PCEC, respectivamente, para crear andamios compuestos biomiméticos CI/II-HyA@PGS y CI-nHA@PCEC dirigidos a la capa de cartílago y a la capa de hueso subcondral. Se caracterizaron sistemáticamente el procesamiento, la estructura, las propiedades mecánicas y el comportamiento de degradación de los andamios compuestos individuales, así como del andamio bicapa combinado. Además, se investigó por separado la capacidad condrogénica de la capa de andamio compuesto CI/II-HyA@PGS y la capacidad osteogénica de la capa de andamio compuesto CI-nHA@PCEC, con el fin de evaluar el potencial del andamio compuesto bicapa combinada para su aplicación en ingeniería de tejidos osteocondrales.

El capítulo 3 presenta la síntesis de copolímeros PCEC con propiedades mecánicas y velocidades de degradación ajustables. Se encontraron tres regímenes de cristalización diferentes, que afectaron significativamente a las propiedades mecánicas y a las velocidades de degradación, dependiendo de la proporción de bloques PCL/PEG. Además, mostraron actividades mitocondriales celulares superiores al 70% y adhesión celular de fibroblastos de ratón L929, lo que indica una buena biocompatibilidad. Asimismo, pueden ser fabricados en forma de

andamios impresos en 3D con microestructura controlada, lo que demuestra su potencial para aplicaciones en ingeniería de tejidos.

El capítulo 4 estudia el procesamiento, la estructura, las propiedades mecánicas, la velocidad de degradación y el desempeño biológico del andamio compuesto CI/II-HyA@PGS. El andamio poroso CI/II-HyA@PGS presentó un módulo elástico de 167 kPa, similar al del cartílago nativo. Además, mantuvo la estabilidad estructural, de masa y mecánica durante el período inicial de regeneración del cartílago de 4 semanas, mientras se degradaba de forma lineal con el tiempo. Las pruebas biológicas *in vitro* con células madre mesenquimales (MSC) derivadas de ratas revelaron que el andamio CI/II-HyA@PGS estimulaba eficazmente la condrogénesis.

El capítulo 5 examina el procesamiento, la estructura, las propiedades mecánicas, la velocidad de degradación y el desempeño biológico del andamio compuesto CI-nHA@PCEC. El andamió presentó una porosidad jerárquica, así como un módulo elástico de 37 MPa, similar al del hueso esponjoso nativo. Además, las pruebas de degradación *in vitro* en condiciones fisiológicas demostraron su estabilidad durante el período inicial de regeneración ósea de ocho semanas. Los experimentos biológicos *in vitro* demostraron su biocompatibilidad, capacidad osteogénica y angiogénica, lo que indica su capacidad para mejorar la reparación de defectos óseos.

El capítulo 6 investiga el procesamiento, la estructura, las propiedades mecánicas y la tasa de degradación del andamio compuesto bicapa. El andamió presentó diferentes composiciones y morfologías, así como una transición del módulo elástico desde 0.142 MPa en la capa superior hasta 46.9 MPa en la capa inferior, similares a los del tejido nativo. Además, las pruebas de degradación *in vitro* en condiciones fisiológicas demostraron su estabilidad durante el período inicial de regeneración osteocondral de ocho semanas.

En resumen, se fabricó un nuevo andamio polimérico biodegradable bicapa para ingeniería de tejidos osteocondrales. Estaba compuesto por una matriz de CI/II-HyA incorporada en un andamio blando de PGS impreso en 3D como capa de cartílago, y una matriz de CI-nHA incorporada en un andamio rígido de PCEC impreso en 3D como capa ósea. La caracterización exhaustiva reveló que el andamio compuesto bicapa presentaba una composición y estructura biomiméticas, propiedades mecánicas en gradiente, una velocidad de degradación compatible con la regeneración tisular, y una condrogénesis eficaz en la capa

superior y osteogénesis en la capa inferior, lo que destaca su potencial para la ingeniería de tejidos osteocondrales.

Table of Contents

List of Figures

List of Tables

Abbreviations and Acronyms

Acronym	Definition
18S	18S ribosomal RNA
3D	Three-dimensional
ACAN	Aggrecan
AFM	Atomic force microscope
ALP	Alkaline phosphatase
BJ	Binder jetting
BMP-2	Bone morphogenetic protein-2
BP	Bio-printing
$CaCl_2$	Calcium chloride
CAD	Computer-aided design
CD44	Cluster determinant 44
CH_2Cl_2	Dichloromethane
CI/II-HyA	Collagen type I/II-hyaluronic acid
CI-nHA	Collagen type I-nano hydroxyapatite
COL1A1	Collagen type I alpha 1 chain
COL2A1	Collagen type II alpha 1 chain
Ct	Cycle threshold value
DHT	Dehydrothermally
DIW	Direct ink writing
DLP	Digital light processing
DMA	Dynamo mechanical analysis
DMEM	Dulbecco's modified eagle medium
DMSO	Dimethyl sulfoxide
DP	Polymerization degree

D-PBS	Dulbecco's phosphate buffered saline
DSC	Differential scanning calorimetry
EBB	Extrusion-based bioprinting
ECM	Extracellular matrix
EDTA	Ethylenediaminetetraacetic
EG	Ethylene glycol
FBS	Fetal bovine serum
FDA	Food and Drug Administration
FDM	Fused deposition modelling
FESEM	Field-emission scanning electron microscope
FT-IR	Fourier transform infrared spectroscopy
G'	Storage modulus
G"	Loss modulus
GAGs	Glycosaminoglycans
GAPDH	Glyceraldehyde-3-phosphate dehydrogenase
GelMA	Gelatin-methacrylamide
GPC	Gel permeation chromatography
H&E	Hematoxylin & eosin
HA	Hydroxyapatite
HyA	hyaluronic acid
IBB	Inkjet-based bioprinting
LAB	Laser-assisted bioprinting
LBB	Light-based bioprinting
$Mg(OH)_2$	Magnesium hydroxide
MJ	Material jetting
MMP-2	Matrix metallopeptidase 2

M_n	Number-average molecular weight
MSC	Mesenchymal stem cell
MTT	Thiazolyl blue tetrazolium bromide
M_w	Weight-average molecular weight
Na_3PO_4	Trisodium phosphate
NaCl	Sodium chloride
NaOH	Sodium hydroxide
NIR	Near-Infrared
NMR	Nuclear magnetic resonance spectroscopy
OCN	Osteocalcin
OD	Optical density
P/S	Penicillin/streptomycin
PBF	Powder bed fusion
PBS	Phosphate-buffered saline
PCEC	Poly(ε-caprolactone)-poly(ethylene glycol)-poly(ε-caprolactone)
PCL	Poly (caprolactone)
PEG	Polyethylene glycol
PEGDA	Polyethylene glycol diacrylate
PFA	Paraformaldehyde
PGA	Poly (glycolic acid)
PGS	poly (glycerol sebacate)
PLA	Poly (lactic acid)
PLGA	Poly (lactide-co-glycolide acid)
PVA	Poly (vinyl alcohol)
qRT-PCR	Quantitative reverse transcriptase polymerase chain reaction
Ra	Average roughness

RGD	Arginine-glycine-aspartic acid sequence
ROP	Ring-opening polymerization
RUNX2	Runt-related transcription factor 2
SEM	Scanning electron microscopy
sGAG	Sulfated glycosaminoglycan
SLA	Stereolithography
SLS	Selective laser sintering
$Sn(Oct)_2$	Tin (II) 2-ethylhexanoate
T_c	Crystallization temperature
T_g	Glass transition temperature
THF	Tetrahydrofuran
T_m	Melting temperature
UV	Ultraviolet
VE-cadherin	Vascular endothelial-cadherin
VEGF	Vascular endothelial growth factor
VP	Vat photopolymerization
XRD	X-Ray diffraction analysis
ß-TCP	Beta-tricalcium phosphate
ΔCt	Delta Ct
ΔH_c	Crystallization enthalpy
ΔH_m	Melting enthalpy
ΔΔCt	Delta-delta Ct
Đ	Dispersity
η*	Complex viscosity

1. Introduction

1.1. Scaffolds for tissue engineering

Tissues and organs are often subjected to damages caused by trauma, degenerative processes, or congenital abnormalities. Current clinical solutions include autologous transplantation (from the same patient), allogeneic transplantation (from a genetically non-identical donor of the same species), and xenogeneic transplantation (from a donor of a different species). However, these options are significantly limited due to the scarcity of available tissues and organs, as well as the risk of immune system rejection [1]. As an alternative, tissue engineering has emerged as a field that integrates cells, scaffolds, and bioactive molecules to support tissue regeneration. Among these components, scaffolds play a critical role by serving as growth platforms that guide the formation of new tissues [2]. Depending on the specific application, scaffolds can be fabricated from different materials, including metals [3], ceramics [4], polymers [5], or their combinations [6]. An ideal scaffold should simultaneously promote tissue healing and provide mechanical support while gradually degrading as the tissue regenerates, which will ensure that the scaffold fulfils its role as a temporary structure without hindering the native regenerative process.

Most metals are neither biodegradable nor bioabsorbable, limiting their applications in tissue engineering [7]. Among biodegradable metals, Mg presents challenges due to its high reactivity, hydrogen gas generation, and alkalinization of the surrounding environment during degradation, which can compromise the viability of the tissue near the implant [8]. Fe has a slow degradation rate of approximately 20.4 $\mu g/cm^2 \cdot h$ *in vitro* and a high modulus of 200 GPa, both of which fall short of the requirements for native bone tissue repair [9]. Zn, which is the least explored, has insufficient mechanical properties for bone applications (e.g., tensile strength of ~120 MPa and ductility of < 10%) and is prone to creep deformation at body temperature, which can alter the structural integrity of

implants over time [10]. Bioceramics are often used in bone applications due to their excellent osteoinductive and osteoconductive properties. However, their limited biodegradability and the challenges to manufacture complex structures restrict their use as scaffolds, owing to their brittleness and poor processability [11]. In contrast, polymers are widely used in tissue engineering because of their versatility in composition, processing methods, biological compatibility, and controllable degradation rates [12]. Among these, poly (lactic acid) (PLA) is the most commonly used biodegradable material in various applications due to its high strength and biodegradability [13,14]. But the stringent requirements for biological characterization and certification drive up the cost of medical grade biopolymers, limiting market options and making them significantly more expensive than those used in other industries. Thus, there is an urgent need for the development of biopolymers with tunable mechanical, degradable, and biological properties.

In the design of polymeric scaffolds, biocompatibility, biodegradability, and mechanical properties are the main features to be considered. Biocompatibility ensures that the scaffold can perform its function without eliciting toxic or immune responses in the host organism, while biodegradability allows the scaffold to gradually degrade and be replaced by native tissue after fulfilling its function [15]. Together, these characteristics ensure that biodegradable polymer scaffolds do not trigger permanent foreign body reactions and are seamlessly integrated into regenerating tissues. Moreover, mechanical properties, determined by structure and molecular weight of polymers, should be tailored to match the stiffness, strength, and ductility required for native hard or soft tissues [16].

The performance of scaffolds is also heavily influenced by the manufacturing technique, which determines their macro- and micro-structural features. Over the past decades, diverse fabrication technologies have been developed, each tailored to the requirements of materials and target tissues [17]. Traditional manufacturing methods, such as freeze-drying, porogen leaching, melt molding, and phase separation, are cost-effective and suitable for large-scale polymer

processing. Nevertheless, these techniques often result in scaffolds with poor pore accuracy and limited three-dimensional (3D) structural precision [18]. In contrast, additive manufacturing, or 3D printing, offers precise and efficient fabrication of scaffolds with complex structures and multifunctional designs. 3D-printed scaffolds also exhibit highly regular geometries, accurate pore interconnectivity, and resemblance to human tissue structure at both macroscale and microscale [19]. These advantages make 3D-printed biodegradable polymer scaffolds highly promising for applications in tissue engineering.

1.2. 3D printable biodegradable polymers

Biodegradable polymers employed in tissue engineering should exhibit mechanical properties and degradation rates closely aligned with those of target tissues. Regarding their origin, biodegradable polymers used in 3D printing can be broadly categorized as natural or synthetic. Natural polymers, derived from organisms, are valued for their high biocompatibility and biodegradability. Examples include collagen, gelatin, chitosan, alginate, and hyaluronic acid (HyA). Synthetic polymers, produced through chemical synthesis, have the advantages of easy availability, tunable mechanical properties, and controllable degradation rates. Some examples include poly (caprolactone) (PCL), poly (lactic acid) (PLA), poly (glycolic acid) (PGA), poly (vinyl alcohol) (PVA) and polyethylene glycol (PEG). In the following sections, the most common polymers used in tissue engineering that are compatible with 3D printing technology are discussed. Their chemical structures are shown in Figure 1.1.

1.2.1. Natural polymers

Collagen: It is the most abundant protein in mammals, constituting approximately 30% of the total human protein. Notably, type I collagen is the main component of extracellular matrix (ECM) in tissues such as skin, tendon, cartilage, and bone [20]. Structurally, collagen is composed of peptide chains forming a triple helix configuration, which facilitates extensive interactions with cells via integrins. These interactions regulate intracellular signalling pathways, thereby

promoting cell adhesion, proliferation, and differentiation [21]. Moreover, Hung et al. [22] demonstrated that collagen enhances proliferation and osteogenic differentiation of human mesenchymal stem cell (MSC) by activating the ERK and Akt signalling pathways, underscoring its potential for applications in bone tissue engineering. However, pure collagen scaffolds are typically modified through physical and chemical crosslinking or combined with other materials to create composite scaffolds due to the inherently weak mechanical properties. These modifications significantly enhance the mechanical properties, with scaffold moduli ranging from 0.1-89,500 kPa [23].

The hydrolysate of collagen, commonly known as **gelatin**, is a single-chain or multi-chain polypeptide that retains properties similar to collagen. It preserves the abundant arginine-glycine-aspartic acid (RGD) sequence derived from collagen, enabling interactions with integrins and thereby promoting cell adhesion and proliferation [24]. Still, gelatin exhibits poor thermal and mechanical stability due to its gel-sol transition at approximately 37 °C. As a result, gelatin-based scaffolds in tissue engineering are typically produced through physical and chemical crosslinking or combining with other biomaterials [25]. Among them, gelatin-methacrylamide (GelMA) is one of the most widely used modifications, which can be easily crosslinked using ultraviolet (UV) light at room temperature to form hydrogels that are stable at 37 °C. Additionally, its properties are tunable by adjusting the degree of crosslinking, making it highly versatile in tissue engineering [26].

Chitosan: It is derived from marine organisms, such as shrimp and other shellfish, and has a structure similar to glycosaminoglycans (GAGs). Notably, chitosan possesses a positively charged surface, enabling it to aggregate red blood cells and platelets, thereby exerting a hemostatic effect, which is critical for treating injuries to skin, muscle, or nerve tissues [27]. Moreover, Woods et al. [28] demonstrated that chitosan promotes collagen production by fibroblasts and enhances cell support, making it a widely used material for wound healing and skin scaffolds. Similar to collagen, chitosan scaffolds also exhibit poor mechanical

properties and rapid degradation *in vivo*. Consequently, they often require additional physical or chemical crosslinking after printing to enhance their stability and functionality [29].

Alginate: It is a polysaccharide derived from marine algae, known for its advantages of low cost, easy availability, and low toxicity. As an anionic polymer, alginate readily undergoes gelation under mild conditions through crosslinking with calcium ions to form stable hydrogels, making it highly suitable for the encapsulation of cells and bioactive factors for tissue regeneration [30][31]. But alginate scaffolds lack biological binding sites on their surface, resulting in poor cell adhesion, and exhibit fast degradation rates *in vivo* due to their high hydrophilicity [32]. These limitations restrict their standalone application in tissue engineering. To address these challenges, alginate is often combined with other biomaterials. For instance, hybrid scaffolds incorporating chitosan have demonstrated improved mechanical properties and enhanced osteoblasts attachment through ionic bonding [33].

Hyaluronic acid (HyA): It is a linear polysaccharide composed of repeating disaccharide units of D-glucuronic acid and N-acetyl-D-glucosamine. It is a major component of ECM in connective tissues, including skin and cartilage [34]. Due to its abundance of carboxyl and hydroxyl groups, HyA exhibits hygroscopic and water-retaining properties, making it highly promising for applications in skin tissue engineering [35]. Furthermore, Ghatak et al. [36] demonstrated that HyA can bind to proteins, particularly interacting with the major receptor cluster determinant 44 (CD44). This interaction is associated with intracellular signal transduction, which regulates inflammation, promotes cell proliferation, and facilitates cartilage regeneration. However, due to its high-water solubility, HyA undergoes rapid degradation *in vivo*, leading to the loss of mechanical properties and structural stability [37]. Consequently, HyA often requires post-crosslinking or combination with other biomaterials, such as collagen, to improve its performance as a tissue-engineered scaffold.

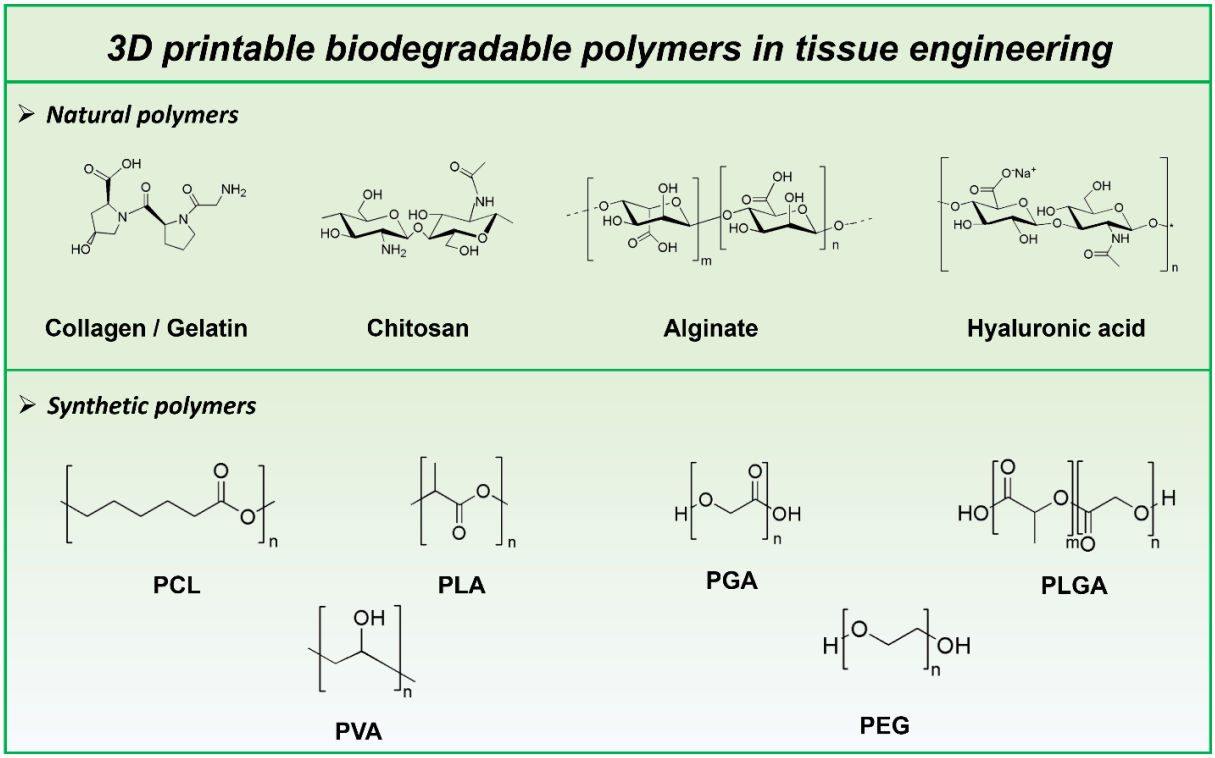

Figure 1.1: Chemical structures of 3D printable biodegradable polymers for tissue engineering.

1.2.2. Synthetic polymers

Poly (caprolactone) (PCL): it is an aliphatic polyester with a low melting point of ~ 60 °C, making it convenient for scaffold processing. Compared with other synthetic polymers, PCL has a slow biodegradation rate (*in vivo* degradation takes approximately 2-3 years) and produces less acidic degradation products, which makes it suitable for tissue engineering applications requiring long regeneration period [38]. Moreover, PCL exhibits modulus of 0.4-0.6 GPa and high flexibility, making it particularly attractive for cartilage, tendon, and bone tissue engineering. Nevertheless, studies have shown that PCL exhibits poor cell adhesion due to its hydrophobic surface [39]. To address these limitations, it is often combined with hydrophilic and bioactive factors to accelerate degradation rates and improve bioactivity. Research has demonstrated that incorporating metallic particles (e.g., ZnO, MgO), ceramics (e.g., hydroxyapatite (HA), beta-tricalcium phosphate (ß-TCP), bioglass), and natural polymers (e.g., collagen, gelatin) effectively improves PCL scaffolds by optimizing degradation rates and bioactivity [40] [41] [42].

Poly (lactic acid) (PLA): it is a bio-based polyester derived from dextrose, capable of degrading into carbon dioxide and water, which can be eliminated through normal metabolic pathways in the body. PLA is also easily processed due to its melting point of 175 °C. Furthermore, PLA scaffolds exhibit modulus of 2-3 GPa, closely resembling that of native bone with 3-20 GPa, thus showing great potential for bone tissue engineering [43]. But its hydrophobicity and high crystallinity lead to a slow degradation rate exceeding 24 months *in vivo*, which does not align with the bone regeneration timeline of 12-18 weeks. Additionally, its acidic degradation products can induce inflammation, negatively impacting the bone healing process [44]. To address these limitations, the incorporation of hydrophilic biomaterials or additives has been extensively explored to enhance its biodegradability and bioactivity. Especially, the addition of hydrophilic HA particles to the PLA scaffold has been proven to effectively accelerate the degradation rate and mitigate the acidic environment via calcium-phosphate precipitation. This modification also improves osteoconductivity and osteoinductivity, making it a widely studied approach in bone tissue engineering [45] [46].

Poly (glycolic acid) (PGA): it is a hydrophilic polymer characterized by its rapid degradation within a few weeks, making it ideal for short-term medical applications such as surgical sutures and vascular implants. Its hydrolysis products are non-toxic and can be eliminated through the tricarboxylic acid cycle or via urine. PGA exhibits a high mechanical strength of 90-110 MPa and an elastic modulus of 6-7 GPa, making it suitable for load-bearing applications such as bone, tendons, and ligaments [47]. Additionally, its highly hydrophilic surface endows it with excellent bioactivity by promoting cell adhesion, cell infiltration, and cell migration, which has been shown to support the growth of multiple cell types on its surface [48]. But its rapid degradation can result in inflammation due to acidic product accumulation and a fast loss of mechanical properties, which limits its applications in tissue engineering [49]. Therefore, recent attention has been paid to the combination of PGA with other materials with slower degradation rates, such as PCL and PLA, to tailor its degradation behavior and extend its utility [50].

Among them, **Poly (lactide-co-glycolide acid) (PLGA)** is synthesized through the copolymerization of PLA and PGA, allowing its degradation rate to be adjustable within the range of 1-6 months *in vitro* and its modulus to be tailored between 1.4-2.8 GPa, depending on the LA:GA ratio [51]. Due to the easy manipulation of mechanical and degradation properties to achieve intermediate characteristics resembling native tissues, PLGA has been extensively applied in several tissue engineering applications, including skin [52], cartilage [53] and bone [54]. However, it is important to note that the accumulation of degradation products can also lead to an acidic environment, causing localized inflammatory responses. Similar to other synthetic materials, PLGA lacks inherent bioactivity, so it is often combined with other biomaterials or bioactive factors, particularly anti-inflammatory agents such as magnesium hydroxide ($Mg(OH)_2$) [55].

Poly (vinyl alcohol) (PVA): It is a water-soluble polymer with a tensile strength in the range of 1-17 MPa in hydrogel form, closely resembling the mechanical properties of native articular cartilage. Due to the abundance of hydroxyl groups in the structure, PVA hydrogels exhibit excellent water adsorption and retention capabilities, making it highly attractive for skin and cartilage tissue engineering [56]. Notably, in an indirect way, Wolff et al. [36] utilized 3D-printed PVA scaffolds as sacrificial templates to fabricate perfused scaffolds with dense vascular channels of organ size [57]. However, PVA lacks bioactive components, limiting its protein adsorption and cell adhesion capabilities. Thus, it is often combined with natural materials, such as chitosan, which have been demonstrated to effectively improve mechanical stability and cell-matrix interactions through the formation of abundant intermolecular and intramolecular hydrogen bonds between the hydroxyl groups of PVA and chitosan [58].

Poly (ethylene glycol) (PEG): This is another widely used polymer in biomedical applications, which can be metabolized and excreted by the body. The blocked dihydroxy groups in PEG can be easily modified or reacted to create scaffolds with tunable properties and functions [59]. Like PVA, PEG is water-soluble and can be readily converted into hydrogels. A commonly used derivative

is photo-crosslinkable polyethylene glycol diacrylate (PEGDA), which exhibits improved mechanical stability and is frequently employed in tissue engineering [60]. Moreover, the low glass transition of ~ 40 °C and melting temperature of ~ 70 °C make it an ideal candidate for blending or copolymerization with other biodegradable polymers such as PCL and PLA to enhance their processability [61]. However, due to its low protein adhesion properties, PEG exhibits limited bioactivity. To address this, PEG is often combined with other biomaterials or bioactive factors. For instance, incorporating PEG with GelMA has been shown to significantly increase stiffness and enhance the proliferation of human MSCs compared to PEG scaffold alone [62].

1.3. 3D printing of biodegradable polymer scaffolds

3D printing is an additive manufacturing technique that uses computer-aided design (CAD) models to create three-dimensional (3D) objects layer by layer. This process eliminates the need for traditional tools, fixtures, or multiple processing steps, enabling the efficient and accurate fabrication of complex geometries in a single operation [63]. In tissue engineering and regenerative medicine, 3D printing has attracted widespread attention due to its ability to produce customized structures with precise specifications. Its rapid prototyping capabilities meet the medical demand for small-batch and individualized solutions. Biodegradable polymers are particularly well-suited for biofabrication due to their low-cost, ease of processing, and adaptability to various forms such as filaments, resins, powders, or bio-inks [64]. The main 3D printing techniques applicable to biodegradable polymers include extrusion, vat photopolymerization, binder jetting, selective laser sintering, and bioprinting, as illustrated in Figure 1.2.

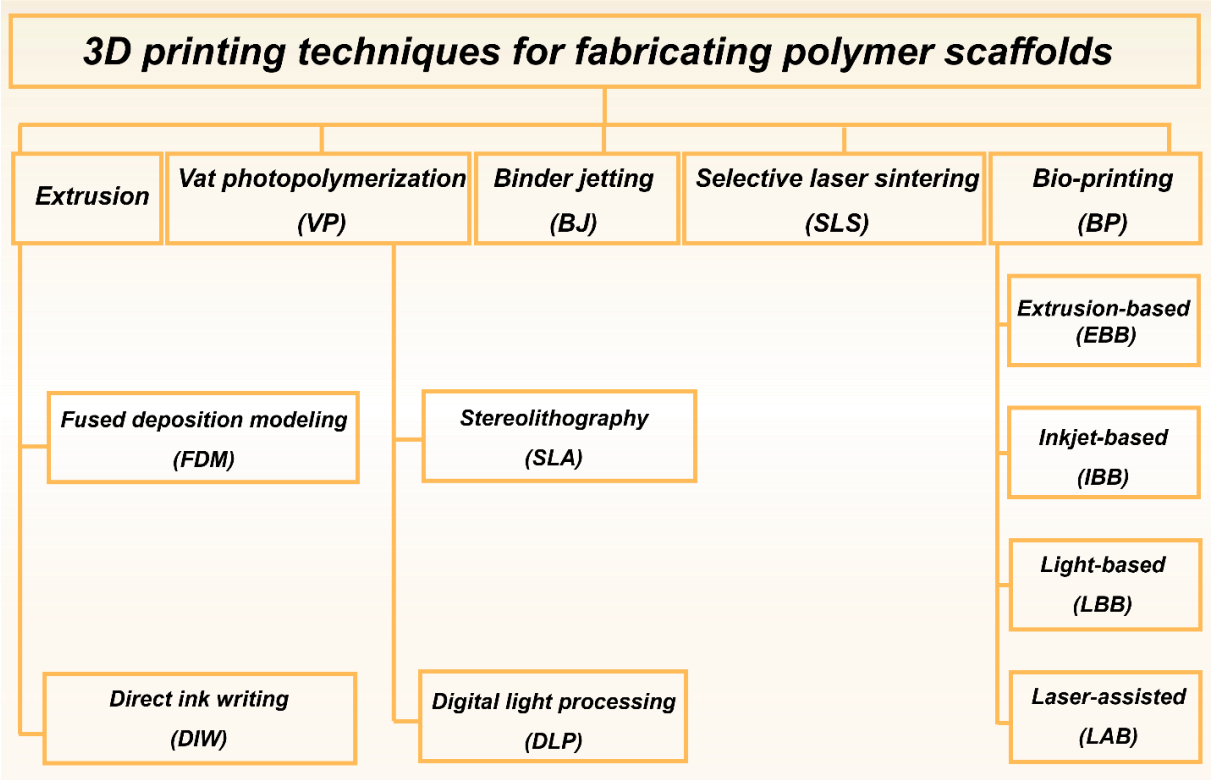

Figure 1.2: 3D printing techniques for fabricating biodegradable polymer scaffolds in tissue engineering.

1.3.1. Extrusion

Fused deposition modelling (FDM) is the most widely used 3D printing technique in tissue engineering due to its simplicity, cost-effectiveness, accuracy, and repeatability. In FDM, material filaments are melted and extruded through a nozzle at the operating temperature and then solidified after deposition to form desired architectures [65]. Biodegradable thermoplastic polymers such as PCL, PLA, PLGA, and PVA, and their composites are frequently used in FDM, resulting in scaffolds with high mechanical properties [66][67][68]. However, the high operating temperature of FDM makes it incompatible with natural polymers and bioactive factors sensitive to heat, such as proteins, which significantly limits their applications in tissue engineering.

Direct ink writing (DIW) is another type of extrusion-based technique that typically operates at room or physiological temperature, where liquid or hydrogel inks are deposited under pressure. This technique is highly dependent on the

rheological behavior of the printing inks, making it well-suited for various types of material [69]. Inks used in DIW should exhibit shear-thinning behavior with a critical viscosity ranging from 10^2 to 10^6 mPa·s at a shear rate of approximately 0.1 s^{-1}, to ensure printability. After deposition, post-curing under specific conditions, such as solvent evaporation, photocuring, or heat treatment, is required to achieve structural stability [70]. DIW inks used in tissue engineering are polymer hydrogels or viscous polymer solutions (e.g. PCL, PLA in chloroform) with high particle content, which solves the problem that polymers with high particle content cannot be processed into filaments required for FDM [71][72]. However, due to the critical viscosity of inks, scaffolds structures are prone to sagging or collapsing after deposition, leading to low resolution.

1.3.2. Vat photopolymerization (VP)

Vat photopolymerization (VP) is an effective 3D printing method for fabricating polymer scaffolds under physiological conditions. This technique relies on light-activated polymerization using UV, visible, or near-Infrared (NIR) light to solidify structures layer by layer. VP is mainly divided into two types, stereolithography (SLA), which uses a top-down configuration, and digital light processing (DLP), which employs a bottom-up configuration [73]. The ink used in SLA and DLP should be liquid with a viscosity of less than 10 Pa·s to ensure proper fluidity and continuity of the reaction. Compared with other 3D printing techniques, SLA and DLP provide higher accuracy and resolution, reaching up to 100 nm. However, additional post-processing, such as heat treatment or photocuring, is often required to enhance mechanical properties of fabricated scaffolds [74]. The selection of biodegradable polymers suitable for SLA and DLP is limited because most are not inherently photoactive. Some biodegradable polymers can be modified with acrylate or methacrylate groups to enable photopolymerization. Some examples include collagen, gelatin, chitosan, alginate, HyA, PEG. Among these, GelMA [75] and PEGDA [76] are two widely used modified polymers for scaffold fabrication in tissue engineering.

1.3.3. Binder jetting (BJ)

Binder jetting (BJ) is a special 3D printing process where a liquid binder is sprayed through a nozzle onto a solid powder bed along a designed path, bonding the powder layer by layer to create 3D scaffolds. This method offers several advantages, including low cost, high fabrication speed of 200 cm^3/min, the ability to produce complex structures without the need for support, and the reuse of unbound powder [77]. However, BJ has limitations such as a low resolution (< 200 μm) and poor layer adhesion, requiring post-curing process to improve the scaffold performance. Moreover, the limited selection of binder and powder (in terms of size and flow properties) directly impacts the quality of scaffold and overall printing performance [78]. Scaffolds produced via BJ for tissue engineering are primarily made from metals or ceramics. A smaller proportion of scaffolds are fabricated from polymers such as PCL, PLA, PVA and their composites, which are mainly used for drug delivery implants and load-bearing bone scaffolds [79][80].

1.3.4. Selective laser sintering (SLS)

Selective laser sintering (SLS), a type of powder bed fusion (PBF), binds material powders layer by layer to form scaffolds using laser power. SLS shares similar advantages with BJ, such as high fabrication speed, the ability to create complex structure without the need for support, and reusable powder [81]. It also offers high accuracy and resolution, which depends on precise conditions of the powder (size, shape and flow properties) and laser settings (power, energy density, and speed) [82]. However, the high cost associated with lasers is a significant drawback. Additionally, the high temperature generated by lasers limits the selection of materials suitable for tissue engineering, and rapid cooling can easily cause scaffold deformation and shrinkage [83]. Despite these challenges, polymers such as PCL, PLA, PVA, PLGA and their composites are commonly processed by SLS to fabricate scaffolds with high mechanical properties [86,87].

1.3.5. Bio-printing (BP)

Bio-printing is a technique based on the aforementioned 3D printing techniques, to manufacture scaffolds including living cells, tissues, and growth factors in a mild environment. This strategy has enormous potential for cell-loaded applications in tissue engineering. Bio-printing mainly includes the following techniques: extrusion-based bioprinting (EBB), inkjet-based bioprinting (IBB), light-based bioprinting (LBB) and laser-assisted bioprinting (LAB). The bioinks used are mainly hydrogels made from collagen, gelatin, alginate, chitosan, HyA, PEG or PVA, which can encapsulate cells for proliferation and differentiation.

EBB is the most widely used and efficient bio-printing technique. It mainly relies on pneumatic, piston or screw-based pressure to extrude bio-ink at room or physiological temperatures [84]. Bioinks used in EBB have a wide viscosity range, from 30 to over 6×10^7 mPa·s, making it compatible with high-viscosity inks and high cell loading (10^8 -10^9 cells/mL), which is suitable for large cell-loaded scaffolds fabrication [85]. EBB is compatible with various biodegradable hydrogels, such as collagen [86] and gelatin [87]. A major issue is the printing pressure and shear forces from the nozzle during printing, which results in relatively low cell viability (40% - 86%) compared to other bioprinting methods [85].

The second technique is IBB, a material jetting (MJ) method that jets bio-inks through a nozzle onto the printing platform layer by layer under the influence of thermal, piezoelectric, or electromagnetic forces. IBB offers advantages such as low cost, high fabrication speed (0.1-1 m/s), high resolution (<30 μm), and high cell viability (>90%), making it promising to create scaffolds with complex microstructures [87]. But the cell loading in the bioink is limited to 10^6 -10^7 cells/mL, while exceeding this range increases viscosity (3.5-12 mPa·s), which can cause several issues such as uneven droplets, cell aggregation, and nozzle clogging [88]. Additionally, due to the limited viscosity, a post-crosslinking process is required after deposition to maintain structural integrity.

To address these issues, nozzle-free methods have been developed, which avoid the shear force caused by printing nozzles. One such method is light-based bioprinting (LBB), which includes SLA and DLP. LBB works by selectively cross-

linking bio-inks with UV or visible light [89]. Due to the absence of nozzle, LBB offers high printing resolution (50 μm) and high cell viability (90%), enabling the fabrication of cell-loaded scaffolds with precise architectures [90]. However, the limited availability of photoactive materials and the potential damage from accumulated UV irradiation restrict its application.

The final method is LAB, which uses a laser to project energy onto the printing platform containing a top laser-absorbing substrate layer and a bottom bio-ink layer. The top layer absorbs laser energy, causing a phase change that ejects the bio-ink onto the platform [91]. For LAB, the viscosity of the bio-ink ranges from 1 to 300 mPa·s, allowing for a high cell loading density (>10^8 cells / mL) and high cell viability (> 90%). Additionally, LAB achieves a high resolution (10-50 μm) due to the micro-scale control of droplets by the laser [90]. Nevertheless, LAB is expensive, and the potential laser damage to cells both limit its application in tissue engineering.

1.4. Osteochondral tissue engineering application

The current applications of 3D-printed biodegradable polymers scaffolds in tissue engineering are both diverse and promising. In principle, the mechanical properties of the scaffold must match those of native tissues, depending on the application requirements of the target tissue. At the same time, the scaffold should gradually degrade during the growth of new tissues, ultimately leaving no residue in the body. Osteochondral tissue is a complex structure composed of cartilage and subchondral bone, playing a crucial role in load-bearing and joint function. The cartilage layer provides a smooth, low-friction surface for articulation, while the underlying bone layer ensures mechanical support and nutrient exchange. Due to its limited self-healing capacity, repairing osteochondral defects requires biomimetic scaffolds that can support tissue regeneration. An ideal scaffold should possess a hierarchical structure that mimics the native osteochondral interface, with a gradient in composition and mechanical properties to accommodate the distinct characteristics of cartilage and bone. Due to the distinct structure and properties, cartilage layer and bone layer are discussed separately as follows.

1.4.1. Cartilage layer

Cartilage tissue is a flexible connective tissue that bears loads, lubricates joints, and protects bones from mechanical damage. It is composed of water, cartilage cells (primarily chondrocytes) and ECM consisting of GAGs, proteoglycans, and collagen fibers. Due to the lack of nerves and blood vessels, cartilage is unable to self-repair following trauma or disease, resulting in the loss of mobility [92]. Thus, the objective of cartilage tissue engineering is to design scaffolds that provide adequate mechanical strength, flexibility, and support for the regeneration of cartilage tissue, while promoting cell proliferation and ECM deposition. Hydrogels made of collagen, gelatin, HA, and PEG are highly attractive in cartilage tissue engineering due to their flexibility, water retention, and ability to support chondrocyte activity [93]. Meanwhile, synthetic polymers such as PCL, PGA, PVA, and PLGA have also been widely used as frameworks to provide sufficient mechanical strength and flexibility to support tissue growth [56,94]. Additionally, depending on the application, SLA/DLP and EBB are suitable for fabricating customized or cell-laden scaffolds for articular cartilage regeneration and small cartilage defect repair, while FDM and SLS are more optimal for creating strong, mechanically stable scaffolds used in load-bearing cartilage regeneration [95–97].

Jiang et al. [98] used EBB to fabricate a 3D-printed hydrogel scaffold featuring an interpenetrating double network structure made from gelatin derived from cold-water fish skin and alginate. By fine-tuning the ratio of these materials, the scaffolds achieved compression modulus up to 20 MPa, making them suitable for load-bearing tissues such as knee joints. Notably, these scaffolds showed non-immunogenicity, non-toxicity, and biodegradability, enabling substantial cartilage defect repair and regeneration in a rat model, while gradually degraded within 12 weeks. To replicate the gradient structure of native cartilage, Li et al. [97] developed a biphasic scaffold combining PCL and GelMA. The top layer consisted of GelMA hydrogel embedded with rat-derived MSCs and chondrocytes, while the bottom layer featured an FDM-printed PCL scaffold impregnated with the same cell-loaded GelMA hydrogel. Their results showed that the co-culture of these cell

types effectively induced synergistic chondrogenesis and cartilage regeneration both *in vitro* and *in vivo*. Moreover, the biphasic scaffolds had a modulus of 228.9 kPa closely resembling that of native cartilage, and less mechanical pain than cartilage defects observed by gait analysis after implantation in rats, highlighting the potential for cartilage regeneration.

1.4.2. Subchondral bone layer

Subchondral bone supports the overlying articular cartilage and distributes mechanical loads across the joint surface by gradually changing stresses and strains. It is a hard connective tissue primarily composed of collagen type I and minerals, including both subchondral cortical plate and subchondral trabecular bone. Effective subchondral bone scaffolds should possess mechanical properties compatible with those of native tissue, which has an elastic modulus in the range 297-475 MPa [99]. Additionally, subchondral trabecular bone are porous structures with abundant vessels and nerves that play an important role in load absorption and structural support as well as nutritional supply to cartilage. Thus, porosity plays a critical role in subchondral bone. An optimal pore size of 200 to 500 μm is considered ideal for bone regeneration and vascularization [100,101]. Natural polymers, such as collagen and chitosan, are attractive for bone tissue engineering due to their biocompatibility but are limited by weak mechanical properties. On the other hand, synthetic polymers such as PCL, PLA, and PLGA offer high stiffness but lack osteoconductive and osteoinductive properties, resulting in low bone regeneration efficiency [102]. Therefore, there has been growing interest in incorporating bone-promoting additives into 3D-printed scaffolds, such as calcium phosphate-based materials (e.g., HA and ß-TCP), metallic particles like ZnO and MgO, and growth factors like bone morphogenetic protein-2 (BMP-2) [103,104].

Zhang et al. [45] developed 3D-printed PLLA/nHA scaffolds with a high nHA content of up to 50% through FDM. This scaffold achieved a high compressive strength of 14.2 MPa, comparable to that of human cancellous bone (2-12 MPa). The addition of hydrophilic nHA improved the degradation rate and mitigated the acidic degradation environment by the formation of Ca-P whiskers. *In vivo* studies

revealed that, after 4 weeks of implantation in the rabbit femur, the scaffold with 50% nHA were filled with newly formed bone tissue, which was tightly integrated with the scaffold surface, demonstrating robust osteo-regeneration capability. Except for the addition, the microenvironment induced by scaffolds also plays a crucial role in bone regeneration by regulating cell-to-cell interaction. Yeung et al. [105] fabricated 3D-printed PCL-PEG-PCL scaffolds enhanced with silane-coated MgO nanoparticles. The gradual release of Mg ions through scaffold degradation promoted the proliferation and differentiation of mouse pre-osteoblasts (MC3T3-E1) by stimulating DNA and protein synthesis. Implantation in a lateral epicondyle defect model further demonstrated the ability to induce in-situ bone regeneration, evidenced by increased mineral deposition and new bone formation over time. Growth factors, particularly BMP-2, have been shown to directly and effectively promote bone regeneration. Lee et al. [106] designed a composite scaffold using a 3D-printed PLA scaffold as mechanical support combined with BMP-2 loaded gelation/alginate gel as the biological cue. The released BMP-2 retained comparable osteoinductive activity to fresh BMP-2, promoting better new bone formation than scaffold without BMP-2 in a rat calvaria defect model. Moreover, in an ectopic ossification model, regular-shaped bone was observed to form around the scaffold at the defect site, demonstrating its ability to control the shape of bone regeneration and avoid unwanted osteogenesis outside the scaffold.

1.4.3. Challenges of scaffolds in osteochondral tissue engineering

Considering the distinct integrated properties of cartilage and subchondral bone, the ideal scaffold for osteochondral tissue engineering should exhibit different compositions, mechanical properties, and biological environments. However, achieving a seamless gradient between layers remains a difficult problem in engineering. Additionally, scaffolds must provide sufficient mechanical strength while maintaining porosity to facilitate cell infiltration and nutrient diffusion. Biodegradation rates must also be carefully controlled to match tissue regeneration, because premature degradation can lead to structural failure, while slow degradation may hinder new tissue formation. Another challenge is ensuring proper vascularization in the bone region while maintaining a low-vascular

environment in the cartilage layer, as an imbalance can impair regeneration. Furthermore, stimulating both chondrogenesis and osteogenesis within a single scaffold requires carefully tuned biomaterials, bioactive factors, and cellular interactions. Overcoming these challenges is crucial for developing functional osteochondral grafts that integrate successfully with native tissue and restore joint function.

1.5. Motivation and objectives

Tissue engineering and regenerative medicine offer promising solutions for rehabilitating or replacing damaged osteochondral tissues through scaffold fabrication. Osteochondral tissue consists of two distinct yet integrated layers: cartilage, which is avascular and provides a smooth, load-bearing surface, and subchondral bone, which offers mechanical support and nutrient supply. The complex mechanical and biological gradients between these layers present a significant challenge for scaffold design. Selecting suitable materials and manufacturing methods is crucial for developing tissue-adapted and customizable scaffolds that effectively mimic these gradients.

Biodegradable polymers with excellent biocompatibility, controlled degradation, and appropriate mechanical properties have gained significant attention, particularly in 3D-printed scaffolds. Recent advancements have focused on multilayered and gradient scaffold designs that replicate the structural and mechanical transitions of native osteochondral tissue. Especially, multi-material approaches allow the integration of polymers with different stiffness and elasticity, leading to functionally graded scaffolds that enhance cell adhesion, differentiation, and the overall regenerative potential. However, despite some progress, it remains a huge challenge that how to select and design scaffolds that not only replicate the distinct mechanical properties of the cartilage and subchondral bone layers, but that also simultaneously promote both chondrogenesis and osteogenesis for effective tissue regeneration, while keep long-term integration and stability during the tissue regeneration period.

The overall aim of the thesis is to develop a biomimetic scaffold with gradient mechanical properties, matched degradation and regenerative capability suitable for osteochondral tissue engineering. Specifically, the first goal of this thesis is to develop 3D-printed biodegradable polymer scaffolds, with biomimetic structure, tailored mechanical properties and degradation rates in physiological conditions with respect to cartilage layer and bone layer in osteochondral tissue, respectively, while supporting cell adhesion and growth. The second goal is to conduct advanced assays to evaluate the chondrogenic and osteogenic capabilities of these scaffolds, in terms of cell proliferation, genes expression, specific factors release and matrix deposition, ultimately determining the potential of the combined scaffold for application in osteochondral tissue engineering.

Following these goals, the thesis is structured as follows:

Chapter 1 briefly summarized the current state of scaffolds in tissue engineering, including the introduction of 3D printable biodegradable polymers and 3D printing techniques for polymer scaffolds. Moreover, the application of 3D-printed biodegradable polymer scaffolds in osteochondral tissue engineering was explored in terms of cartilage layer and bone layer, while the challenges of scaffolds for osteochondral tissue were also listed.

Chapter 2 introduced the fabrication process of 3D-printed scaffolds, biomimetic composite scaffolds, and bilayer scaffolds. The structural, thermal, crystallized, and rheological properties were characterized. Then, the mechanical properties were investigated in tension and compression mode, and degradation tests were conducted in accelerated and physiological conditions. Finally, biological performance was studied through a biocompatibility test, advanced chondrogenic assay, and advanced osteogenic assay.

Chapter 3 explored the processing, composition, mechanical properties, and accelerated degradation behaviour of PCEC copolymers. Three different crystallization regimes were revealed depending on the PCL/PEG block ratio, significantly affecting the properties. The biocompatibility of PCEC copolymers, as well as the ability to be manufactured into 3D-printed scaffolds, were also evaluated to confirm the capability in tissue engineering.

Chapter 4 studied the processing, mechanical properties, degradation behaviour of CI/II-HyA@PGS composite scaffold. Moreover, the biocompatibility and chondrogenic capacity were evaluated by culturing with rat-derived mesenchymal stem cell (MSC) for 28 days, including the exploration of metabolic activity, cell viability, sulfated glycosaminoglycans (sGAG) production, gene expression and *de-novo* cartilage-like matrix deposition.

Chapter 5 examined the processing, mechanical properties, degradation behaviour of CI-nHA@PCEC composite scaffold. Moreover, the biocompatibility and the osteogenic potential were checked by culturing with pre-osteoblast MC3T3 cells for 28 days through analysis of alkaline phosphatase (ALP) release, calcium deposition, gene expression. Additionally, the angiogenic potential was assessed by evaluating tube formation and gene expression in human endothelial EA.hy 926 cells after 5 days of culture.

Chapter 6 investigated the processing, mechanical properties, degradation behaviour of bilayer composite scaffold, revealing its unique composition, morphology and mechanical properties, as well as its matched degradation rate and mild degradation environment in physiological conditions.

Finally, Chapter 7 discusses the application potential of the biomimetic bilayer composite scaffold for osteochondral tissue engineering based on the results in the previous chapters, including the main conclusions of the thesis and future directions of the work.

2. Materials and experimental techniques

2.1. Scaffolds manufacturing

2.1.1. Printing inks

2.1.1.1. PGS ink

The PGS ink was prepared by mixing PGS prepolymer and sodium chloride particles. PGS prepolymer was synthesized through the polycondensation of glycerol and sebacic acid, as previously described [107,108]. Briefly, glycerol (anhydrous, >99.5%, Sigma-Aldrich, Germany) and sebacic acid (analytical grade, 99%, Sigma-Aldrich, Germany) at a molar ratio of 1:1 were mixed and heated to 120 °C under agitation in a nitrogen atmosphere for 24 h. Then, the pressure was reduced to 2 mbar, and a continuous stirring was conducted at 120 °C for another 24 h to obtain the PGS prepolymer. Afterwards, the PGS prepolymer was dissolved in tetrahydrofuran (THF, anhydrous, 99 %, Sigma-Aldrich, Germany) at a mass/volume ratio of 1:5. Next, grided sodium chloride particles (NaCl, 99 %, Sigma-Aldrich, Germany, diameter of 1-75 μm) with a double weight of PGS prepolymer were added to the solution and stirred for 24 h. Finally, the mixture was transferred to a vacuum oven and dried at 50 °C overnight to remove the solvent. The resulting mixture was used as the ink for 3D printing.

2.1.1.2. PCEC ink

PCEC copolymers were synthesized by ring-opening polymerization (ROP) of ε-CL and PEG as previously described [109]. Typically, 0.2 mmol polyethylene glycol (PEG, Sigma-Aldrich, M_n= 0.6k, 2k, 6k, 20k and 35k g/mol, dried before use) and 0.175 mol ε-caprolactone (ε-CL, Sigma-Aldrich, 97%, distilled) were weighed into a Schlenk flask, and the catalyst of tin (II) 2-ethylhexanoate ($Sn(Oct)_2$, Sigma-Aldrich, 92.5-100.0%) with a 0.5 wt% ratio was dropped into the mixture. Then, the branch pipe on the flask was connected to a vacuum pump for 10 min to remove the residual moisture and oxygen in the flask. Afterwards, the flask was immersed

in an oil bath at 110 °C under stirring for 24 h. Then, the product was dissolved in dichloromethane (CH_2Cl_2, TCI EUROPA N.V. Belgium, 99.0%, anhydrous) and precipitated into petroleum ether (Sigma-Aldrich, boiling point ≥ 90% 40-60 °C) three times to purify the product. After filtration and drying in a vacuum oven at 40 °C for 24 h, white block products were obtained (yield: > 95%). According to the molecular weight of initiators, the obtained samples were named by $PCE_{0.6k}C$, $PCE_{2k}C$, $PCE_{6k}C$, $PCE_{20k}C$ and $PCE_{35k}C$, respectively. PCL was synthesized as above from ethylene glycol (EG, Sigma-Aldrich, 99.8%, anhydrous) and ε-CL at the same ratio. PCL and PCEC copolymer samples (~ 7 g) were transferred to a mold (100 × 100 × 0.5 mm^3) and processed by hot-pressing at 120 °C for 10 min under a pressure of 20 MPa to obtain regular polymer films for characterization. Among them, $PCE_{20k}C$ was dissolved again in CH_2Cl_2 and poured into flat plates to obtain thin films. After drying overnight in hood, $PCE_{20k}C$ thin films were cut into small pieces to be used as pellet inks for 3D printing.

2.1.2. Scaffolds fabrication

2.1.2.1. PGS scaffolds

A 3D printing system (F40, Direct 3D, Italy) with a screw-assistant extrusion driving was used to manufacture the PGS scaffold. The ink was placed in the printing system installed with a 500 μm nozzle and printed at 50 °C with a moving speed of 10 mm/s and a screw flow percentage of 600 %. Once the printing head was filled up with the ink, cubic shape samples with a design of a layer thickness of 500 μm, a pore diameter of 1000×1000 μm, and a 0°/90° laying pattern were printed. Then, the samples were placed in a vacuum oven at 100 °C, 0.5 bar for 15 h, and then at 150 °C, 1 bar for 24 h to complete the curing process. The cured scaffolds were soaked in distilled water for 24 h (water was changed 4-6 times) to remove the NaCl particles and then freeze-dried (FreeZone 4.5 Liter -50C Benchtop, Labconco, the United States) at -50 °C under a pressure of 0.2 mbar to get the final PGS scaffolds with high porosity. Finally, scaffolds were cut by a biopsy puncher (Kai Medical, Japan) with a 6 mm diameter to obtain the desired cylindrical structure.

2.1.2.2. PCEC scaffolds

$PCE_{20k}C$ pellets were pour into the same 3D printing system with a nozzle of 500 μm to manufacture porous scaffolds. The extruder of the printer was set with a printing temperature of 90 °C, a moving speed of 10 mm/s and a flow percentage of 2000%. After pre-heating for 30 min, the melted materials were deposited layer by layer in a 0°/90° laying pattern to fabricate scaffolds with a filament diameter of 500 μm, a distance between filaments of 1000 μm and a final height of 3 mm. Finally, $PCE_{20k}C$ scaffolds were cut by a biopsy puncher with a 6 mm diameter to obtain the cylindrical structure.

2.1.3. Biomimetic composite scaffolds

2.1.3.1. CI/II-HyA@PGS composite scaffold

To fabricate the biomimetic composite scaffold, the 3D-printed PGS scaffold was combined with a pro-chondrogenic collagen-based matrix slurry consisting of collagen type I/II and hyaluronic acid (CI/II-HyA) designed in previous study [110]. Briefly, the CI/II-HyA slurry was prepared with a total collagen concentration of 0.5% w/v (collagen I and collagen II at ratio 1:1) and a hyaluronic acid concentration of 0.05% w/v.

The PGS scaffold was loaded with 0.3 mL of the previously prepared CI/II-HyA slurry into a stainless-steel tray (dimensions: 9.5 mm diameter and 4 mm height) prior being freeze-dried (Virtis Genesis 25EL, Biopharma, UK) at a constant cooling rate of 1 °C/min to a final temperature of -20 °C and drying at a pressure of 200 mTorr [111]. Then, the scaffold was punched to get a final dimension of 6 mm in diameter and 3 mm in height using a biopsy puncher. CI/II-HyA scaffold without the 3D-printed PGS framework was also fabricated and crosslinked using a dehydrothermally (DHT) crosslinking procedure in a vacuum oven (VacuCell, MMM, Germany) at 105 °C for 24 h under a pressure of 0.05 bar.

2.1.3.2. CI-nHA@PCEC composite scaffold

Collagen based slurry including of collagen type I and nano-hydroxyapatite (CI-nHA) was prepared according to previous established methods [112]. Briefly,

calcium chloride ($CaCl_2$, 0.13M, Fisher Chemical, Ireland) solution was added to trisodium phosphate solution (Na_3PO_4, 0.42M, Sigma-Aldrich, Ireland) with sodium hydroxide (NaOH, Fisher Chemical, Ireland) and DARVAN® 821-A (R.T. Vanderbilt Holding Company, Inc, USA), followed by stirring overnight. The mixture was centrifuged to remove the supernatant and resuspend in water 3 times. Then the n-HA suspension was obtained by resuspending the precipitation product into acetic acid (0.5M, Sigma-Aldrich, Ireland) and then sonicated for 2-3 minutes. Finally, n-HA suspension was dropped to 300 mL collagen type I (lyophilized polymeric collagen, Sigma-Aldrich, Ireland) in acetic acid slurry through blending for 2 h to get the homogenous CI-nHA slurry.

The 3D-printed $PCE_{20k}C$ scaffold was then placed in a stainless-steel plate, and 0.3 mL of prepared CI-nHA slurry was poured to cover the scaffold. Then, the plate was placed in the freeze-drier with a processed procedure of a constant cooling rate of 1 °C/min, a final temperature of -40 °C and a pressure of 200 mTorr for 40 h. The final composite scaffold of 6 mm in diameter and 3 mm in height was obtained by using a biopsy puncher. For comparation, CI-nHA scaffold without the 3D-printed PCEC framework was also fabricated through the same methods and subjected to an additional treatment of a dehydrothermal (DHT) cross-linking procedure in a vacuum oven under 0.05 bar pressure at 105 °C for 24 h.

2.1.3.3. Bilayer composites scaffold

The bilayer composite scaffold was assembled by in-situ bonding of CI/II-HyA@PGS and CI-nHA@PCEC composite scaffolds. Briefly, a small amount of CH_2Cl_2 was applied to the bottom surface of CI-nHA@PCEC scaffold using a scalpel (Sigma-Aldrich). As the superficial PCEC filaments were dissolved to get a tacky surface, the CI/II-HyA@PGS scaffold was carefully placed on the surface and pressed to ensure a firm bonding. Finally, the combined bilayer scaffold was left in a fume hood overnight to allow complete evaporation of residual CH_2Cl_2.

2.2. Composition and structural characterization

2.2.1. Nuclear magnetic resonance spectroscopy (NMR)

NMR spectroscopy is a technique for determining the structure of organic compounds, which identifies the positions of atoms in molecules. In this thesis, the composition and structure of PCL and PCEC copolymers was analysed by ^{1}H-NMR and ^{13}C-NMR spectra measured in an NMR instrument (AVANCE III 400, Bruker, USA) at 400 MHz using deuterated chloroform as the solvent.

2.2.2. Fourier transform infrared spectroscopy (FT-IR)

FT-IR spectroscopy is a technique to define the presence and absence of functional groups, which can provide complementary chemical information with NMR spectroscopy. In this thesis, a FTIR spectrometer (Nicolet iS50, ThermoFisher) under an ATR mode was used to study the chemical structure of PCL, PCEC copolymers, glycerol, sebacic acid, PGS prepolymer, CI/II-HyA matrix, PGS framework and CI/II-HyA@PGS composite scaffold.

2.2.3. Gel permeation chromatography (GPC)

GPC is a technique to determine the molecular weight averages and complete molecular weight distribution by separating polymers and organic molecules based on their size. In this thesis, the molecular weight and the dispersity of PCL and PCEC copolymers were obtained from a gel permeation chromatographer (Waters1525, Spain) that equipped with a Waters 2424 refractive index detector and a Waters 2489 UV detector. GPC process was carried out at 25 °C using monodisperse polystyrene (Sigma-Aldrich, Germany) as the standard sample, and THF as the solvent.

2.2.4. Atomic force microscopy (AFM)

AFM is a high-resolution form of scanning probe microscopy that employs a sharp tip in a raster motion to measure and visualize materials at the atomic and nano scales. In this thesis, the surface morphology of PCL and PCEC copolymer

films was assessed by using an AFM (XE-150, Park Systems). Areas of 20×20 μm were scanned in contact mode at a rate of 0.3Hz. Average roughness (Ra) was measured and recorded from the surface.

2.2.5. Scanning electron microscopy (SEM)

SEM is a technique that produces images of a sample by scanning it with a focused beam of electrons. In this thesis, the morphology of CI/II-HyA, PGS, CI/II-HyA@PGS, CI-nHA, PCEC and CI-nHA@PCEC scaffolds in top and cross-section view were observed in field-emission scanning electron microscope (FESEM, JSM-7800 F, ThermoFisher) at an accelerating voltage of 5.0 kV.

2.3. Thermal properties and crystallization behaviour

2.3.1. Dynamic mechanical analysis (DMA)

DMA is a technique used to characterize the thermal properties of a material by recording the deformation as a function of frequency, temperature or time. In this thesis, the thermal properties of PCL and PCEC copolymers were studied by using a DMA machine (TA-Q800) over a temperature range of -110°C to 40°C, a heating rate of 3 °C/min, and a frequency of 1 Hz.

2.3.2. Differential scanning calorimetry (DSC)

DSC is a technique to determine physical or chemical changes in the material as a function of temperature. In this thesis, DSC was performed in PCL and PCEC copolymers films (5-10 mg) by using a TA-Q200 machine in an N_2 atmosphere (50 mL/min). Samples were tested from -40 °C to 100 °C and kept for 1 min to remove the thermal history, then quenched to -40 °C at a cooling rate of 10 °C/min, and after isothermal equilibrium for 1 min, heated to 100 °C at a rate of 10 °C/min.

2.3.3. X-Ray diffraction analysis (XRD)

XRD is a rapid analytical technique primarily used for phase identification of crystalline materials. In this thesis, XRD was conducted on an X-ray diffractometer (PANalytical B.V., Netherlands) with Ni-filtered Cu Kα radiation from 10° to 40° to study the crystallization behaviour of PCL and PCEC copolymers.

2.3.4. Rheological properties

Rheology is the science of flow that describes the interrelation between force, deformation and time. In this thesis, the rheological properties of PCL and PCEC copolymers were explored on a rheometer (Anton Paar MCR 702e, Austria) by using disk samples with a diameter of 25 mm and a thickness of 1 mm at 110 °C under a shear stain of 3% in a frequency range of 0.1-50 rad/s. The storage modulus (G'), loss modulus (G") and complex viscosity (η*) were recorded during the experiment.

2.4. Mechanical characterization

2.4.1. Tensile tests

PCL and PCEC copolymer films were cut into dog-bone shape with dimensions of 75 mm × 4 mm × 0.5 mm, following ISO 527/2 5A (1996) standard. A universal tensile testing machine (Instron 5966, USA) was utilized to carry out the tensile tests with a 500 N load cell and an initial length of 40 mm at a speed of 10 mm/min. A minimum of 6 specimens were tested for each sample.

2.4.2. Compression tests

The mechanical properties of original and degraded CI/II-HyA, PGS, and CI/II-HyA@PGS scaffolds were evaluated at room temperature in a bioreactor (TC-3F, Ebers, Spain) with a 50 N load cell and compressive grips in dry condition (air) and wet condition (PBS solution). Scaffolds with cylindrical shapes of a diameter of 6 mm and a thickness of 3 mm were used in the tests. The scaffolds for the wet

tests were immersed in 0.1M phosphate-buffered saline (PBS, Gibco, UK) overnight before compression. Scaffolds were compressed to a strain of 50% at a speed of 0.1 mm/s, and stress-strain curves were recorded. Cyclic compressions in dry and wet conditions were carried out by compressing scaffolds up to a maximum strain of 10%, 20%, and 40%, for 10 cycles at the speed of 0.1 mm/s. A minimum of 6 scaffolds were tested for each sample.

CI-nHA, PCEC, and CI-nHA@PCEC scaffolds with cylindrical shapes of a diameter in 6 mm and a thickness in 3 mm were also tested under dry and wet conditions. The mechanical properties of original and degraded CI-nHA scaffolds were tested in the bioreactor with a 50 N load cell at a speed of 0.1 mm/s. The mechanical properties of original and degraded PCEC and CI-nHA@PCEC scaffolds were tested in the universal testing system with a 2 kN load cell and compressive grips at a speed of 0.1 mm/s. Scaffolds for wet condition tests were immersed in PBS solution for overnight before testing. Each sample were tested by using at least 6 scaffolds to get the average.

Bilayer composite scaffolds were only tested under wet conditions after immersion overnight in PBS solution. The mechanical properties of bilayer composite scaffolds were tested in the universal testing system with a 2 kN load cell and compressive grips at a speed of 0.1 mm/s. Cyclic compressions in wet conditions were carried out by compressing bilayer composite scaffolds up to strains of 5%, 10%, and 15% for 10 cycles at the speed of 0.1 mm/s. A minimum of 6 scaffolds were tested for each sample.

2.5. Degradation tests

2.5.1. Hydrophilicity test

The water contact angle of PCL and PCEC copolymers was measured by a Drop Shape Analyzer (DSA25S, KRÜSS). A drop of water (3 μL) was served on the surface of samples, and the image was immediately recorded. The behaviour of the drop and the material was recorded for 5 seconds, and the average and the

standard deviation were obtained. A minimum of 3 specimens were tested for each sample.

2.5.2. Accelerated degradation tests

Accelerated degradation tests were carried out in 5 M sodium hydroxide (NaOH, Sigma-Aldrich, Germany) solution at 37 °C to explore the degradation behaviour. Briefly, PCL and PCEC copolymer films with a diameter of 15 mm × 5 mm × 0.5 mm were placed into glass vials, respectively. Then 2 mL of 5 M NaOH solution was added to each vial to immerse the whole film. After tightly sealed, the vials were placed into an oven with a temperature of 37 °C. Samples were checked every 2 or 3 days to monitor the change in mass. To this end, samples were removed, washed with deionized water, and dried in a fume hood for 24 h. Then samples were weighed every time and put back to the glass vials. The process was repeated until the samples completely lost their structural integrity. A least 3 pieces of each sample were performed at the same time to obtain the average and standard deviation.

2.5.3. Physiological degradation tests

Degradation test was carried out in a 0.1 M PBS solution with a pH value of 7.15 at the physiological temperature of 37 °C, following the ISO 13781 standard [113,114]. Briefly, CI/II-HyA, PGS, CI/II-HyA@PGS, CI-nHA, PCEC and CI-nHA@ PCEC scaffolds with a dimension of 6 mm diameter and 3 mm height, and bilayer composite scaffolds with a dimension of 6 mm diameter and 6 mm height were placed respectively into 1.5 mL or 2 mL reaction tubes and filled with PBS at a proportion of at least 30 mL/g to ensure a complete immersion of scaffolds. Then, scaffolds were placed in an oven at 37 °C and checked every 1 or 2 weeks up to 8 weeks. At each time point, the pH was recorded using a pH meter (Sension + PH3, Hach, USA), and scaffolds were taken out, washed 3 times with deionized water, and dried at a fume hood for 24 h to obtain the change of mass.

2.6. Biocompatibility tests

2.6.1. Cell culture

2.6.1.1. Mouse fibroblast L929 cell line

A mouse fibroblast L929 cell line (ATCC-CRL-2593) was used for the cytocompatibility tests of PCL and PCEC copolymers. Cells were cultured in a complete medium consisted of high-glucose Dulbecco's modified eagle medium (DMEM, Gibco, USA), fetal bovine serum (FBS, Corning, USA), penicillin (100 units/mL, Invitrogen, USA) and streptomycin (100 µg/mL, Invitrogen, USA). Cells were used at 80 % of confluence and incubated at 37 °C with an atmosphere of 95 % air and 5 % CO_2.

2.6.1.2. Rat bone-marrow derived mesenchymal stem cells (MSC)

Rat mesenchymal stem cell (MSC) was isolated from the bone marrow of Wistar rats under the approval of the Royal College of Surgeons in Ireland Research Ethics Committee (REC Approval No. 237) [115,116]. Afterwards, cells from three separate pools of donors were expanded and cultured in completed culture medium (Dulbecco's Modified Eagle Medium (DMEM) + 10 % fetal bovine serum (FBS) + 100 U/mL penicillin/streptomycin (P/S) + 1% L-glutamine + 1% Glutamax + 1% non-essential amino acids) under normoxic cell culture conditions (37 °C, 5 % CO_2).

Once 70% confluent, cells were passaged using trypsin ethylenediaminetetraacetic acid (EDTA, Sigma-Aldrich, Ireland) and seeded on CI/II-HyA, PGS and CI/II-HyA@PGS scaffolds with a density of 5×10^5 cells per scaffold. Following 30 min incubation, scaffolds were cultured with 2 mL of culture expansion media for 24 h. The culture expansion media was then replaced with 2 mL of chondrogenic culture media including high-glucose DMEM with 50 µg/mL ascorbic acid, 40 µg/mL proline, 100 nM dexamethasone, 1×ITS, 0.11 mg/mL sodium pyruvate and 20 ng/mL human TGF-ß3 (Prospec, Israel) (components were supplied by ThermoFisher Scientific, Ireland, unless otherwise specified). The cell-seeded scaffolds were incubated for 28 days, with media changed twice weekly.

2.6.1.3. Mouse pre-osteoblast cell line MC3T3-E1

Mouse pre-osteoblast cell line MC3T3-E1 (ATCC-2593, USA) was expanded in completed culture medium (Minimum Essential Medium Eagle Alpha (α-MEM) + 10 % fetal bovine serum (FBS) + 100 U/mL penicillin/streptomycin (P/S)) for a confluence of 80%-90% in cell culture plate. Then, MC3T3 cells was seeded on CI-nHA and CI-nHA@ PCEC scaffolds at a density of 5×10^5 cells per scaffold in a 24-well plate and cultured in 2 mL completed culture medium at conditions of 37 °C, and 5 % CO_2. The cell-seeded scaffold was transferred to a new plate after one day of seeding and 2 mL of osteogenic culture medium (α-MEM + 10% FBS + 100 U/mL P/S + 50 µg/mL ascorbic acid + 10 mM β-glycerophosphate + 100 nM dexamethasone) were added and continued to an incubation for 28 days. Osteogenic culture media was changed every 3 or 4 days.

2.6.2. Indirect tests

Extracts of the PCL and PCEC copolymers were obtained by immersion of polymer films in complete culture medium with a ratio of 3 cm^2/mL and incubated at 37 °C for 72 h. Then, the samples were removed, and extracts were used for the cytocompatibility assay. To this end, L929 cells were seeded with a cell density of 1×10^4 cells/cm^2 and incubated at 37 °C for 24 h. Then, the culture medium was removed and replaced with diluted extracts (100%, 50%, 25%, 12.5%, 6.25% and 3.125%) and incubated for another 24 h. The mitochondrial activity was measured by adding thiazolyl blue tetrazolium bromide (MTT, Sigma-Aldrich, Germany) at a concentration of 5 mg/mL with a ratio of 10 µL by each 100 µL of complete culture medium. Afterwards, the cells were incubated under the same conditions for another 3 h and 100 µL dimethyl sulfoxide (DMSO, Sigma-Aldrich, Germany) was added in each well to dissolve the formazan crystals produced. Finally, the absorbance was measured in a microplate reader (Tecan Infinite M Plex, Switzerland) at a 570 nm wavelength. Cells without extract but with complete culture medium were used as the control. The mitochondrial activity was reported after normalizing the optical density (OD) of the cells exposed to the extracts with

respect the control (mitochondria activity (%) = (OD of sample / OD of positive control) × 100 %).

2.6.3. Direct tests

L929 cells were seeded at a cell density of 1×10^4 cells/cm^2 directly on the surface of the samples and incubated at 37 °C for 24 h. Afterwards, cells were fixed with paraformaldehyde (PFA 4%, Thermo Fisher Scientific, USA) at 37 °C for 25 min. Cell morphology was studied for immunofluorescent staining. After fixation, cells were treated with 0.1% of triton® X-100 (Thermo Scientific, USA) for 15 min and washed several times with Dulbecco's phosphate buffered saline (D-PBS, Corning, USA). Afterwards, cells were stained with Alexa Fluor 488 phalloidin (Invitrogen, USA) at a concentration of 1:300 to observe the cytoskeleton, and with DAPI (Invitrogen, USA) at a concentration of 1:1000 for the identification of the nucleus. After incubation under dark at room temperature for 1 h, the morphology of cells was observed under confocal microscopy (Olympus FV3000, Japan).

2.6.4. Cellular metabolic activity assay

An AlamarBlue assay (ThermoFisher Scientific, Ireland) was conducted to measure the metabolic activity of the cells within the CI/II-HyA, PGS, CI/II-HyA@PGS, CI-nHA and CI-nHA@ PCEC scaffolds. Scaffolds were initially washed in PBS twice and later cultured in fresh media containing 10% AlamarBlue viability reagent at 37 °C for 1 h (for MSC) or 3 h (for MC3T3 cells). A spectrophotometer (Victor2 D, Wallac, Boston, MA, USA) with an excitation wavelength of 550 nm and an emission wavelength of 590 nm was used to read the resulting fluorescence level. Media containing 10% AlamarBlue were used as a blank sample, subtracted from the experimental readings to eliminate background fluorescence. The cellular metabolic activity of cells grown on scaffolds at days 1, 3, 7, 14, 21, and 28 was measured.

2.6.5. DNA quantification assay

Cell-seeded CI/II-HyA, PGS, CI/II-HyA@PGS, CI-nHA and CI-nHA@ PCEC scaffolds were washed in PBS and digested in a papain enzyme solution prepared with 0.5 M EDTA, cysteine-HCl, and 1mg/mL papain enzyme (Carica papaya, Sigma-Aldrich, Ireland) at 60 °C for 12 h. Then the DNA concentration was determined using a Quant-iT™ PicoGreen® dsDNA assay kit (Invitrogen, UK).

2.7. Advanced biological assays

2.7.1. Chondrogenic assay

2.7.1.1. Sulfated glycosaminoglycan (sGAG) quantification

CI/II-HyA, PGS, and CI/II-HyA@PGS scaffolds were washed in PBS and digested in a papain enzyme solution prepared with 0.5 M EDTA, cysteine-HCl, and 1mg/mL papain enzyme (Carica papaya, Sigma-Aldrich, Ireland) at 60 °C for 12 h. The sGAG content within the scaffolds was measured using Blyscan sulfated glycosaminoglycan assay kit (Biocolor Life Sciences, UK), and determined using a standard curve at day 28 as per the manufacturer's instructions.

2.7.1.2. Histological analysis of cellular infiltration and sGAG distribution

Histological staining protocols were used to further evaluate cellular infiltration and sGAG distribution within CI/II-HyA, PGS, and CI/II-HyA@PGS scaffolds. Scaffolds were formalin-fixed for 1 h, treated with 1 mL of 15% sucrose for 2 h and 30% sucrose overnight, embedded in OCT (Fisher-Scientific, Ireland), and transversally sectioned at various depths on a cryostat (Leica RM 2255, Leica, Germany) to give 10 µm thick sections. These sections were mounted on PolysineTM glass slides (Fisher-Scientific, Ireland) and stained for Alcian blue (Sigma-Aldrich, Ireland), which stains sGAG blue, and nuclear fast red, which stains the cell nuclei red. The sections were successively imaged at several magnifications using a Leica DMIL microscope (Leica Microsystems, Switzerland).

2.7.1.3. Gene expression analysis

Quantitative reverse transcriptase polymerase chain reaction (qRT-PCR) was performed to determine the expression of specific genetic markers associated with chondrogenic lineage in CI/II-HyA, PGS, and CI/II-HyA@PGS scaffolds (Table 2.1). The total RNA was isolated from the cells within the scaffolds using a RNeasy kit (Qiagen, UK) and reverse transcribed to cDNA at a final concentration of 2.5 ng/µL using a QuantiTect reverse transcription kit (Qiagen, UK) on a thermal cycler (Mastercycler Personal, Eppendorf, UK). A QuantiTect SYBR Green PCR kit (Qiagen, UK) was used to run qRT-PCR reactions on a 7500 real-time PCR System (Applied Biosystems, UK) as previously described [117]. The relative expression of mRNA was calculated using the delta-delta Ct (ΔΔCt) method, where delta Ct (ΔCt) was the value obtained by subtracting the cycle threshold value (Ct) of a house-keeping gene from the Ct value of target mRNAs: aggrecan (ACAN), collagen type II alpha 1 chain (COL2A1) and collagen type I alpha 1 chain (COL1A1). The amount of target mRNA relative to the housekeeping gene was normalized to a calibrator sample to generate ΔΔCt. This was then converted to a fold increase in expression using the formula: Fold increase = $2^{-(\Delta\Delta Ct)}$. 18S ribosomal RNA (18S) was used as the housekeeping gene.

Table 2.1: List of gene transcripts analyzed by qRT-PCR. Qiagen QuantiTect validated primers used to analyze the expression levels of target genes.

Target gene	Catalogue code	Target gene reference
Collagen type 1 α1 chain (COL1A1)	QT01081059	Rn_Col1a1_1_SG
Collagen type 2 α1 chain (COL2A1)	QT01084118	Rn_Col2a1_1_SG
Aggrecan (ACAN)	QT00189518	Rn_Acan_1_SG
18S ribosomal RNA (18S)	QT02589300	Rn_Rn18s_1_SG

2.7.2. Osteogenic assay

2.7.2.1. Evaluation of alkaline phosphatase (ALP) activity

SensoLyte pNPP Alkaline Phosphatase Assay Kit Colorimetric (AnaSpec, USA) was used to check the ALP activity of CI-nHA and CI-nHA@ PCEC scaffolds. At days 7 and 14, scaffolds were washed with PBS and placed in 200 µL lysis buffer

containing 2% Triton X-100 (Sigma-Aldrich, Ireland) and 0.1M sodium acetate (Fisher Scientific, Ireland). Following by spinning at 10,000 g at 4 °C for 10 min, the obtained solutions were used to detect the ALP activity under the assay kit.

2.7.2.2. Evaluation of mineralization

Calcium (CPC) LiquiColor® Test Kit (Stanbio, USA) was used to quantify the calcium content from CI-nHA and CI-nHA@ PCEC scaffolds and cell mineralization. At days 21 and 28, cell-free and cell-seeded scaffolds were all washed with PBS and placed in 1 mL 0.5 M HCl solution (Honeywell Fluka, ThermoFisher Scientific, UK). Through shaking overnight at 4 °C, the obtained solutions were diluted 10 times for detecting the calcium content under the assay kit.

2.7.2.3. Histological analysis

Histological staining analysis were conducted to evaluate the cell cellular infiltration and calcium distribution within CI-nHA and CI-nHA@ PCEC scaffolds. Briefly, scaffolds with cells were firstly fixed in formalin (Epredia™, ThermoFisher Scientific, Ireland) for 1 h, then immersed in 15% sucrose solution (Sigma-Aldrich, Ireland) for 4 h and 30% sucrose solution for overnight. After embedded in OCT (Fisher-Scientific, Ireland), the slices with 10 µm thick were mounted on PolysineTM glass slides under cryostat (Leica RM 2255, Leica, Germany).

Slices were stained by using hematoxylin & eosin (H&E, Sigma-Aldrich, Ireland) to stain nucleus in dark purple to check the cell infiltration and alizarin red S (Sigma-Aldrich, Ireland) to stain calcium in red to check the mineralization, respectively. The histological staining images were obtained by observing these slices under microscope (Leica Microsystems, Switzerland).

2.7.2.4. Quantitative real-time PCR (qRT-PCR) analysis

Gene expression levels of specific markers associated with osteogenic lineage were determined in CI-nHA and CI-nHA@ PCEC scaffolds after 21 days in culture. The total RNA previously isolated was reverse transcribed to cDNA at a final concentration of 2.5 ng/µL using a QuantiTect reverse- transcription kit (Qiagen,

UK) and run on the 7500 real-time PCR system (Applied Biosystems, USA). The relative expression of mRNA was assessed using the Delta-delta Ct (ΔΔCt) method, in which four genes associated with osteogenesis (COL1A1, RUNX 2, OCN and BMP-2 (from QuantiTect Primer Assays, UK) were detected using GAPDH as a housekeeping gene, as shown in Table 2.2.

Table 2.2: List of qRT-PCR primers (Rat) for osteogenic study

Target gene	Catalogue code	Target gene reference
Collagen type 1 α1 (COL1A1)	QT01081059	Rn_Col1a1_1_SG
Osteocalcin (OCN)	QT00371231	Rn_Bglap_1_SG
Runt-related transcription factor 2 (RUNX2)	QT01300208	Rn_Runx2_1_SG
Bone morphogenic protein 2 (BMP-2)	QT00495096	Rn_Bmp2_1_SG
Glyceraldehyde-3-phosphate dehydrogenase (GAPDH)	QT01082004	Rn_Gapdhs_1_SG

2.7.3. Angiogenetic assay

Human endothelial cell line EA.hy 926 (ATCC-CRL-2922, USA) was used to check the angiogenesis of CI-nHA and CI-nHA@ PCEC scaffolds. Briefly, EA.hy 926 cells were seeded on scaffolds at a density of 1×10^5 cells per scaffold in a 24-well plate and cultured in 2 mL growth medium (high-glucose Dulbecco's modified Eagle's medium (DMEM) + 10 % fetal bovine serum (FBS) + 100 U/mL P/S) at conditions of 37 °C and 5 % CO_2. Scaffolds were transferred to a new plate after 24 h and cultured for 5 days with media change every 2 or 3 days.

After 1 and 5 days of incubation, staining with Alexa Fluor 488 phalloidin (1:300, Invitrogen, USA) and DAPI (1:1000, Invitrogen, USA) were performed and cell morphology was then observed under confocal microscope (Olympus FV3000, Japan) at magnification of 10x and 20x. Finally, three angiogenesis-related genes (VEGF, VE-cadherin (Integrated DNA Technologies, Belgium)) and MMP-2 (Sigma, USA) were evaluated by qRT-PCR, as shown in Table 2.3.

Table 2.3: List of qRT-PCR primers (Human) for angiogenetic study

Target gene	Sequence
Vascular endothelial growth factor (VEGF)	FWD: TGAACTTTCTGCTGTCTTGGGTGC
	RV: CAAACAAATGCTTTCTCCGCTCTG
Vascular endothelial-cadherin (VE-cadherin)	FWD: TGCCCACATATTCTCCTTTGAG
	RV: GAACCAGATGCACATTGATGAAG
Matrix metallopeptidase 2 (MMP-2)	FWD: GATACCCCTTTGACGGTAAGGA
	RV: CCTTCTCCCAAGGTCCATAGC
Glyceraldehyde-3-phosphate dehydrogenase (GAPDH)	FWD: TGTAGTTGAGGTCAATGAAGGG
	RV: ACATCGCTCAGACACCATG

2.8. Statistical analysis

All the data were recorded as mean ± standard deviation unless stated otherwise. Each experiment was carried out for at least triplicate samples. Statistical analysis was carried out using Origin software (2021b, OriginLab, Northampton, Massachusetts, USA) and GraphPad Prism (GraphPad Software 10.2.0, California USA) using a t-test was performed for two comparisons, and a general linear model one-way analysis of variance (ANOVA) with Fisher's LSD test analysis performed for multiple comparisons. p-values less than or equal to 0.05 ($p \leq 0.05$) were considered statistically significant. * Denotes $p \leq 0.05$, **$p \leq 0.01$, ***$p \leq 0.001$ and ****$p \leq 0.0001$.

3. Processing, structure and properties of PCEC copolymers

3.1. Introduction

Tissue engineering is currently considered an excellent approach to replace damaged tissue, and synthetic polymer scaffolds play a very important role in this task due to their similar structure and function to extracellular matrix (ECM) [118,119]. An ideal scaffold should physically and biologically mimic the structure and function of the target tissue. Specifically, the scaffold should provide adequate mechanical support for the damaged tissue and gradually degrade as new tissue grows. Besides, favourable biological properties are also required for tissue recovery [120–122]. However, the mismatch of mechanical properties and degradation rate [123,124], the presence of inflammatory degradation products [125,126], and difficulties to manufacture personalized scaffolds with precise pore interconnections [127,128] make it difficult to meet clinical use needs. Therefore, the development of materials with tailored mechanical properties and degradation rates that are suitable for different tissues and that can be used to fabricate customized and personalized scaffolds remains a significant challenge.

The emergence of 3D printing technologies provides broad prospects for the manufacture of personalized scaffolds for tissue engineering, since it can accurately and quickly fabricate scaffolds with precise geometry and high pore connectivity, similar to native tissues [129–133]. Among them, extrusion-based 3D printing is a common strategy because of low cost, simple and eco-friendly fabrication, high availability of materials (metals, ceramics, polymers, hydrogels and their composites) and diverse raw material to process (wires, pellets, and powders) [134–136]. In this context, some synthetic biodegradable polymers have attracted considerable attention over the past decades due to the high biocompatibility, ease of processing, as well as tailored mechanical properties and degradation rates [137–142]. For instance, poly(ε-caprolactone) (PCL), approved by the Food and Drug Administration (FDA), is widely used in bone regeneration

because of its mechanical properties, good biocompatibility, and easy processing due to the low melting temperature of ~ 60 °C [143–147]. However, PCL has a hydrophobic surface, which affects the degradation process that is reported to be between 2-3 years *in vivo*. The poor wettability also has a direct influence on the cell attachment and proliferation resulting in certain limitations in healthcare and medical applications [148–150].

As a nontoxic and water-soluble polymer, poly (ethylene glycol) (PEG) is often used for copolymerization or blending with PCL matrix to improve the hydrophilicity of PCL-based 3D-printed scaffolds, and some interesting results have been achieved [151–153]. Among them, PCL-PEG-PCL (PCEC) triblock copolymers synthesized from ring-opening polymerization (ROP) are attractive in tissue engineering due to the controlled synthesis and the flexibility of compositions, which allows to tailor the mechanical properties and degradation rate of PCL-based scaffolds [154–157]. However, most studies have focused on the regulation of PCEC copolymer composition in a narrow range and low molecular weights, because high molecular weights will lead to high viscosities, which are not appropriate for 3D printing, as well as to low degradation rates which are not compatible to tissue regeneration. In addition, to the best of our knowledge, the structure-property relationships of PCEC copolymers have not been systematically explored from the viewpoint of degradation rate, biological performance, and fabrication for tissue engineering applications, especially for macroinitiators of PEG with high molecular weight of 20k g/mol and 35k g/mol. Therefore, these studies are necessary to design and select PCEC copolymers and scaffolds that can be used for tissue engineering in different clinical applications.

This chapter of the thesis aims to manufacture and characterize biocompatible and biodegradable PCEC copolymers with high molecular weight using macroinitiators from low molecular weight PEG (0.6k g/mol) to high molecular weight PEG (35k g/mol). They are expected to cover a wide range of mechanical properties, degradation rates and biological performance, so they can be used in different applications. The composition, thermal properties, crystallization behaviour, mechanical properties, degradation rate, and biological

properties will be studied to establish the structure-property relationships of PCEC copolymers. Finally, the potential application in tissue engineering will be demonstrated by manufacturing them into scaffolds via a pellet-based screw-driven 3D printing system.

3.2. Processing and structure

PCL and a series of PCEC triblock copolymers with different PEG contents were successfully synthesized by the ring-opening reaction of ε-CL as the monomer, and EG or PEG as initiators using $Sn(Oct)_2$ as the catalyst (Figure 3.1a). PEG0.6k, PEG2k, PEG6k, PEG20k, and PEG35k were used as macroinitiators to assess the structure-property relationships as a function of PEG content on PCEC copolymers.

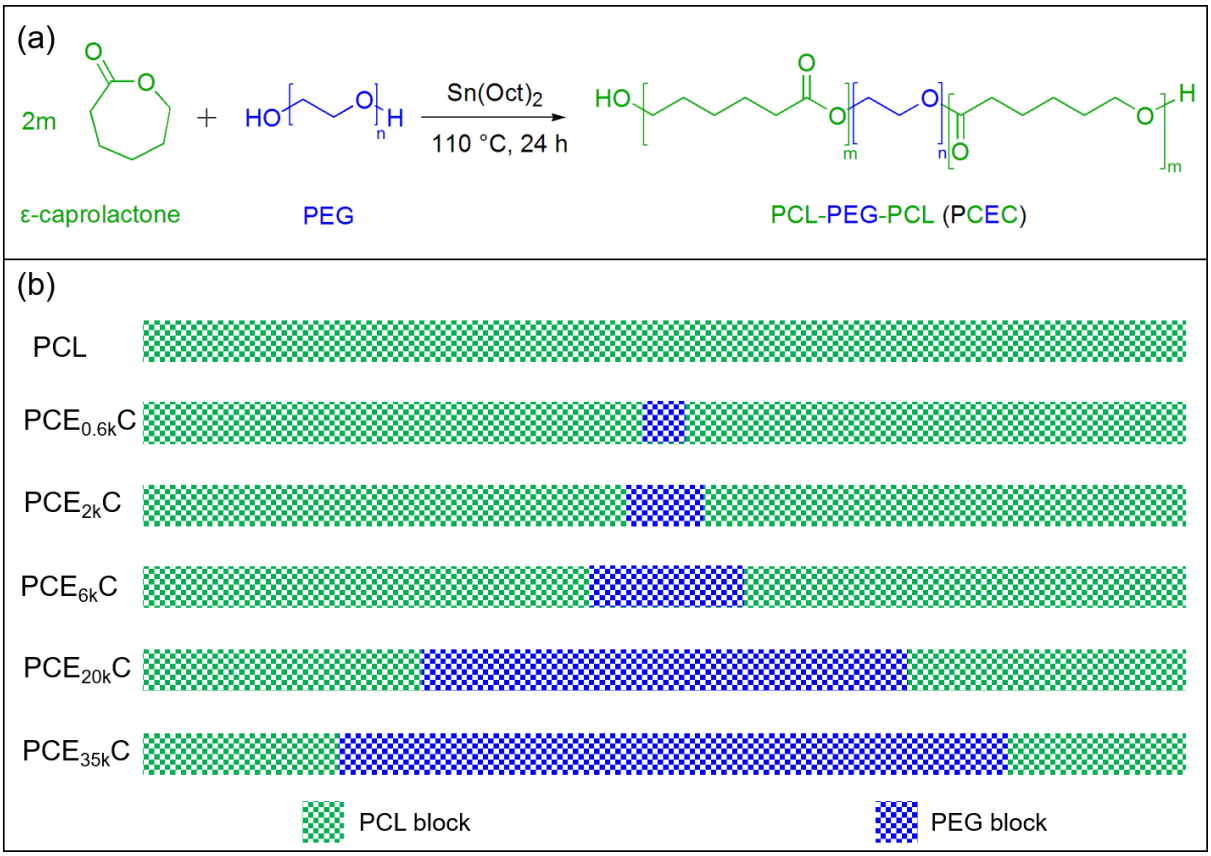

Figure 3.1: (a) synthesis route and (b) schematic diagram of the composition of PCL and PCEC copolymers.

^{1}H-NMR, ^{13}C-NMR, FT-IR, and GPC analysis were conducted to confirm the structure, composition and molecular weight of the synthesized block copolymers.

The assumed schematic diagram of blocks in PCEC copolymers is shown in Figure 3.1b. The structures and characteristic ^{1}H-NMR spectra of PCL and PCEC copolymers after purification are shown in Figure 3.2a, b, and c.

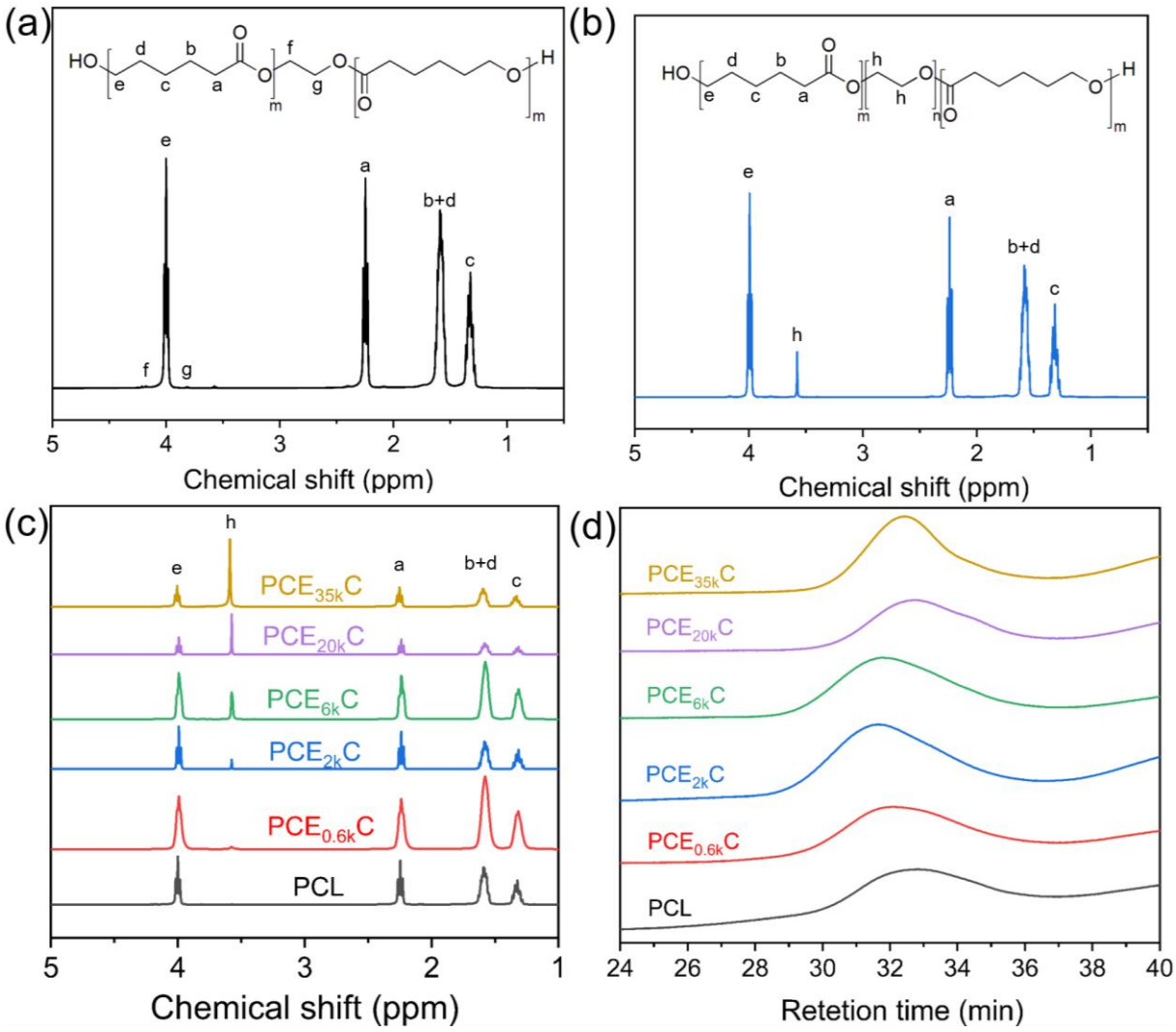

Figure 3.2: The ^{1}H-NMR spectra of (a) PCL, (b) $PCE_{2k}C$, (c) PCL and PCEC copolymers, and (d) GPC curves of PCL and PCEC copolymers.

The peaks at 4.05 ppm (peak e), 2.29 ppm (peak a), 1.59 to 1.68 ppm (peak b and d), and 1.33 to 1.41 ppm (peak c) in Figure 3.2a correspond to the methylene protons of the PCL blocks. In addition to the appearance of PCL block peaks, a typical peak appears in PCEC copolymers curves at 3.65 ppm (peak h), corresponding to the methylene protons of the PEG block [158] (Figure 3.2b and c). Furthermore, the appearance of characteristic peaks of the PCL block and PEG block in the ^{13}C-NMR and FT-IR spectrum also confirms the composition of the

PEG block and PCL block (Figure 3.3a and b). All this evidence indicates that PCEC copolymers made up of PEG and PCL blocks were successfully synthesized.

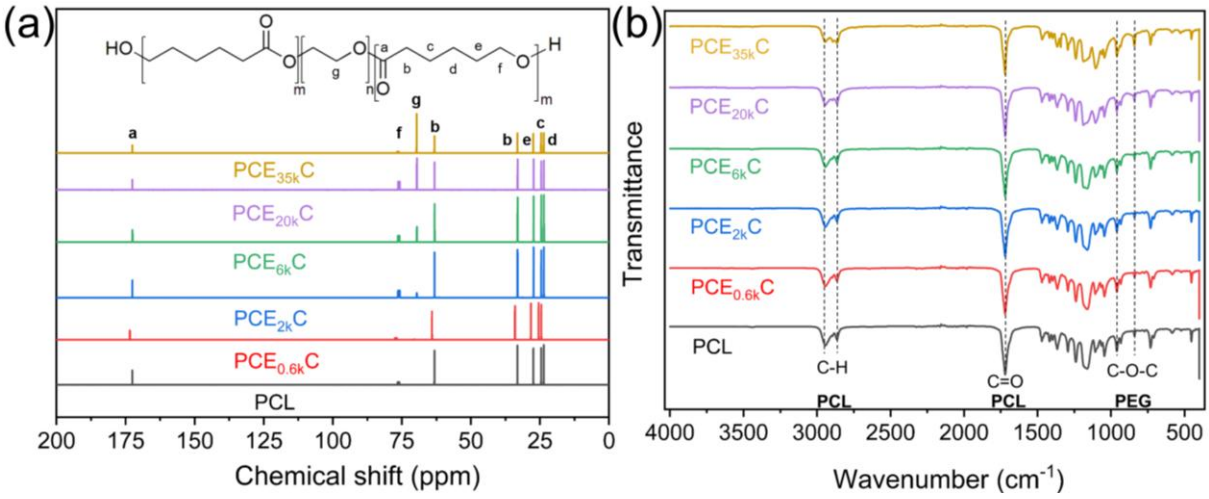

Figure 3.3: (a) ^{13}C-NMR and (b) FT-IR spectra of PCL and PCEC copolymers.

In addition, the proportions of PEG block and PCL blocks in the synthesized PCEC copolymers are also different due to the different molecular weights of the macroinitiator PEG. It can be seen in Figure 3.2c that the peaks of the PEG block became stronger with the increase in the molecular weight of PEG while the peaks of the PCL block became weaker, which is because the PEG content in the PCEC copolymers increased gradually. In order to figure out the specific proportions, PCL / PEG block ratios in PCEC copolymers were obtained from the calculation of the peak area ratio of e and h in ^{1}H-NMR (2m/n, where n refers to the polymerization degree (DP) of PEG block and 2m refers to the total DP of PCL blocks) (Figure 3.1a), and the results are depicted in Table 3.1. As the molecular weight of PEG increases, the ratio gradually decreases, corresponding to the increase of the PEG block and the decrease of the PCL block. It is worth noting that the ratio was close to 1 in PCE$_{20k}$C, indicating that the polymerization degree (DP) of these two blocks was nearly equal in the copolymer. Also, the DP of PCL block was smaller than that of PEG block (2m/n ratio <1) in PCE$_{35k}$C, demonstrating that the PEG block content occupies a significant part in copolymer. Therefore, these copolymers can be classified into three composition types according to the block content: (1) PEG

< PCL, (2) PEG ≈ PCL, and (3) PEG >PCL, as shown in Figure 3.1b. These different compositions will significantly affect the properties of the copolymers, as it will be discussed in detail below.

Table 3.1: Composition and molecular weight of PCL and PCEC copolymers

Sample	PCL/PEG block ratio [a]	M_n[b] (g/mol)	M_w[c] (g/mol)	Đ [d]
PCL	121.9	65 196	94 194	1.44
$PCE_{0.6k}C$	30.3	73 275	105 412	1.43
$PCE_{2k}C$	9.8	89 457	121 256	1.39
$PCE_{6k}C$	3.2	79 293	111 810	1.41
$PCE_{20k}C$	0.96	61 879	79 667	1.28
$PCE_{35k}C$	0.55	72 047	89 554	1.24

[a] PCL/PEG block ratio calculated from the peak area ratio of peak e and h in ^{1}H-NMR
[b] Number-average molecular weight (M_n) obtained from GPC
[c] Weight-average molecular weight (M_w) obtained from GPC
[d] Dispersity (Đ, M_w/M_n) obtained from GPC

GPC measurements were performed to determine the molecular weight of PCL and PCEC copolymers and the results are presented in Table 3.1. As shown in Figure 3.2d, all the relative curves of PCL and PCEC copolymers show a single peak of relative molecular weight. The PCL and PCEC copolymers exhibit high molecular weights within the range of 60k g/mol to 90k g/mol. These results prove that the synthesis is controlled and these PCL and PCEC copolymers can be used for comparison.

3.3. Thermal properties and crystallization behaviour

Thermal properties and crystallization behaviour are critical in tissue engineering because they can affect the mechanical properties and degradation rate. The thermal properties and crystallization behaviour of PCL and PCEC copolymers were studied by DSC, DMA and XRD (Figure 3.4), and the related data are listed in Table 3.2.

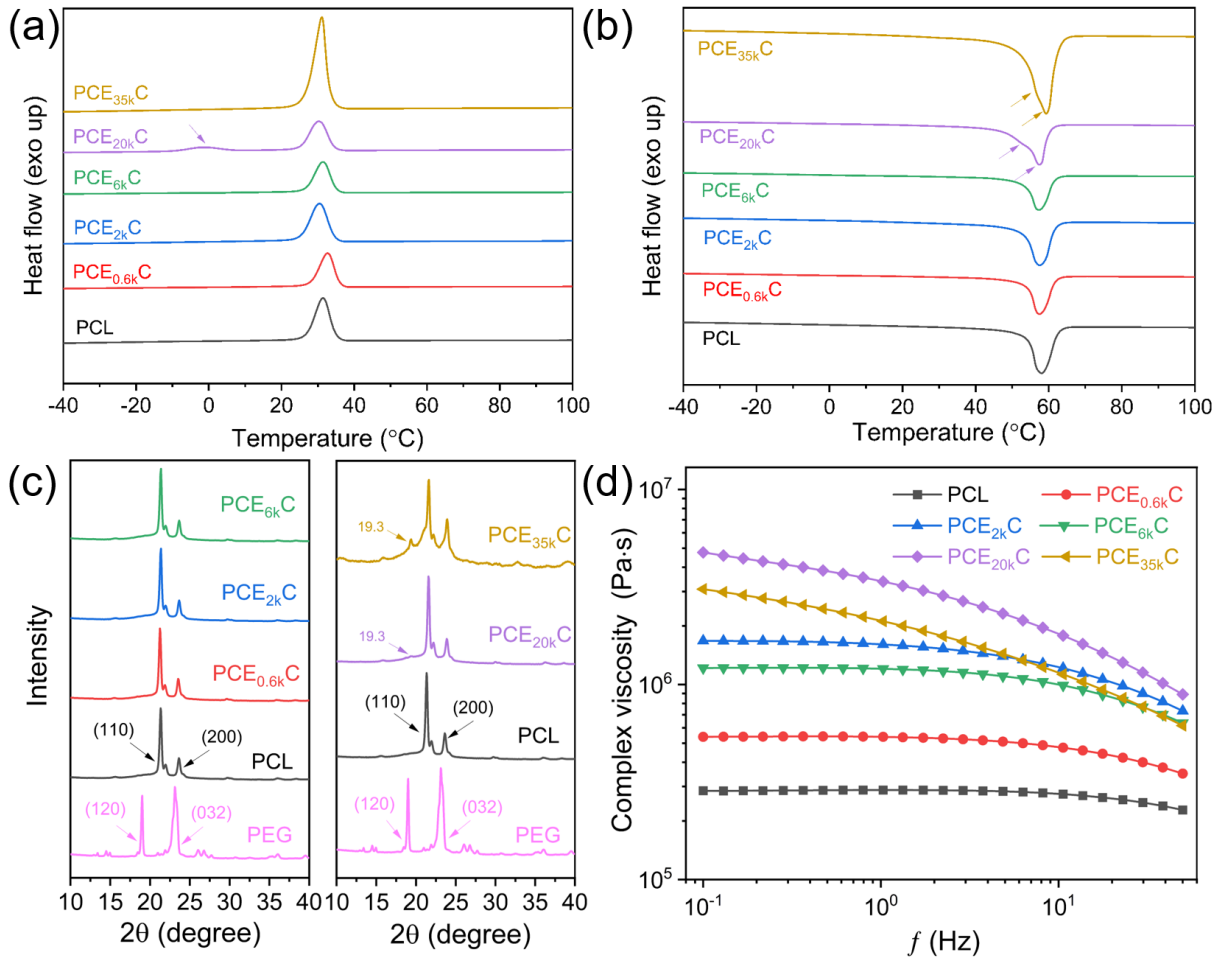

Figure 3.4: DSC curves of PCL and PCEC copolymers after removing the thermal history: (a) crystallization process and (b) melting process, (c) XRD spectra of PCL and PCEC copolymers and (d) complex viscosity of PCL and PCEC copolymers in rheology.

As shown in the DSC curves, $PCE_{0.6k}C$, $PCE_{2k}C$, and $PCE_{6k}C$ display a single crystallization temperature (T_c) at around 30 °C corresponding to the PCL block with a T_c of 31.4 °C (Figure 3.4a). Due to the small DP of the PEG blocks in these copolymers, the mobility of PEG blocks is affected by the crystallization of PCL blocks, thus leading to a single peak related to the PCL block. Besides, the PCL block content in the copolymer decreases with the increase of the PEG block content, leading to a reduction in the crystallization enthalpy (ΔH_c) of PCL from 64.0 to 57.8 J/g. The same tendency can also be observed in the melting process, as shown in Figure 3.4b and Table 3.2.

Table 3.2: Thermal properties of PCL and PCEC copolymers

Sample	T_g(°C)	T_c (°C)	T_m (°C)	ΔH_c (J/g)	ΔH_m (J/g)
PCL	-38.3	31.4	58.1	64.0	70.5
$PCE_{0.6k}C$	-39.2	32.7	57.4	62.6	67.6
$PCE_{2k}C$	-43.6	30.5	57.5	59.6	66.2
$PCE_{6k}C$	-45.8	31.3	57.3	57.8	62.1
$PCE_{20k}C$	-39.4	-2.1, 30.2	53.3, 57.3	10.3, 53.3	75.0
$PCE_{35k}C$	-41.4	31.0	59.4	79.7	89.0

When the PEG block content increases (PEG ≈ PCL), the crystallization of PEG begins to appear, resulting in two crystallization peaks in $PCE_{20k}C$, where the one at 30.2 °C corresponds to the PCL block and the other at -2.1°C stands for the crystallization of the PEG block. This result can also be confirmed from the overlapping melting peaks and a higher ΔH_m (melting enthalpy, 75.0 J/g). However, the actual T_c of PEG20k was around 45 °C according to DSC (Figure 3.5a). This reduced temperature comes from the crystallization of the PCL block at high temperature, which affects the mobility of the PEG block, leading to the difficulty in PEG crystallization. Conversely, when PEG > PCL, PEG block crystallization dominates and appears as a sharp peak similar to the crystallization peak of the PEG block (Figure 3.5a) in $PCE_{35k}C$, but with a higher ΔH_c of 79.7 J/g due to the joint contribution of PEG and PCL blocks. The overlap also appears in the melting process of $PCE_{35k}C$, which exhibits a higher ΔH_m = 89.0 J/g. Besides, it also can be confirmed by the change of the glass transition temperature (T_g) from DMA (Figure 3.5b and Table 3.2). When PEG < PCL, the crystallization enthalpy of the copolymers decreased with the increase of PEG block content, resulting in the decrease in T_g. While the T_g of the copolymer increases when the crystallization of PEG begins to appear. This is because the T_g of the copolymer decreases as the crystallinity of the copolymer decreases, which is consistent to the results of DSC.

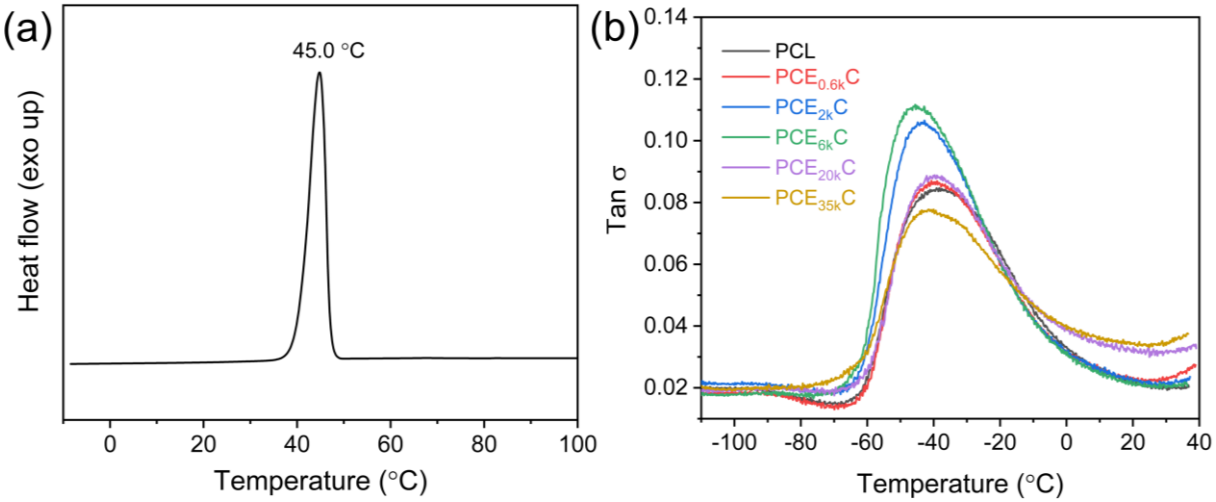

Figure 3.5: (a) DSC curves of PEG20k (crystallization process) and (b) DMA curves of PCL and PCEC copolymers.

To gain insight into the crystallization behaviour of these block copolymers, X-ray diffraction (XRD) was performed. As shown in Figure 3.4c, the peaks at 21.3° and 23.6° corresponded to (110) and (200) crystal planes of PCL block, while the peak at 19.0° and 23.1° related to (120) and (032) crystal planes of PEG block [159]. Only peaks corresponding to the PCL block appear when PEG < PCL, indicating the crystallization of PEG block with lower DP is restricted by the PCL block crystallization. A small peak corresponding to the PEG block crystallization appears at 19.3° when PEG ≈ PCL, because of the increased DP of PEG block in $PCE_{20k}C$. More importantly, both peaks corresponding to the PEG block and the PCL block appears clearly in $PCE_{35k}C$ when PEG > PCL, providing strong evidence of the joint contribution of PEG and PCL blocks and the overlap phenomenon observed in DSC.

3.4. Rheological behaviour

The rheological behaviour of the material is a key factor for extrusion-based 3D printing because it determines printability. In particular, the shear thinning behaviour is beneficial to 3D printing, because the low viscosity under high-frequency shear is conducive to the extrusion of the material and prevents the nozzle clogging. On the contrary, the high viscosity under low-frequency shear is

beneficial to maintain the shape after deposition to prevent microstructure collapse.

The rheology of PCL and PCEC copolymers was explored, and the results are plotted in Figure 3.4d. PCL shows a typical Newtonian behaviour that was frequency-independent in the low frequency region. It was interesting to see that the PCEC copolymers show a PCL Newtonian behaviour when PEG < PCL, while they exhibit an obvious shear-thinning phenomenon when PEG ≥ PCL, which is the key factor for extrusion-based 3D printing. This special performance comes from the increase of the flexible PEG blocks, which improve the flexibility of the copolymer chain, leading to decreased viscosities at high shear frequency. Moreover, higher moduli G' of $PCE_{20k}C$ and $PCE_{35k}C$ appear at low shear frequency, making them more suitable to obtain a stable microstructure after deposition (Figure 3.6). These results demonstrate that the rheological properties of PCEC copolymers can be optimized for the 3D printing by carefully controlling the composition. Furthermore, it also provides an effective method to improve the rheological properties of PCL-based polymers without reducing the molecular weight or blending with other materials.

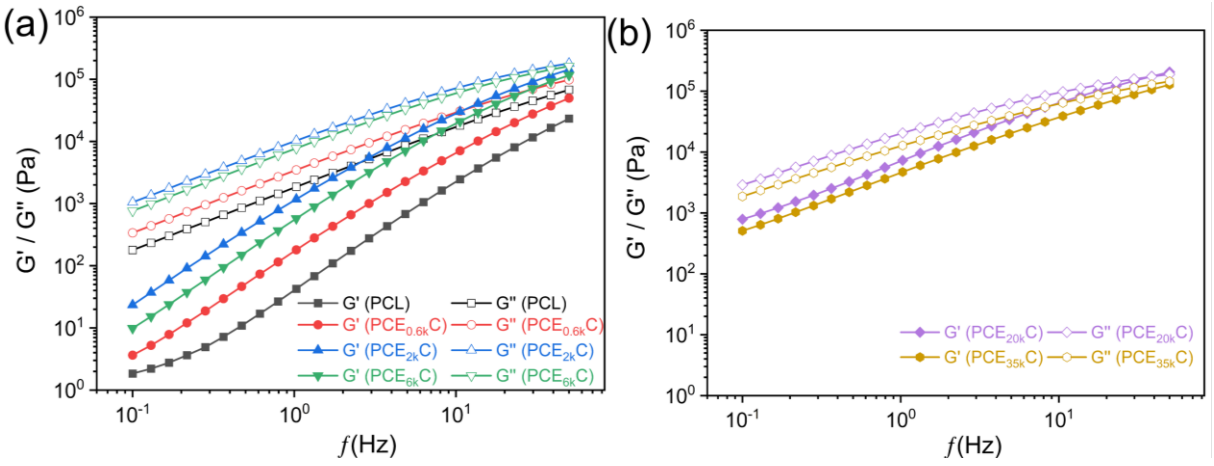

Figure 3.6: Storage modulus G' and loss modulus G" obtained from rheology. (a) PCL, $PCE_{0.6k}C$, $PCE_{2k}C$ and $PCE_{6k}C$ and (b) $PCE_{20}kC$ and $PCE_{35}kC$.

3.5. Mechanical properties

Tensile tests were carried out to ascertain the mechanical properties of PCL and PCEC copolymers. All copolymers showed an initial elastic region, followed by plastic deformation after the yield point, leading to a large elongation to fracture (Figure 3.7a).

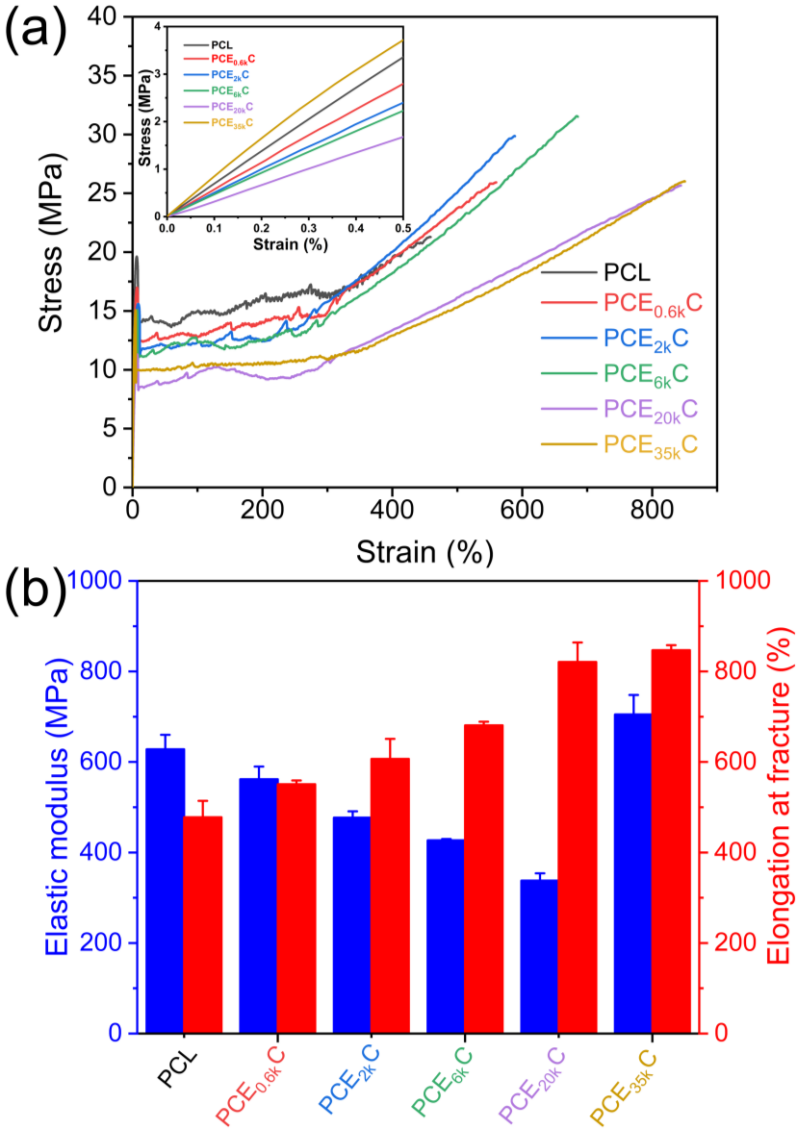

Figure 3.7: (a) Typical stress-strain curves and (b) tensile properties of PCL and PCEC copolymers.

The elastic modulus of PCEC copolymers decreases while the elongation at fracture increases with the increase of PEG block content if PEG ≤ PCL (Figure 3.7b). This trend behaviour comes about because PCL block dominates in the

crystallization of theses copolymers due to the lower DP of PEG block, the reduced PCL block content decreases the crystallinity, resulting in lower elastic modulus. However, the crystallization of the PEG block dominates when PEG > PCL, and the combination of the PEG and PCL blocks leads to a higher crystallinity, resulting in higher elastic modulus. Although the mechanical properties are usually related to the molecular weight of polymers, it can be seen from Table 3.3 that the molecular weights of PCL and PCEC are similar, which indicates that the mechanical properties of PCEC copolymers are mainly influenced by different crystallization behaviours. It is interesting to notice that the elastic modulus of PCEC copolymers can be controlled in a wide range from 338 MPa to 705 MPa by adjusting the molecular weight of macroinitiator PEG, without reducing the molecular weight and elongation at fracture. Thus, these PCEC copolymers have a large potential to manufacture scaffolds for cancellous bone (~ 400 MPa), tendon (~ 560 MPa) and collateral ligament (~ 366 MPa) in the tissue engineering, taking into account their large elongation at fracture.

Table 3.3: Tensile parameters of PCL and PCEC copolymers

Sample	Elastic modulus (MPa)	Strength (MPa)	Elongation at fracture (%)
PCL	628±32	21.0±1.8	478±36
$PCE_{0.6k}C$	562±28	26.1±1.1	551±8
$PCE_{2k}C$	477±14	32.7±3.7	607±44
$PCE_{6k}C$	427±3	30.4±0.8	681±8
$PCE_{20k}C$	338±16	25.4±0.6	821±43
$PCE_{35k}C$	705±43	25.6±0.9	847±11

3.6. Degradation behaviour

3.6.1. Wettability

Water contact angles were explored before degradation tests to determine the surface hydrophilicity of PCEC copolymers, as it directly affects the degradation rate and cell behaviour. PCL, $PCE_{0.6k}C$ and $PCE_{2k}C$ showed similar contact angles

of 84.2°, 87.3° and 87.1°, respectively, representing a hydrophilic behaviour (contact angle lower than 90°) (Figure 3.8a). The increase of the PEG block content in this range was insufficient to increase the hydrophilicity significantly. The contact angle begins to significantly drop from $PCE_{6k}C$ (73.4°, $p<0.0001$), and when PEG ≥ PCL, $PCE_{20k}C$ and $PCE_{35k}C$ show excellent hydrophilicity, with contact angles of 45.2° ($p<0.0001$) and 65.4° ($p<0.0001$), respectively. This is due to the increase of the presence of the highly hydrophilic PEG blocks. Notably, $PCE_{35k}C$ with higher PEG content shows a contact angle higher than that of $PCE_{20k}C$ due to the joint contribution of crystallization discussed before, which makes it more difficult for water to diffuse on the surface. These results indicate that the hydrophilicity can be changed in a wide range by adjusting the PEG block content, providing a useful strategy to tailor the degradation rate and cell behaviour.

3.6.2. *In vitro* accelerated degradation properties

The degradation rate is a vital factor for biomedical applications as it will directly affect the *in vivo* performance of the scaffolds. The degradation mechanism of PCL under physiological conditions (water or PBS solution) is bulk erosion. The sample first experiences a reduction in molecular weight, which later leads to the loss of mass. The degradation rate is not constant in bulk erosion, because of the complexity of degradation process [160]. However, the degradation mechanism of PCL in the alkaline environment with high pH is surface erosion. Under these conditions, the mass loss appears in the initial stage and the degradation rate are linear [161,162]. This constant degradation rate facilitates the comparison of the degradation among different materials. Therefore, accelerated degradation tests were performed by immersing PCEC copolymer films in 5M NaOH solution (pH = 13) at 37 °C in this study. The degradation was monitored by measuring the residual mass over time until structural integrity was lost (Figure 3.8b).

When PEG < PCL, PCL, $PCE_{0.6k}C$ and $PCE_{2k}C$ show similar degradation rates with ~70% mass loss retained structural integrity after 23 days, while $PCE_{6k}C$ shows a faster degradation rate, with about 90% mass loss after 20 days and loss of structural integrity after 23 days. Surprisingly, when PEG ≥ PCL, $PCE_{20k}C$ and

$PCE_{35k}C$ exhibit extremely fast degradation rates and they were fully degraded within 1 day, so that samples were checked every 2 h. $PCE_{20k}C$ and $PCE_{35k}C$ show ~60% mass loss after 8 h and lost their structural integrity after 10 h (Figure 3.8c). These phenomena were consistent to the results of hydrophilicity. During the degradation process, the hydrophilic PEG blocks were more likely to be released into the solution, leading to the formation of holes, which facilitate the ingress of water and accelerate the hydrolysis of the PCL block. However, the PEG blocks did not completely disappear due to surface erosion but were gradually degraded as the thickness decreased. Therefore, it demonstrates that the apparent degradation rate of PCEC copolymers can be significantly affected by the PEG block content over a wide range, which broadens the design space of biomaterials with controllable degradation rates.

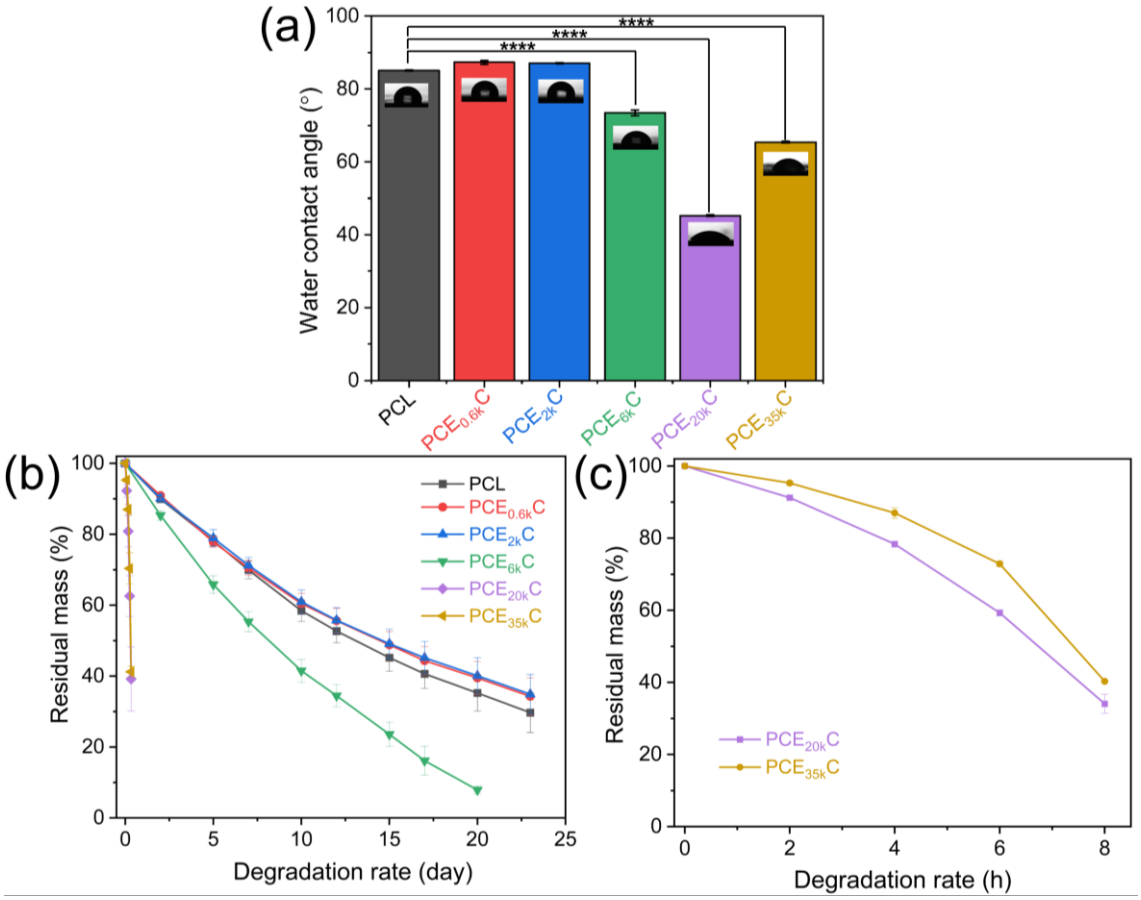

Figure 3.8: (a) Water contact angles of PCL and PCEC copolymers, (b) Residual mass of PCL and PCEC copolymers after immersion in NaOH solution for 23 days, and (c) Residual mass of $PCE_{20k}C$ and $PCE_{35k}C$ after immersion in NaOH solution for 8 hours.

3.7. Biological performance

Cytotoxicity of PCL and PCEC copolymers was tested by MTT assay. To this end, different diluted extracts (100%, 50%, 25%, 12.5%, 6.25%, and 3.125%) were used to incubate L929 cells at a concentration of 1×10^4 cells/cm^2 for 24 h. The mitochondrial activity of PCL and PCEC copolymers was normalized by the obtained value of the control and the relationship between the mitochondrial activity at function of the dilution is plotted in Figure 3.9 for all copolymers. PCL and PCEC copolymers present a mitochondrial activity above 70%, which is the lowest limit to consider the material cytotoxic according to ISO10993-5. Thus, all copolymer present excellent biocompatibility, and there was no significant difference between them, which indicates that the composition of PCEC copolymer has no effect on the material cytotoxicity.

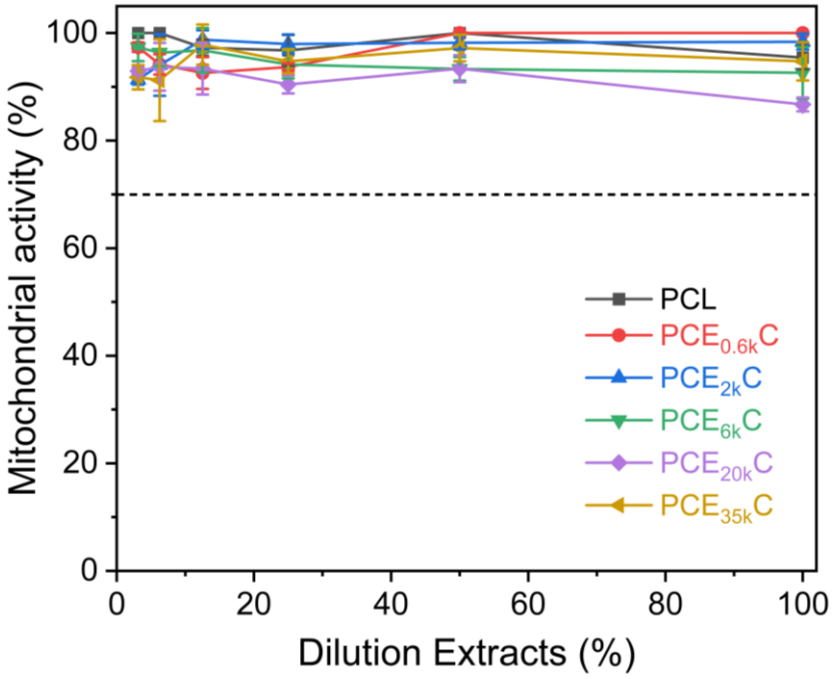

Figure 3.9: Mitochondrial activity of the L929 cells after 72 h of incubation in the extracts obtained from PCL and PCEC copolymers immersed in culture medium.

The homogeneity of the polymer films was observed by atomic force Microscope (AFM). As shown in Figure 3.10, all samples present smooth surfaces, and the differences in surface morphology come from the roughness of the hot-pressed plate and possibility from the removal of material during the release of the

hot-pressed films. However, the overall roughness is relatively homogeneous, and the average roughness (Ra) is between 0.35-1.76 µm, which does not affect the proliferation and growth of cells with size of 15-30 µm.

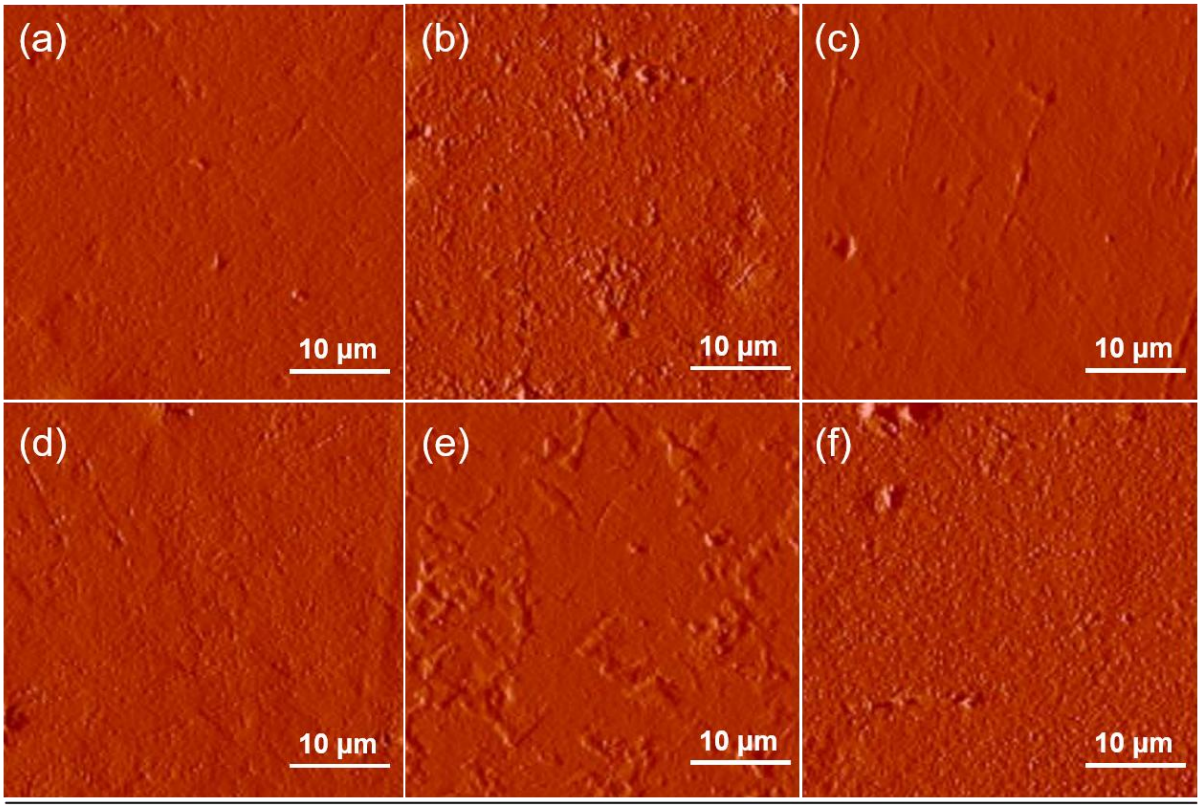

Sample	PCL	$PCE_{0.6k}C$	$PCE_{2k}C$	$PCE_{6k}C$	$PCE_{20k}C$	$PCE_{35k}C$
Ra (µm)	0.64	0.35	1.25	1.34	1.76	0.40

Figure 3.10: AFM images of PCL and PCEC copolymer films and the data of average surface roughness (Ra). (a) PCL, (b) $PCE_{0.6k}C$, (c) $PCE_{2k}C$, (d) $PCE_{6k}C$, (e) $PCE_{20k}C$ and (f) $PCE_{35k}C$.

The results of the direct interaction between PCL or PCEC copolymers and L929 cells after 24 h of incubation is depicted in Figure 3.11. Cells are viable on both PCL and PCEC copolymers and they display the typical morphology of L929 cells, indicating that these materials were biocompatible. Moreover, the quantity and quality of cell spreading seems to be improved with the increase in PEG content, and more cells with extended cytoplasmic projections appear, indicating enhanced cell adhesion, especially starting from $PCE_{6k}C$. This may be because the increase of PEG improves the hydrophilicity and surface energy, resulting in easier cell spreading and migrating on the material. These results confirm that the

increased PEG content has an indirect effect on cell attachment and proliferation in PCEC copolymers.

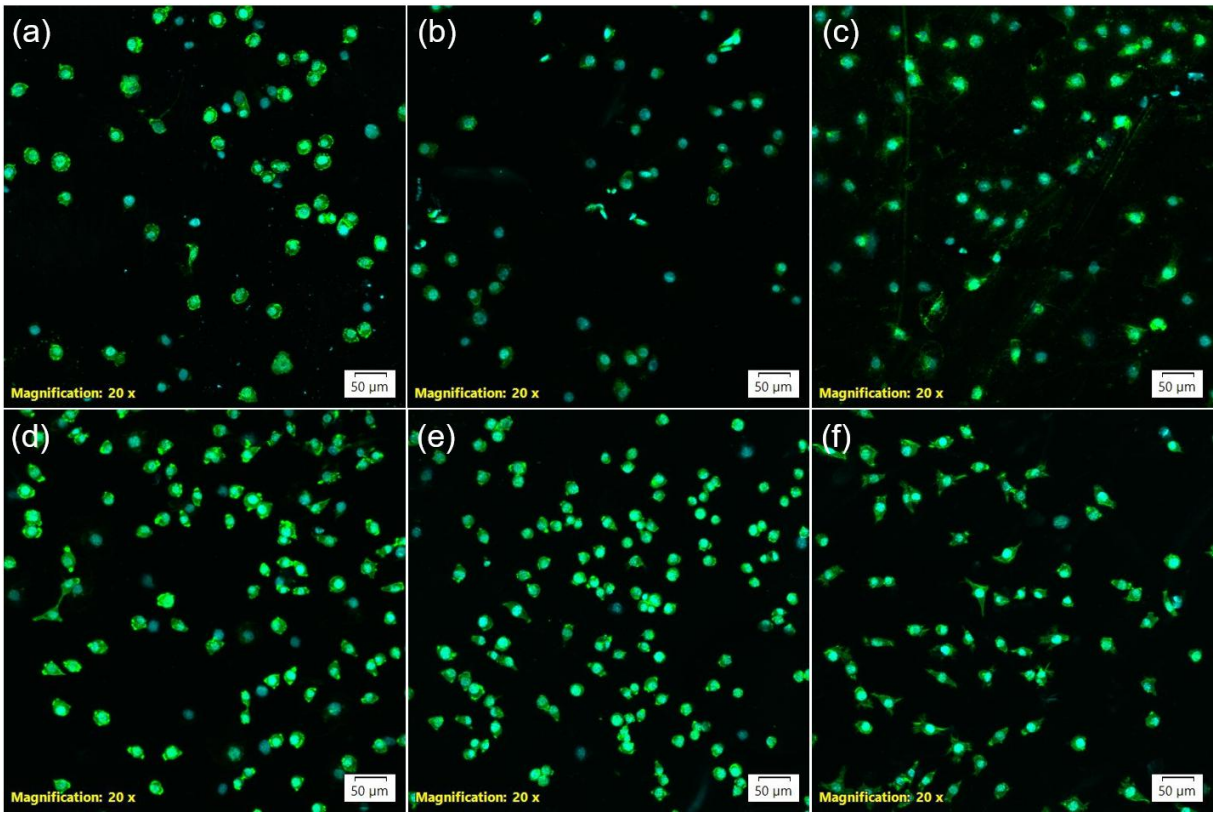

Figure 3.11: Confocal microscopy images of the interaction between L929 cells and the surface of polymer films for 24 h. (a) PCL, (b)$PCE_{0.6k}C$, (c)$PCE_{2k}C$, (d)$PCE_{6k}C$, (e)$PCE_{20k}C$ and (f) $PCE_{35k}C$.

3.8. PCEC copolymer scaffolds

3D-printed PCEC copolymer scaffolds were fabricated by pellet-based screw-assisted 3D printing system. It is highly tolerant to the shape of the material, such as powders, pellets, or gels. Compared with the commonly used fused deposition modelling (FDM) system, it reduces the cumbersome process of making uniform filaments, which is simpler and more efficient for manufacturing. The printing parameters of 3D printing were greatly influenced by the rheological behaviour, especially the extrusion flow rate, which is directly related to the viscosity. As shown in Figure 3.4d, with the increase of PEG content, the PCEC copolymers show increased complex viscosities, which indicates higher extrusion rates are

required to obtain a smooth printing process. However, due to the shear thinning behaviour, even though $PCE_{20k}C$ and $PCE_{35k}C$ exhibit high viscosities, they can be extruded at low extrusion flow rates, improving printing efficiency and reducing nozzle clogging issues. PCL and PCEC copolymers can be all printed into scaffolds with precise geometry and high pore connectivity. Taking $PCE_{20k}C$ as an example, 3D-printed scaffolds with different sizes, number of layers, and porosity were displayed in Figure 3.12.

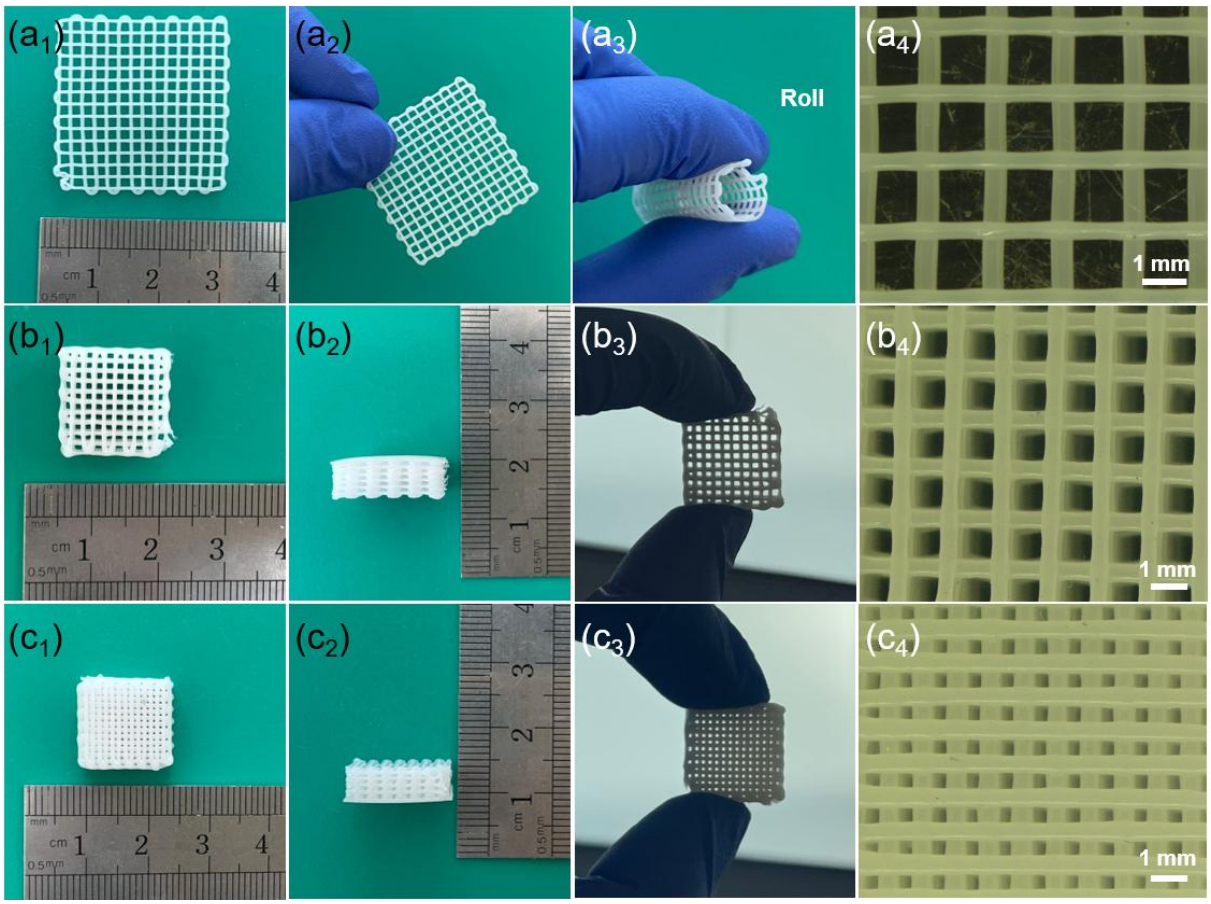

Figure 3.12: Digital photos and optical microscopy images of the 3D-printed $PCE_{20k}C$ scaffolds. (a) a 2-layered sheet, (b) a 10-layered scaffold with 1000 μm porosity and (c) a 10-layered scaffold with 500 μm porosity.

Because of the flexibility of $PCE_{20k}C$, the 2-layer sheet shows excellent bending performance, which can be curled or bent multiple times without damage after recovery, showing potential for applications in joint tissue engineering. In addition, scaffolds with smaller dimensions and more complex pore structures can also be obtained. It can be seen from the optical microscopy images that, the

printed filaments of the scaffolds are smooth and uniform, cylindrical in shape, with a diameter of ~ 500 μm close to the designed size. The printed scaffolds also show a well-defined and interconnected porous network structure, and their sizes were also close to the designed 1000×1000 μm and 500×500 μm, respectively. Besides, no collapse of filaments and pore clogging are observed on the top surface of the scaffolds, indicating their good printability. These results confirm the usability of PCEC copolymers in 3D-printed scaffolds.

3.9. Conclusions

In this Chapter, biodegradable and biocompatible PCEC copolymers with tunable mechanical properties and degradation rate were synthesized by using macroinitiators ranging from low molecular weight PEG (0.6k g/mol) to high molecular weight PEG (35k g/mol). Three different crystallization regimes were found depending on PCL/PEG block ratio which significantly affected the mechanical properties. The elastic modulus of the copolymers could be tuned between 338-705 MPa, close to the value of cancellous bone, tendon, and collateral ligament, while the elongation to fracture was always >500%. The surface hydrophilicity and degradation rate were directly related to the PEG content. PCEC copolymers with higher PEG content showed higher hydrophilicity, faster degradation rate, and improved cell attachment. In fact, $PCE_{20k}C$ and $PCE_{35k}C$ copolymers exhibited extremely fast apparent degradation rates in 5M NaOH solution. Moreover, all PCEC copolymers could be manufactured into 3D scaffolds with controlled microstructure, particularly $PCE_{20k}C$ and $PCE_{35k}C$ which exhibit excellent shear-thinning rheological properties. These results show that is possible to tailor the mechanical properties, degradation rate and hydrophilicity of PCEC copolymers to adapt the properties of the copolymers to different native tissues, and they also provide a strategy for the design and selection of other copolymers for biomedical applications.

4. Processing, structure, and properties of CI/II-HyA@PGS composite scaffold

4.1. Introduction

Cartilage defects caused by trauma or disease negatively affect the quality of life of over 500 million people worldwide and effective treatments remain a significant challenge in clinical applications in recent 10 years [163,164]. Cartilage tissue is a porous-viscoelastic connective tissue populated by a low density of chondrocytes embedded in a dense extracellular matrix (ECM), substantially limiting their mobility and ability to repair damaged tissue [165,166]. The lack of nerves and blood vessels in its structure remains a big contributing factor that ultimately leads to ineffective cartilage repair with the consequent formation of low-quality hyaline tissue, which is unable to satisfy its function [167–169]. Although traditional surgical treatments consisting of autografts and allografts can be effective on a short-term basis (<5 years), clinical success in the long-term over 5 years is poor and ultimately can lead to full knee arthroplasty or revision surgery in patients [170]. In this regard, tissue engineering has drawn a lot of attention in recent 20 years, with some cartilage-engineered scaffolds showing promising alternatives [171,172]. Despite some success in supporting chondrogenesis and cartilage-like matrix formation, most scaffolds still display unmatched mechanical properties and degradation rates with native cartilage, greatly affecting tissue repair efficiency [173]. Consequently, there is a need to develop scaffolds that simultaneously meet the requirements of mechanical support for cartilage growth, stimulation of chondrogenesis, and of maintaining structural and mechanical stability during tissue regeneration.

The combination of the manufacturing technique and the material selection allows the design of scaffolds with suitable properties to fulfil the requirements of tissues. For instance, features such as shape design and macro/microstructure can be controlled using 3D-printing technologies. Complementarily, the raw materials

provide the overall mechanical properties, biological functionality, and degradation rate of the scaffolds [174–176]. To this end, biodegradable synthetic polymers such as poly(caprolactone) (PCL), poly(lactic acid) (PLA), and poly(lactic-co-glycolic acid) (PLGA) with tailored mechanical properties, degradation rates, and ease of processing have been widely used in 3D-printed scaffolds for cartilage tissue engineering [94,177,178]. However, high modulus and inelastic behaviour, slow degradation rates, and acidic degradation products are not conductive to tissue repair and limit their suitability. In this regard, a biocompatible elastomer, poly (glycerol sebacate) (PGS), a biocompatible elastomer with flexible and elastic mechanical behaviour has been considered as a suitable material for cartilage defect repair [179]. You's group used a step-by-step curing process to successfully fabricate 3D-printed porous PGS scaffolds and applied them to tissue engineering such as heart, bone, and cartilage [107,180,181]. Depending on the printing parameters and micropore sizes, the elastic modulus of PGS scaffolds can be varied from 150.7 to 239.4 kPa, thus approaching the physiological range of healthy articular cartilage (0.1-2 MPa). Meanwhile, PGS exhibit excellent fatigue resistance under dynamic deformations, which is suitable for joint tissue repair [107,182,183]. Nevertheless, like most biodegradable synthetic polymers, PGS shows low bioactivity due to the lack of bioactive sites, which limits its applications in biomedical and healthcare applications.

To improve the bioactivity, attention has been paid to the functionalization of 3D-printed biodegradable polymer scaffolds by incorporating bioactive matrices to obtain biomimetic structures [172,184–187]. In this context, ECM-based materials, such as collagen, are considered good candidates due to their excellent biocompatibility and biodegradability properties, but more importantly, because of their ability to direct cell-binding to the ECM and appropriate matrix deposition [131,188–190]. A pro-chondrogenic matrix formed by incorporating collagen type II and hyaluronic acid (key articular cartilage ECM components) into a collagen type I has been proved to direct mesenchymal stem cell (MSC) chondrogenesis, thereby leading to enhanced hyaline-like cartilage formation while inhibiting late-stage differentiation events and MSC hypertrophy [110,191]. Furthermore, it has

been observed in some animal models (e.g., rabbits, goats, and horses) that when this matrix is incorporated into a multilayered collagen-based scaffold, it exhibits a robust ability to drive efficient, high-quality cartilage repair [192–194]. However, despite some progress, its chondrogenic potential and clinical therapeutic application are only involved in small defects repair, due to the limited mechanical properties. Therefore, it remains a challenge to design scaffolds for large cartilage defect repair that satisfies the requirements of biomimicking mechanical properties and chondrogenic bioactivity, and that presents a degradation rate that matches cartilage regeneration in order to ensure long-term integration and stability.

This chapter aims to propose a novel biomimetic composite scaffold (CI/II-HyA@PGS) with hierarchical porosity by directly incorporating a pro-chondrogenic collagen type I/II and hyaluronic acid (CI/II-HyA) matrix in a 3D-printed PGS scaffold framework. The porous CI/II-HyA matrix provides the biological cue to stimulate MSC chondrogenesis, while the PGS scaffold provides the mechanical enforcement to support new cartilage tissue growth. The mechanical properties in dry and wet conditions will be studied under compression, while cyclic compression under different applied strains will be performed simultaneously to evaluate the fatigue resistance property. The structural, mass, and mechanical stability after degradation will be analysed by immersion in PBS solution for up to 8 weeks. Finally, the proliferation and differentiation of rat-derived MSCs on these scaffolds will be systematically studied for up to 28 days *in vitro* to explore the chondrogenic capacity of the novel CI/II-HyA@PGS composite scaffold.

4.2. Processing and structure

An innovative composite scaffold CI/II-HyA@PGS with a hierarchical porosity was developed by using a pre-chondrogenic CI/II-HyA matrix served as a biological cue to stimulate MSC chondrogenesis, and an elastic 3D-printed PGS scaffold served as mechanical enforcement to support cartilage growth. Briefly, the CI/II-HyA@PGS scaffold was fabricated by soaking the 3D-printed PGS scaffold in the mixed solution of collagen type I/type II (total collagen

concentration of 0.5% w/v at ratio 1:1) and hyaluronic acid (HyA) at a concentration of 0.05% w/v, prior to being freeze-dried to a final temperature of -20 °C. The complete process of manufacturing, functionalization and evaluation of the CI/II-HyA@PGS scaffold is summarized in Figure 4.1.

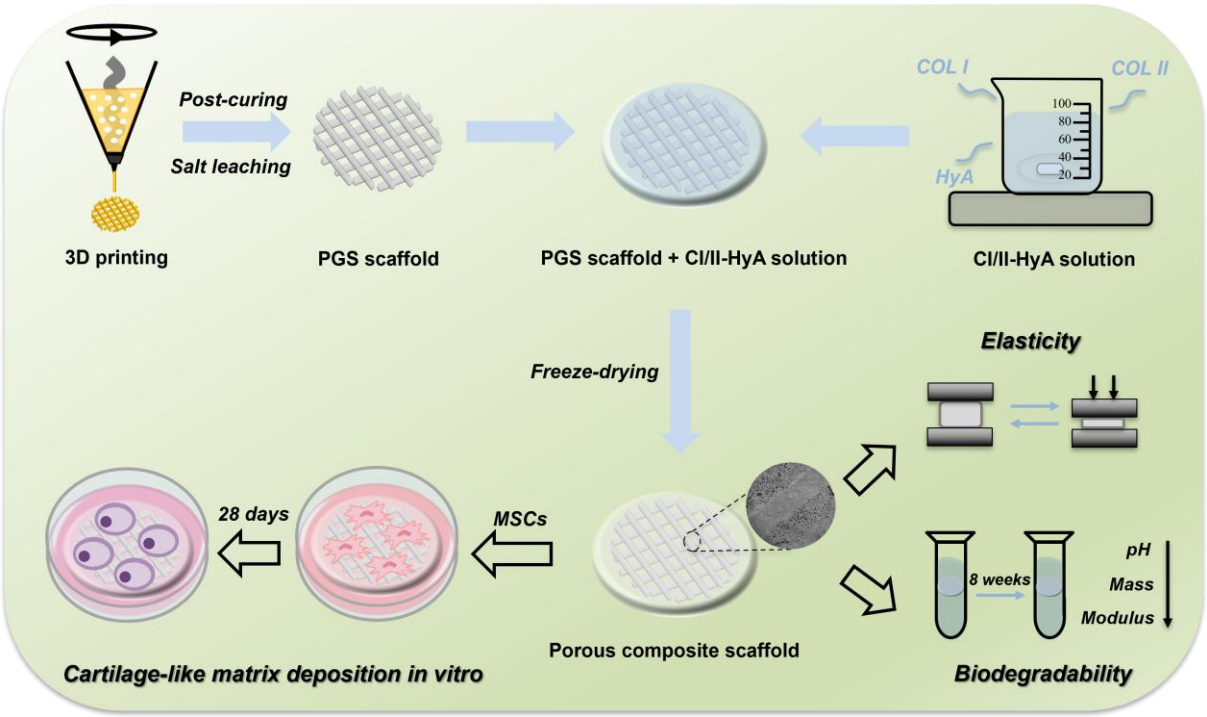

Figure 4.1: The fabrication and application of CI/II-HyA@PGS composite scaffold manufactured from a 3D-printed PGS framework and a collagen type I/II-hyaluronic acid (CI/II-HyA) matrix.

After the manufacturing of the samples, FT-IR spectroscopy was used to identify the curing reaction. As shown in Figure 4.2a, in the PGS prepolymer, the absence of the characteristic absorption at 1230 cm^{-1} related to -C-O- in the carboxyl group from sebacic acid, and the weakness of absorption at 3291 cm^{-1} corresponding to the -OH group in glycerol both demonstrate the consumption of monomers during the reaction. Furthermore, the characteristic absorption of -CH_2- in glycerol (2869 cm^{-1} and 2932 cm^{-1}) and -C=O- in sebacic acid (1686 cm^{-1}) both appear in the final PGS scaffold [183], indicating successful curing.

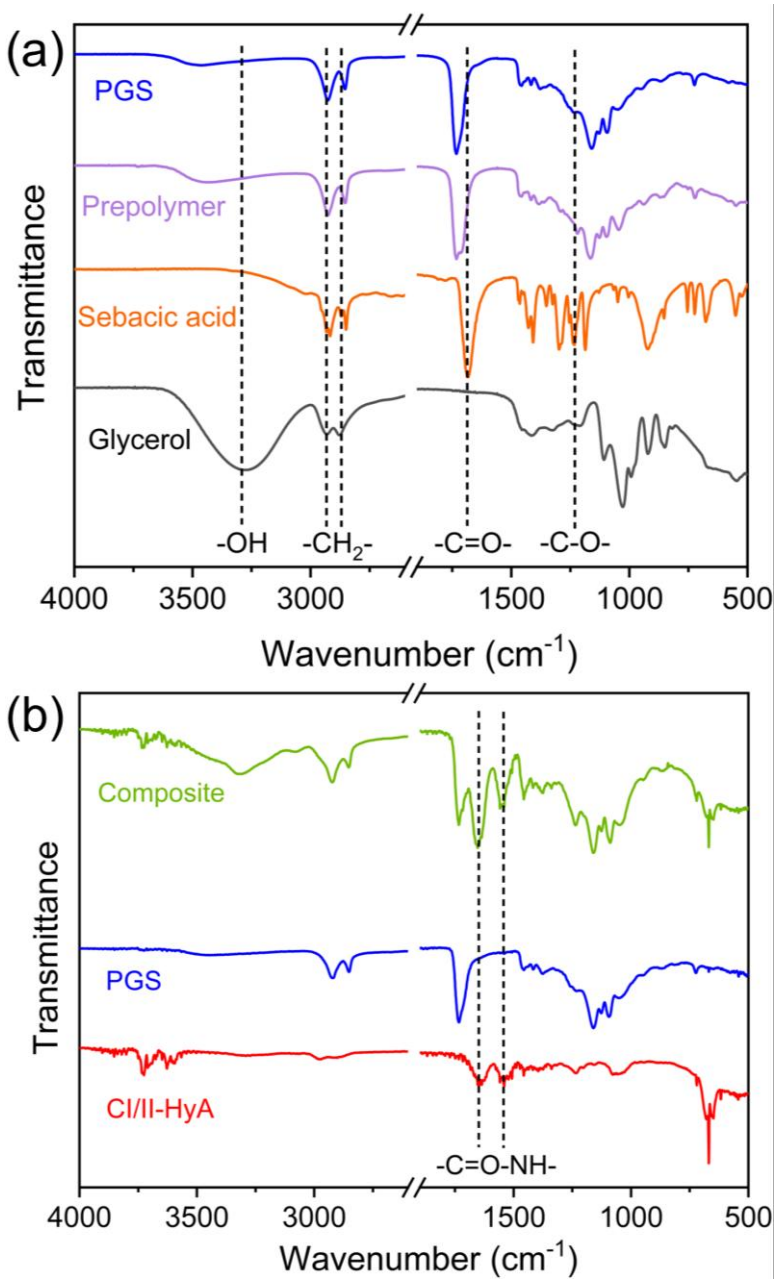

Figure 4.2: FT-IR spectrum of (a) glycerol, sebacic acid, PGS prepolymer and PGS, and (b) CI/II-HyA, PGS and CI/II-HyA@PGS scaffolds.

After incorporation with CI/II-HyA matrix, it can be observed from the FT-IR spectrum in Figure 4.2b that two specific absorption peaks at 1648 cm^{-1} and 1542 cm^{-1} related to the amide I band and amide II bond in collagen occur in CI/II-HyA@PGS compared with the PGS, indicating the successful incorporation of the matrix and framework.

The development of highly porous scaffolds is crucial in cartilage tissue engineering to ensure an appropriate nutrient-waste exchange for cell populations

colonized on biomaterials, ultimately biologically satisfying their function in a long-term culture environment [195]. In this work, the CI/II-HyA@PGS scaffold was successfully manufactured with a hierarchical porosity between the porous collagen type I/II-hyaluronic acid matrix and the PGS filaments, which demonstrated both good integration and spatial structure, as shown in Figure 4.3.

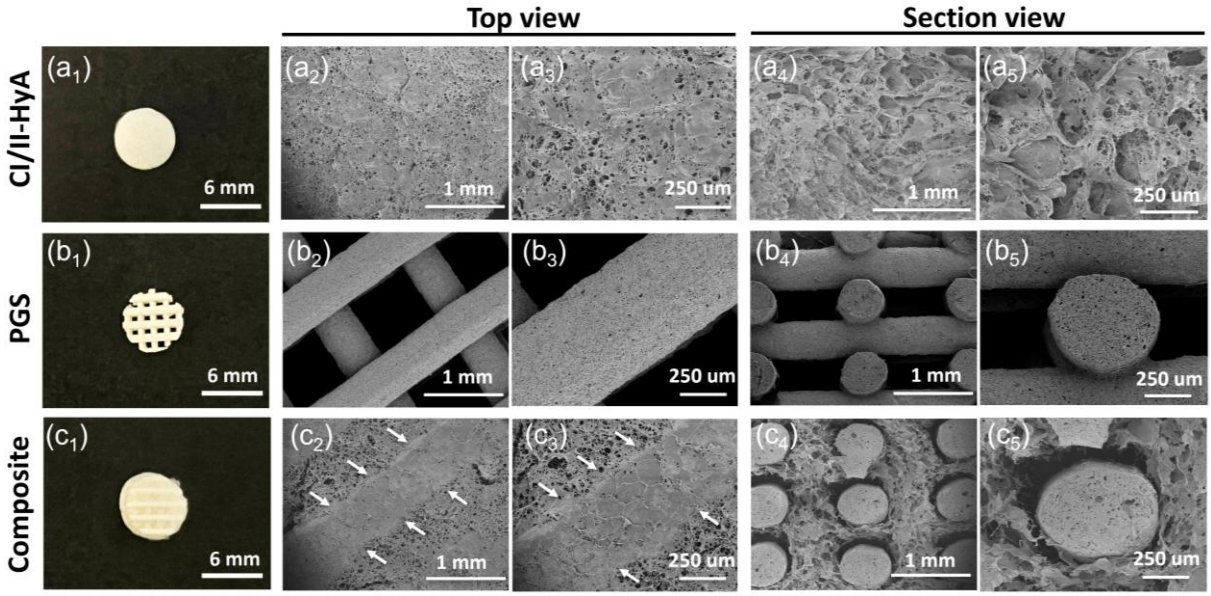

Figure 4.3: Representative digital images and SEM images of (a) CI/II-HyA, (b) PGS, (c) composite scaffolds under the top view and section view. Scale bar represents 6 mm and 1 mm and 250 µm length, respectively.

CI/II-HyA scaffold exhibits a fluffy porous structure with a pore size of 155 ± 5 µm and a porosity of 99 % formed through the multiple freeze-drying procedure [110]. 3D-printed PGS scaffold presents an interconnected multi-layer structure, in which the filaments exhibit a homogeneous cylindrical shape with an average diameter of 550 ± 23 µm, and the average gap size between the filaments is 778 ± 34 µm. High microporosity caused by NaCl leaching appears on the surface and inside of PGS filaments, making the overall PGS scaffold show a hierarchical porosity. Additionally, it can be seen in the CI/II-HyA@PGS scaffold that the porous collagen matrix is firmly coated on the surface of the porous PGS filaments and fill the printed pores of the PGS scaffold. After incorporation, PGS framework maintained a good spatial structure without filaments deformation and collapse, and the internal microporous structure was also maintained. These results

indicate that the fabrication of the biomimetic CI/II-HyA@PGS scaffold with hierarchical porosity was successfully achieved.

4.3. Mechanical properties

The mechanical properties of CI/II-HyA, PGS and CI/II-HyA@PGS composite scaffolds were tested through compression and cyclic compression tests under air (dry) and PBS solution (wet) conditions. As shown in Figure 4.4, the incorporation of CI/II-HyA matrix significantly enhanced the mechanical properties of the PGS framework in dry conditions. The compressive modulus of the CI/II-HyA@PGS composite scaffold was 167.0 kPa, which is twice that of the PGS scaffold with a modulus of 80.0 kPa, while the modulus of the CI/II-HyA scaffold was 10.8 kPa. Notably, after incorporating the CI/II-HyA matrix, the compressive modulus of the CI/II-HyA@PGS composite scaffold in dry conditions was greatly improved due to hydrogen bond interactions in the collagen molecular chain, reaching 167.0 kPa, as shown in Table 4.1, which is within the modulus range of native cartilage (100-2000 kPa) [196]. While in wet solution, the compressive modulus of the CI/II-HyA@PGS composite scaffold was reduced to 45.2 kPa, which was close to that of the PGS scaffold (35.7 kPa), as shown in Table 4.1. It demonstrated that although the incorporation of a collagen-based matrix improved the mechanical properties, the PGS scaffold is still the main provider of mechanical support in the CI/II-HyA@PGS composite scaffold.

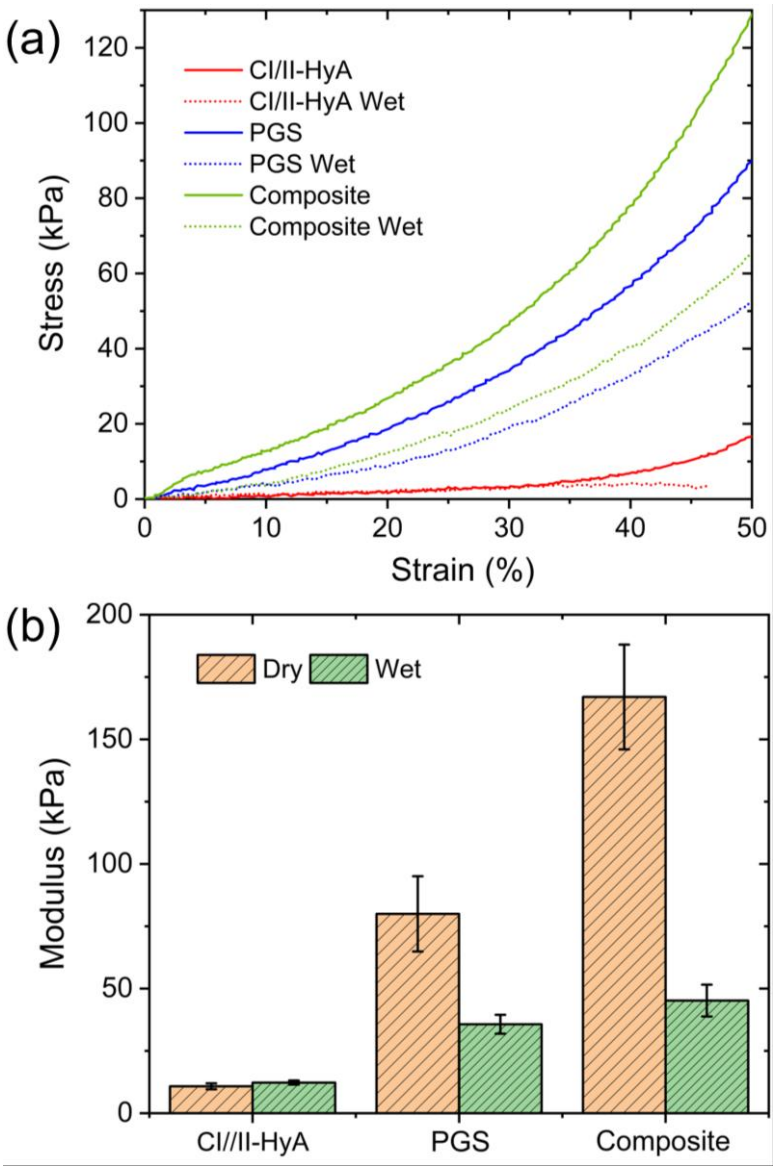

Figure 4.4: (a) Stress-strain curves under compression at a speed of 0.1 mm/s and (b) the recorded compressive modulus of CI/II-HyA, PGS, and CI/II-HyA@PGS composite scaffolds under air (dry) and PBS solution (wet) conditions.

Table 4.1: The compressive parameters of CI/II-HyA, PGS and CI/II-HyA@PGS scaffolds in dry and wet conditions

Sample	Compressive modulus (kPa)	Compressive stress (kPa)
CI/II-HyA	10.8 ± 1.2	12.6 ± 0.1
CI/II-HyA Wet	12.3 ± 0.8	5.7 ± 0.5
PGS	80.0 ± 15.1	104.4 ± 15.8
PGS Wet	35.7 ± 3.8	60.4 ± 7.0
Composite	167.0 ± 21.0	121.4 ± 8.4
Composite Wet	45.2 ± 6.4	56.7 ± 7.4

Furthermore, various studies [197,198] have shown that during daily physiological activities, the amount of cartilage deformation caused by force is about 10%-20% of its height, depending on the distribution. When articular cartilage undergoes vigorous exercise, its deformation range can be as high as 40%, especially in joint tissues [199,200]. Consequently, developing scaffolds capable of processing adapted elasticity is another important aspect to consider guaranteeing mechanical features that recapitulate cartilage healthy physiological conditions. Therefore, cyclic compression tests under dynamic strains of 10%, 20%, and 40% were conducted to evaluate the elasticity and fatigue resistance of PGS and CI/II-HyA@PGS composite scaffolds under dry and wet conditions.

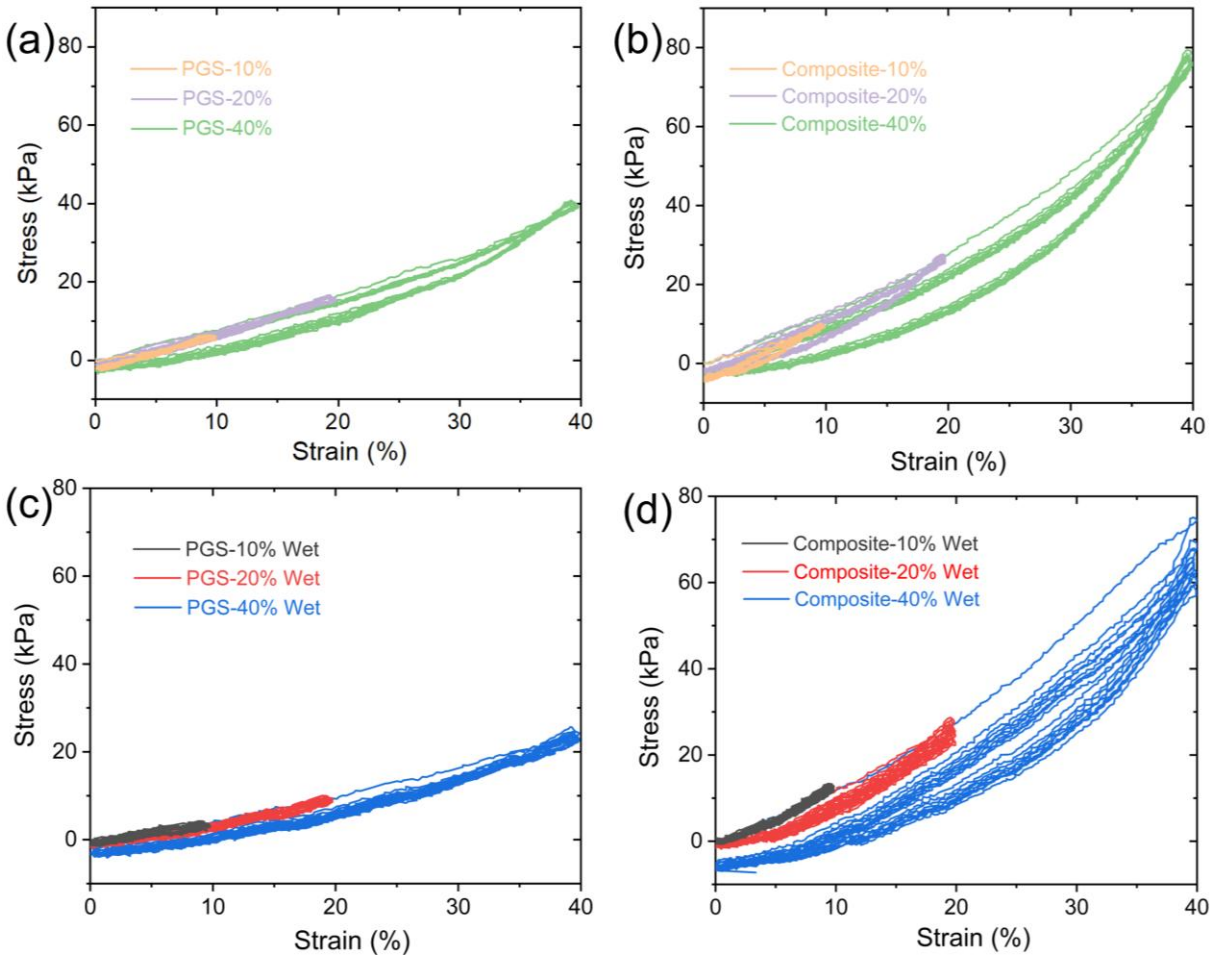

Figure 4.5: Cyclic compression tests with strains of 10%, 20%, and 40% at a speed of 0.1 mm/s (a) PGS scaffold in dry condition, (b) PGS scaffold in wet condition, (c) CI/II-HyA@PGS composite scaffold in dry condition, and (d) CI/II-HyA@PGS composite scaffold in wet condition.

As shown in Figure 4.5, both scaffolds show a complete elastic recovery at low strains of 10% and 20%, while some hysteresis was observed at a high strain of 40%. Among them, the CI/II-HyA@PGS scaffold shows more severe hysteresis under high strains in wet conditions. Overall, the novel CI/II-HyA@PGS composite scaffold exhibited adapted elasticity and excellent fatigue resistance under dynamic compression conditions, suitable for use in the cartilage environment under frequent deformation.

4.4. Degradation behaviour

Another important characteristic of successful cartilage-engineered scaffolds is to possess a degradation rate that matches the regeneration rate of native tissues. Therefore, the degradation behaviour of CI/II-HyA, PGS, and CI/II-HyA@PGS composite scaffolds was measured *in vitro* at 37 °C in PBS solution for 8 weeks. During the degradation, all scaffolds showed shape integrity without any damage (Figure 4.6) and mass retention of 48.52%, 92.51%, and 94.51% after 8 weeks, for CI/II-HyA, PGS and CI/II-HyA@PGS composite scaffolds, respectively, as shown in Figure 4.7a.

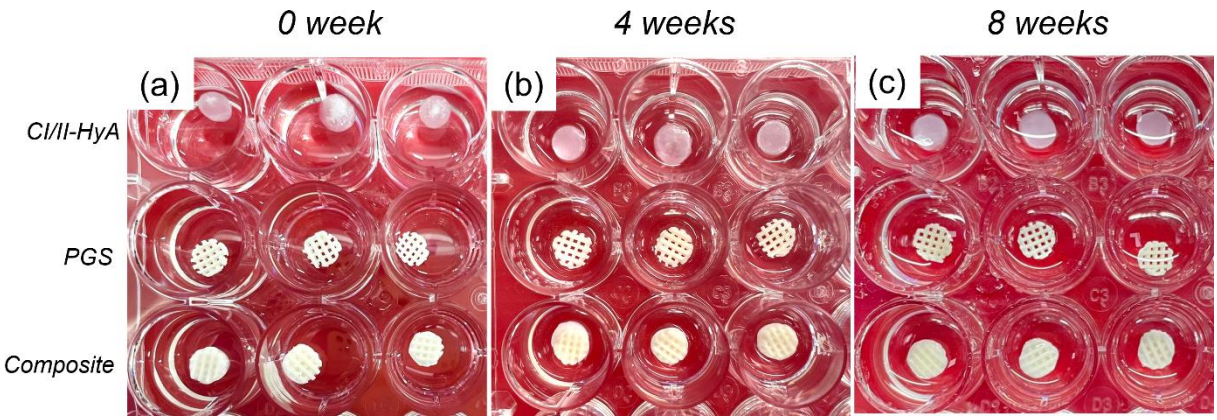

Figure 4.6: Digital images of CI/II-HyA, PGS and CI/II-HyA@PGS composite scaffolds after degradation. (a) 0 week, (b) 4 weeks and (c) 8 weeks.

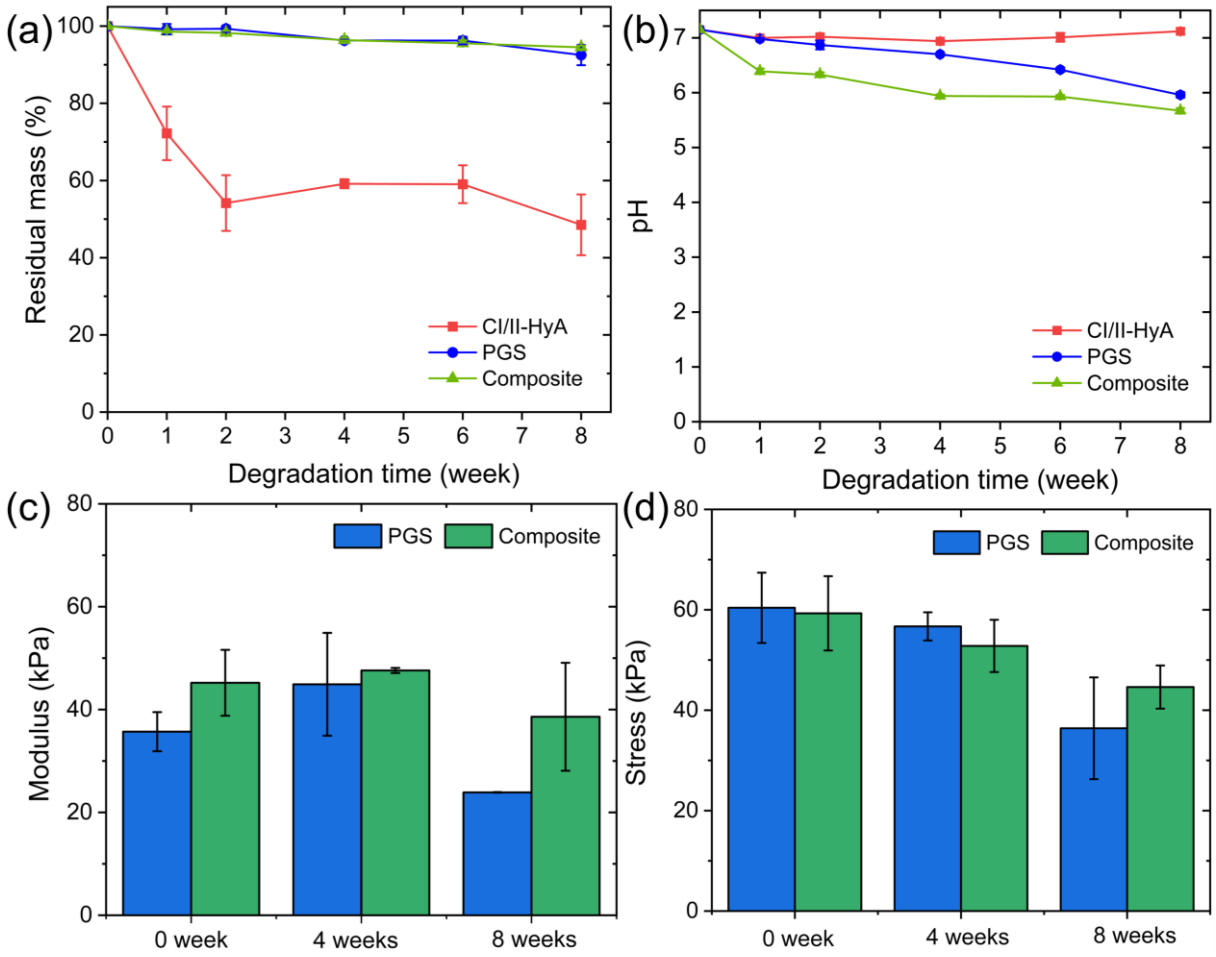

Figure 4.7: *In vitro* degradation behaviour with time on (a) residual mass, (b) pH change, (c) compressive modulus, and (d) compressive stress of CI/II-HyA, PGS, and CI/II-HyA@PGS composite scaffolds.

These results indicate that PGS and CI/II-HyA@PGS composite scaffolds maintained structural, mass, and mechanical integrity within 4 weeks, which matches the speed of MSC chondrogenesis and cartilage-like formation *in vitro*, but CI/II-HyA scaffold showed a rapid decrease in the same period. This is because the PGS framework not only provides mechanical support but also helps to protect against the loss of the collagen-based matrix. Meanwhile, in the CI/II-HyA@PGS composite scaffold, the PGS filaments were firmly surrounded by a collagen-based matrix, limiting the degradation of the PGS framework, which can be proved by the slower liner degradation tendency caused by surface erosion of the CI/II-HyA@PGS composite scaffold than PGS only. It solves the problem of the fast degradation rate of PGS to a certain extent, making it more matched with cartilage

regeneration [201]. Additionally, the tendency of pH and mass kept dropping gradually with time as shown in Figure 4.7b, meeting the requirements of the biodegradable scaffolds in tissue engineering.

More importantly, compression and cyclic compression were conducted in wet condition along the degradation to check the mechanical stability of PGS and CI/II-HyA@PGS composite scaffolds. As shown in Figure 4.7c and d, mechanical properties of both scaffolds showed decreasing during degradation. Notably, the compressive modulus of PGS and composite scaffolds remained unchanged after 4 weeks of degradation while gradually decreasing after 8 weeks, but the compressive stress decreased significantly with time (Table 4.2 and Table 4.3).

Table 4.2: The compressive parameters of PGS scaffold after degradation in wet conditions

Sample	Compressive modulus (kPa)	Compressive stress (kPa)
PGS Wet 0 week	35.7 ± 3.8	60.4 ± 7.0
PGS Wet 4 weeks	39.0 ± 4.3	56.7 ± 2.8
PGS Wet 8 weeks	29.8 ± 13.2	36.4 ± 10.1

Table 4.3: The compressive parameters of CI/II-HyA@PGS composite scaffold after degradation in wet conditions

Sample	Compressive modulus (kPa)	Compressive stress (kPa)
Composite Wet 0 week	45.2 ± 6.4	56.7 ± 7.4
Composite Wet 4 weeks	47.6 ± 0.5	52.8 ± 5.2
Composite Wet 8 weeks	38.6 ± 10.5	44.6 ± 4.3

Besides, cyclic compression tests show that the elasticity and fatigue resistance of both scaffolds were well reflected without any destruction during the 8 weeks of degradation (Figure 4.8). Overall, the combination of CI/II-HyA matrix and PGS framework shows a syncretic effect on the degradation control, endowing the CI/II-HyA@PGS composite scaffold with a perfect degradation rate matched cartilage tissue regeneration.

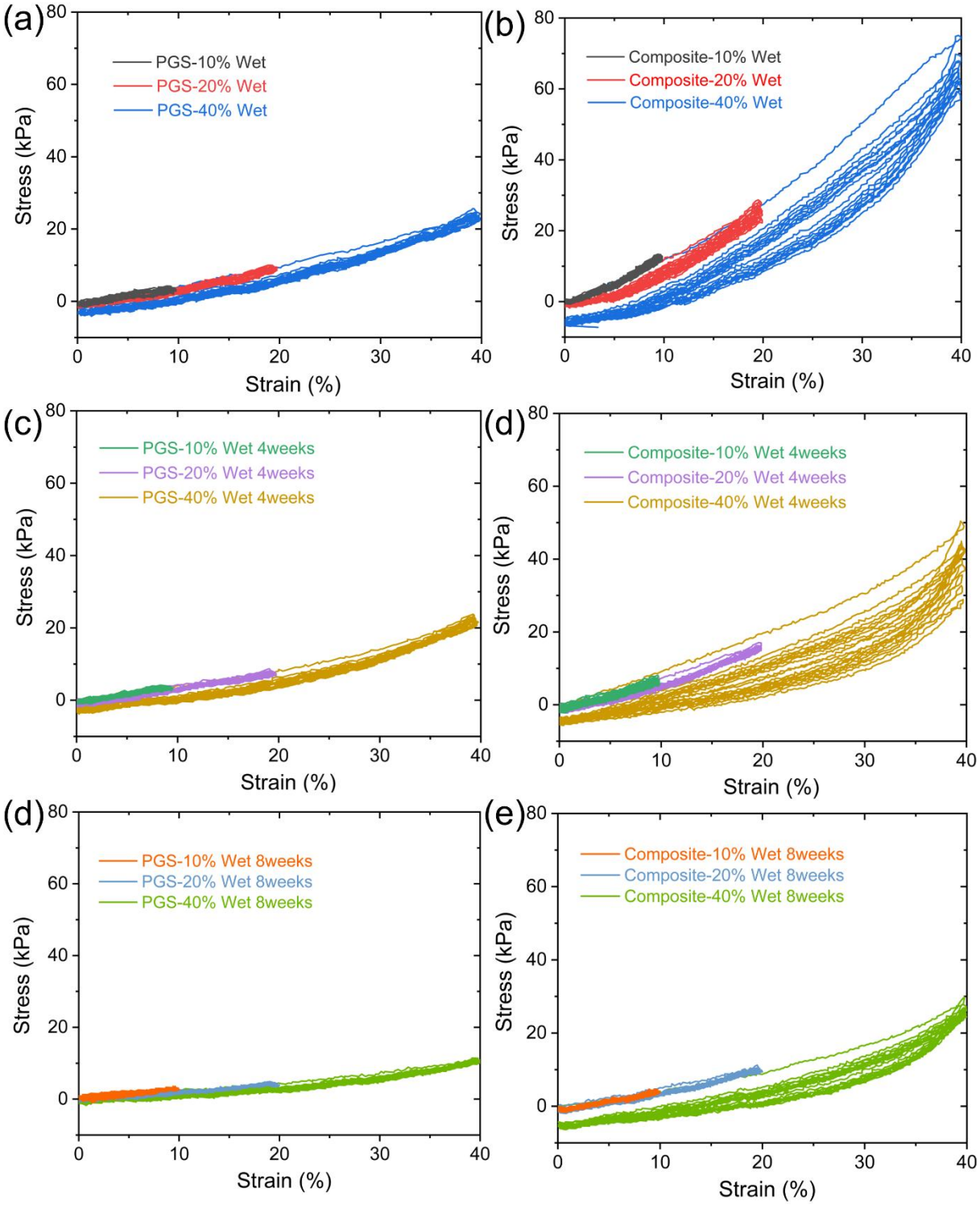

Figure 4.8: Cyclic compression tests in PBS solution with stain of 10%, 20% and 40%. (a) PGS scaffold, (b) CI/II-HyA@PGS composite scaffold, (c) PGS scaffold after 4 weeks of degradation, (d) CI/II-HyA@PGS composite scaffold after 4 weeks of degradation, (e) PGS scaffold after 8 weeks of degradation and (f) CI/II-HyA@PGS composite scaffold after 8 weeks of degradation.

4.5. Biological performance

4.5.1. Biocompatibility

The capability of CI/II-HyA, PGS and CI/II-HyA@PGS scaffolds to support cell cellular viability and growth was evaluated to assess biocompatibility. As shown in Figure 4.9, all scaffolds resulted in equal cellular metabolic activity at day 28, though PGS and composite scaffolds showed significantly increased cellular metabolic activity at days 7 and 15, compared to the CI/II-HyA scaffold ($p \leq 0.0001$), indicating the combination with PGS scaffold has no cytotoxic effect on the biocompatibility.

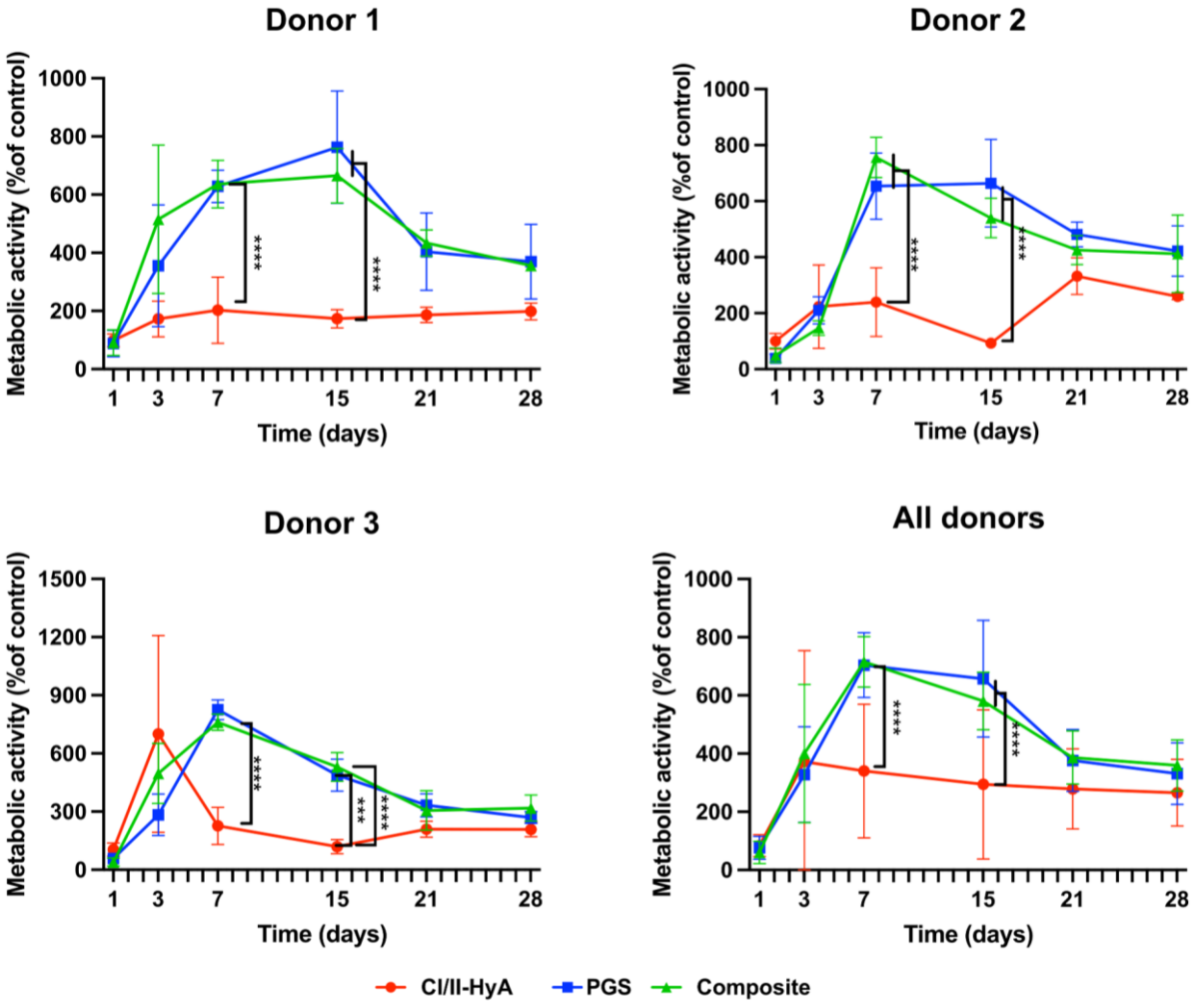

Figure 4.9: Cellular metabolic activity (normalized to CI/II-HyA scaffold at day 1) after 1, 3, 7, 15, 21 and 28 days. Data shown represent the mean from three individual rat MSC donors $n \geq 3$ (unless indicated differently).

Despite similar metabolic activity was observed between groups at day 28, the CI/II-HyA@PGS composite scaffold possessed the highest overall DNA content level of 3.93 µg, compared to CI/II-HyA of 2.07 µg ($p \leq 0.001$) and PGS of 1.03 µg ($p \leq 0.0001$) (Figure 4.10). This is because in addition to the major mechanical reinforcement provided by the 3D-printed PGS filaments, the PGS framework also supported the porous pro-chondrogenic collagen matrix, thus benefiting the overall construct to obtain an increased cellular proliferation.

Furthermore, the DNA levels of the CI/II-HyA@PGS composite scaffold were significantly increased compared to the PGS scaffold of donors 1 and 2. Although CI/II-HyA scaffold had lower DNA levels than CI/II-HyA@PGS composite scaffold, they still resulted in a significant increase in overall DNA level, compared to PGS scaffold ($p \leq 0.05$), due to the smaller pores ensure better cell attachment. These findings are comparable with studies related to cartilage-engineered scaffolds that incorporated bioactive matrices such as alginate/agarose/collagen or hyaluronic acid into 3D-printed frameworks such as PCL and PLA [186,202,203]. Overall, the CI/II-HyA@PGS composite shows improved biocompatibility by proving greater surface area available to the cells via the combination of CI/II-HyA matrix and 3D-printed PGS framework.

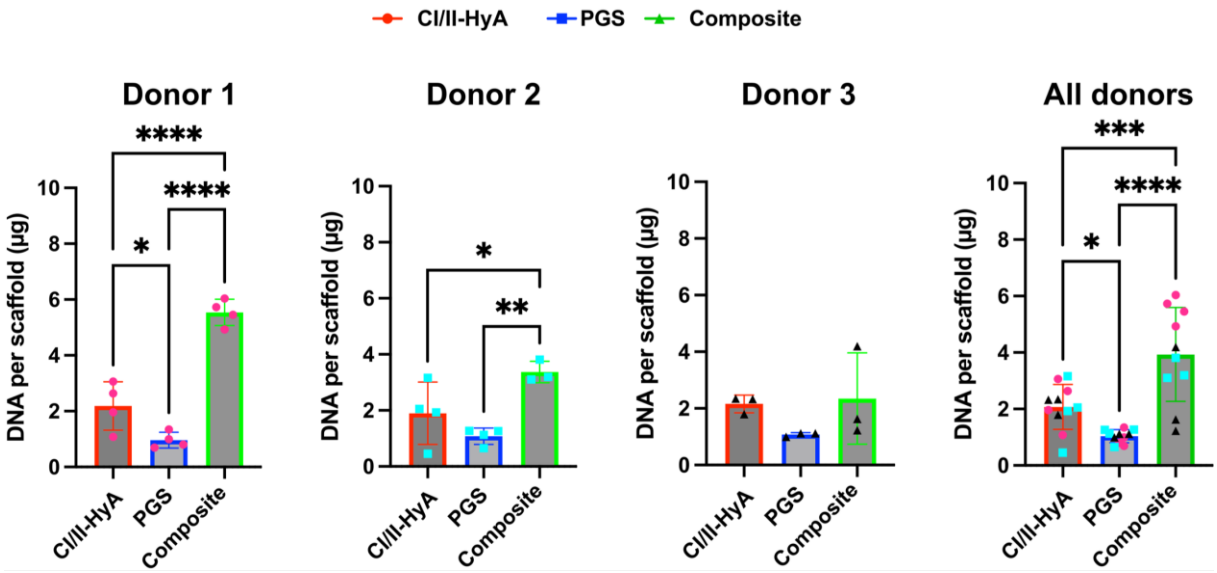

Figure 4.10: DNA content per scaffold after 28 days in culture of CI/II-HyA, PGS and CI/II-HyA@PGS composite scaffolds. Data shown represent the mean from three individual rat MSC donors $n \geq 3$ (unless indicated differently).

4.5.2. Chondrogenesis

To assess the capability of the scaffolds to sustain effective MSC chondrogenic differentiation, the expression of key genetic markers typically associated with accurate chondrogenesis was investigated. All scaffold variants sustained overall gene expression of Collagen I (*COL1A1*), Collagen 2 (*COL2A1*) and Aggrecan (*ACAN*) of MSC at day 28, thus indicating the ability of these scaffolds to support effective MSC chondrogenic differentiation (Figure 4.11).

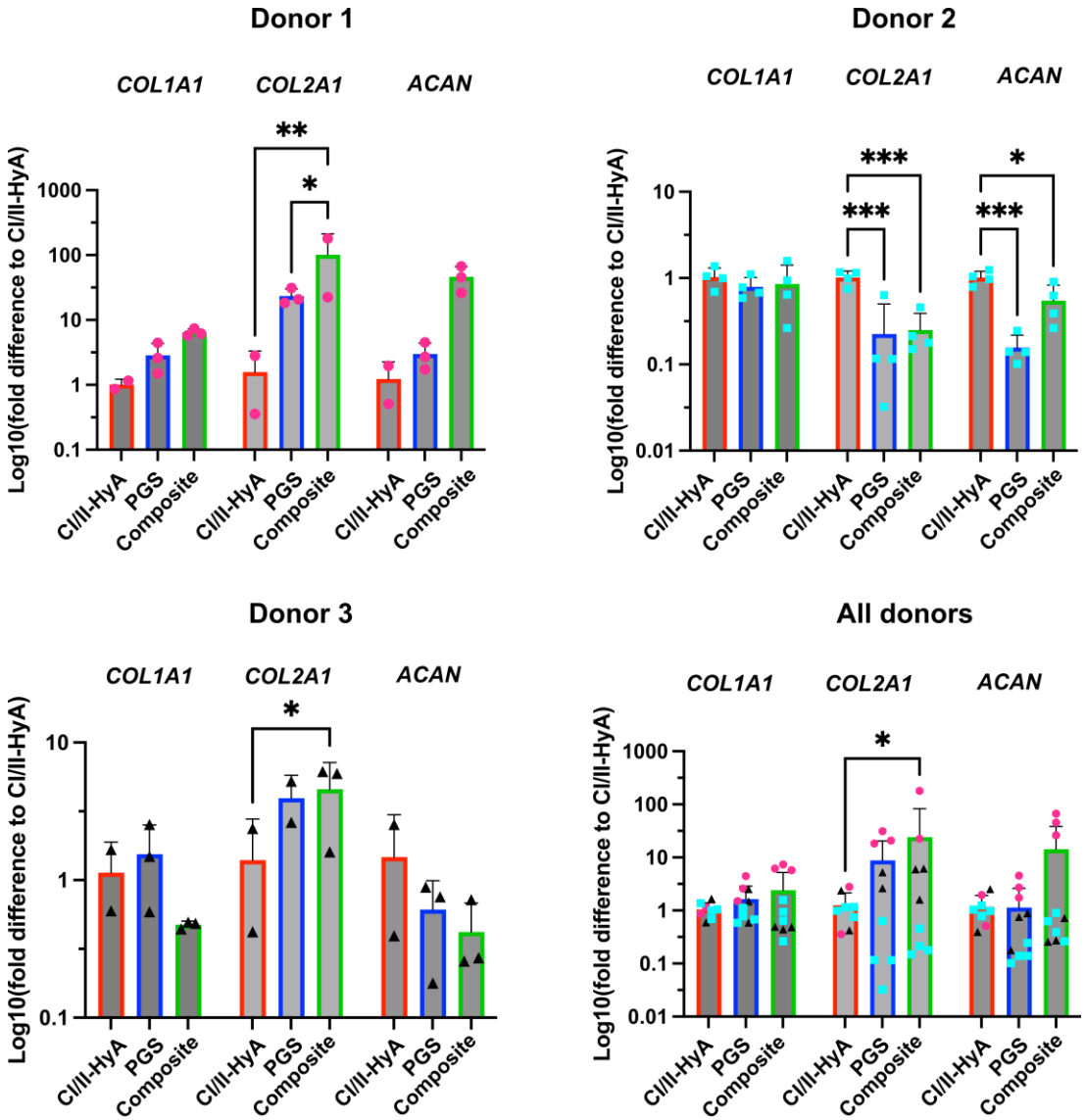

Figure 4.11: Expression of chondrogenic genes *COL1A1*, *ACAN*, and *COL2A1* of MSC on CI/II-HyA, PGS and CI/II-HyA@PGS composite scaffolds after 28 days in culture. Data shown represent the mean from three individual rat MSC donors n ≥ 3 (unless indicated differently).

Interestingly, the CI/II-HyA@PGS composite scaffold displayed significantly higher *COL2A1* compared to CI/II-HyA scaffold ($p \leq 0.05$), demonstrating potential for the CI/II-HyA@PGS composite scaffold to enhance chondrogenesis. Specifically, *COL2A1* gene expression was significantly upregulated in CI/II-HyA@PGS composite scaffold compared to CI/II-HyA scaffold in two individual donors, respectively, donors 1 ($p \leq 0.01$) and 3 ($p \leq 0.05$). Moreover, although it was not significant when compared to the other groups, the CI/II-HyA@PGS composite scaffold also displayed the highest *ACAN* expression at day 28. This is because, in the CI/II-HyA@PGS composite scaffold, the porous collagen-based matrix ensured adequate cell attachment, migration, and differentiation, the 3D-printed PGS framework reduced risks of cell-mediated contraction, thereby ensuring a greater surface area available to the cells. Consequently, it has translated into enhanced MSC migration, proliferation, and matrix deposition in CI/II-HyA@PGS composite scaffold. This also can be confirmed by cartilage-like matrix formation *in vitro* which studied by sGAG deposition and histology assessment.

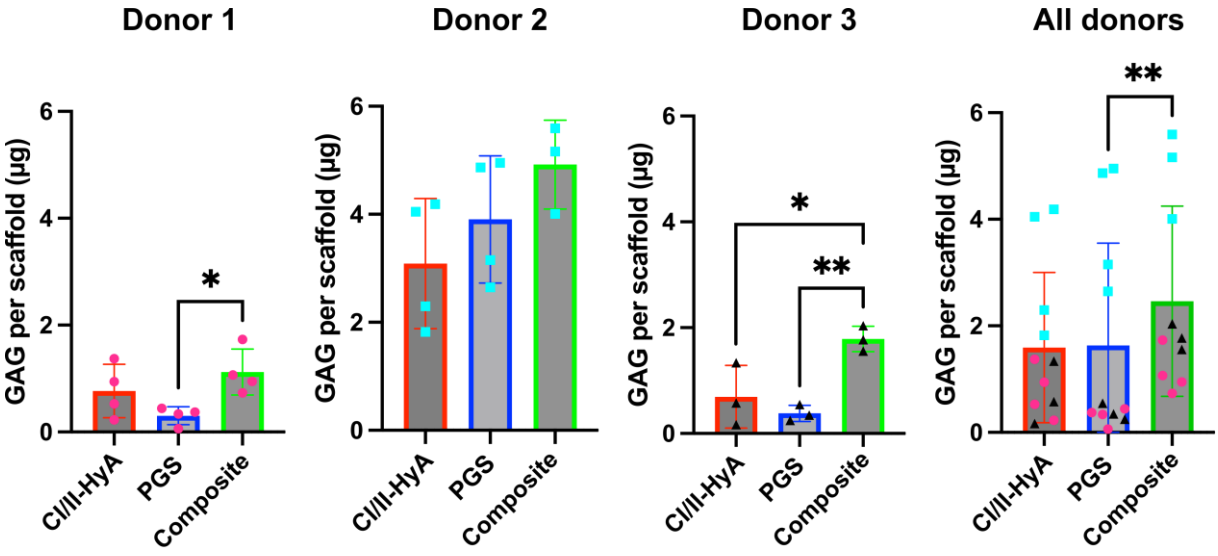

Figure 4.12: Overall sGAG content on CI/II-HyA, PGS and CI/II-HyA@PGS composite scaffolds after 28 days in culture. Data shown represent the mean from three individual rat MSC donors $n \geq 3$ (unless indicated differently).

As shown in Figure 4.12, all scaffold variants sustained sGAG deposition by MSCs at day 28. The CI/II-HyA@PGS composite scaffold displayed the highest

overall levels of sGAG per scaffold (2.70 µg/mL), which was significantly higher compared to PGS scaffold with a level of 1.63 µg/mL ($p \leq 0.01$). Specifically, it also supported significantly increased sGAG quantities compared to PGS scaffold with donors 1 ($p \leq 0.05$) and 3 ($p \leq 0.01$), as well as CI/II-HyA scaffold with donor 3 ($p \leq 0.05$).

Furthermore, histological analysis performed and analysed to qualitatively assess the ability of these scaffolds to sustain effective MSC migration and cartilage-like matrix distribution in theses scaffolds. Histological analysis confirmed sGAG presence in all scaffold groups at day 28 (Figure 4.13). CI/II-HyA and CI/II-HyA@PGS composite scaffolds displayed more abundant and homogenous sGAG distribution compared to PGS scaffold. In parallel, a more homogenous cellular infiltration and migration throughout the matrices was also observed in CI/II-HyA and CI/II-HyA@PGS composite scaffolds. Overall, these findings demonstrate that CI/II-HyA@PGS composite scaffold is an excellent biomimetic scaffold with a strong possibility to succeed *in vivo* in enhancing cartilage defect repair.

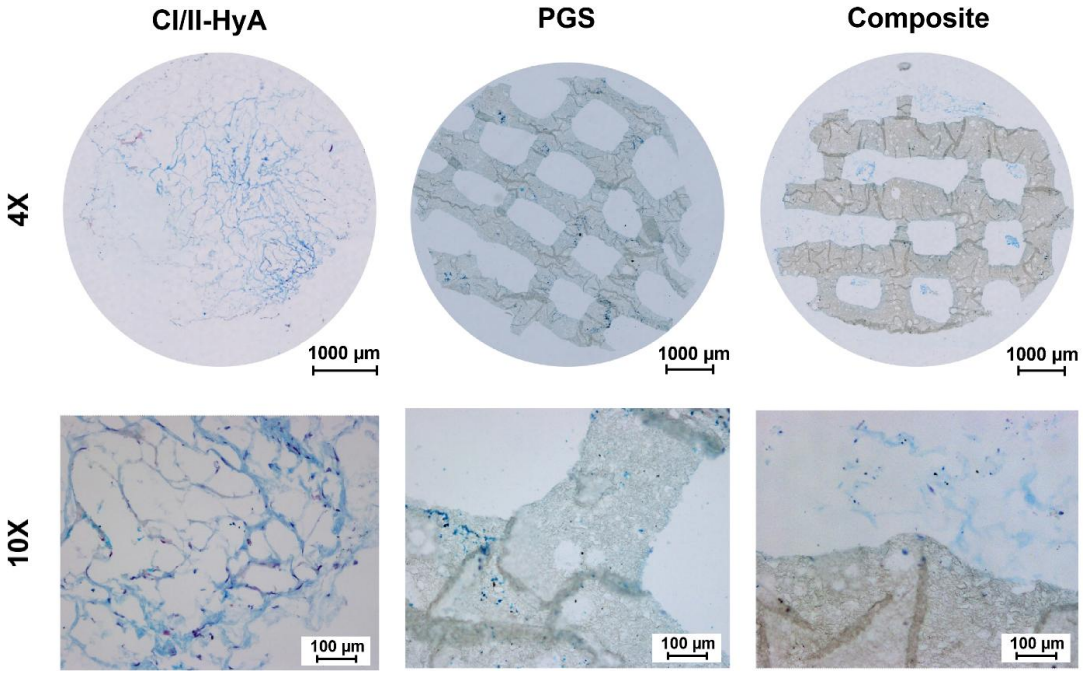

Figure 4.13: Representative histological images of MSC-seeded scaffolds stained with alcian blue after 28 days in culture. The histological images were collected for scaffolds seeded with rat MSCs from donors 1, 2 and 3. Scale bar represents 1000 µm and 100 µm length for the 4X and 10X magnification, respectively.

4.6. Conclusions

In this Chapter, a novel biomimetic collagen-based 3D-printed PGS composite scaffold (CI/II-HyA@PGS) was specifically designed to enhance cartilage defect repair, whereby the porous CI/II-HyA matrix served as the biological cue for MSC chondrogenic stimulation and the PGS scaffold as the mechanical enforcement to support tissue growth. The CI/II-HyA@PGS composite scaffold exhibited mechanical properties mimicking native cartilage, promoting accurate MSC differentiation and abundant cartilage-like matrix deposition at 28 days *in vitro*, while maintaining structural, mass, and mechanical stability during the initial cartilage regeneration period of 4 weeks. Taken together, this novel biomimetic CI/II-HyA@PGS composite scaffold with adaptive properties to native tissue holds great promise as an attractive clinical approach for enhanced cartilage defect repair.

5. Processing, structure and properties of CI-nHA@PCEC composite scaffold

5.1. Introduction

Large bone defects caused by trauma, disease, injury or infection are particularly challenging to heal, especially when they exceed the critical self-regeneration threshold (> 2.5 cm). In such cases, the implantation of substitutes becomes necessary, posing a significant clinical challenge [204][205][206][207]. Autografts and allografts are considered the most effective methods for treating bone defects, but their clinical application is severely limited by several drawbacks such as resource scarcity, immune rejection, and infection risks [102]. To address these challenges, tissue-engineered scaffolds composed of metals, ceramics, and polymers have emerged as promising alternatives [134][208]. Despite notable progress, many implants still fail to match the mechanical properties and degradation rates of native bone tissue, significantly limiting their effectiveness [209]. For instance, titanium and its alloys are widely used in clinical settings due to their high mechanical strength. But their non-degradable nature leads to a second surgery for implant removal after bone healing, which is associated with severe pain and infection risks. Additionally, stress concentration can result in implants loosening and fracture [210][211]. Therefore, there is an urgent need to develop biodegradable scaffolds with appropriate mechanical properties and degradation rate comparable to those of native tissue.

3D printing technology enables the precise and rapid fabrication of scaffolds that closely mimic native bone tissues at macro and micro architectures. In particular, it can achieve interconnected pore design, which is conducive to cell growth and vascularization during bone regeneration [131][212]. Biodegradable synthetic polymers have been extensively explored in bone tissue engineering [213]. Among them, polycaprolactone (PCL) has attracted substantial interest due to its biocompatibility, mild processing condition (melting point: 50-60 °C), and non-

inflammatory degradation products [41][145]. However, its hydrophobic nature results in a slow degradation rate of 2-3 years *in vivo*, severely limiting its clinical applications [214]. To overcome this limitation, a series of poly(ε-caprolactone)-poly(ethylene glycol)-poly(ε-caprolactone) (PCEC) copolymers using hydrophilic PEG with high molecular weights as macroinitiators were obtained in Chapter 3 [176]. Among them, $PCE_{20k}C$ shows excellent potential for bone tissue engineering. Its pronounced shear-thinning behaviour enhances its processability in extrusion-based 3D printing. More importantly, it exhibits a significantly lower water contact angle of (45.2°) compared with PCL (84.2°), leading to a faster degradation rate of 60% mass loss after 8 hours, compared to 70% mass loss after 23 days for PCL under accelerated degradation conditions. Nevertheless, similar to PCL, $PCE_{20k}C$ lacks bioactive sites, which limits osteogenesis, osteointegration, and osteoconductivity.

Recent research has shifted towards biomimetic composite scaffolds, which integrate bioactive matrices with native tissue-derived compounds into 3D-printed frameworks. This approach maintains mechanical properties while improving overall performance in aspects such as osteogenesis and osteoconductivity [215][104]. Hydroxyapatite (HA) and collagen type I (CI), the primary components of bone tissue, have been widely incorporated into bone tissue-engineered scaffolds. Their combination has demonstrated significant efficacy in promoting bone regeneration [216][217]. Especially, Gleeson et al. [218] have shown that addition of nano HA (nHA) particles to highly porous CI scaffolds accelerate healing, yielding results comparable to the current gold standard of autologous bone grafting. Therefore, CI-nHA scaffolds have been frequently used as a bone layer matrix, and they have been demonstrated excellent *in vitro* and *in vivo* performance in a variety of animal models, including rabbits and goats [193][192][219]. Despite these advances, the mechanical properties of CI-nHA scaffolds remain inferior to those of native cancellous bone, limiting their application to small defect repair.

This chapter aims to fabricate a biomimetic composite scaffold (CI-nHA@PCEC) consisting of a 3D-printed porous $PCE_{20k}C$ framework and a bioactive

CI-nHA matrix specifically designed for cancellous bone defect repair. The compressive properties of the scaffold will be evaluated both in dry and wet conditions. Degradation behaviour will be studied in phosphate-buffered saline (PBS) solution at 37 °C over eight weeks, examining changes in structure, mass, pH and mechanical properties. Finally, *in vitro* studies will be conducted to assess osteogenic and angiogenic potential using pre-osteoblast cells and endothelial cells.

5.2. Processing and structure

To create the CI-nHA@PCEC composite scaffold, a 3D-printed $PCE_{20k}C$ framework was first manufactured as the mechanical support, which was designed from a copolymer synthesized using PEG and ε-CL in Chapter 3. Then, a bioactive slurry (CI-nHA) composed of collagen type I and nano-hydroxyapatite, was prepared as biological cues. Finally, by soaking the $PCE_{20k}C$ scaffold in CI-nHA slurry, the biomimetic composite scaffold was obtained after a further freeze-drying process, as shown in Figure 5.1.

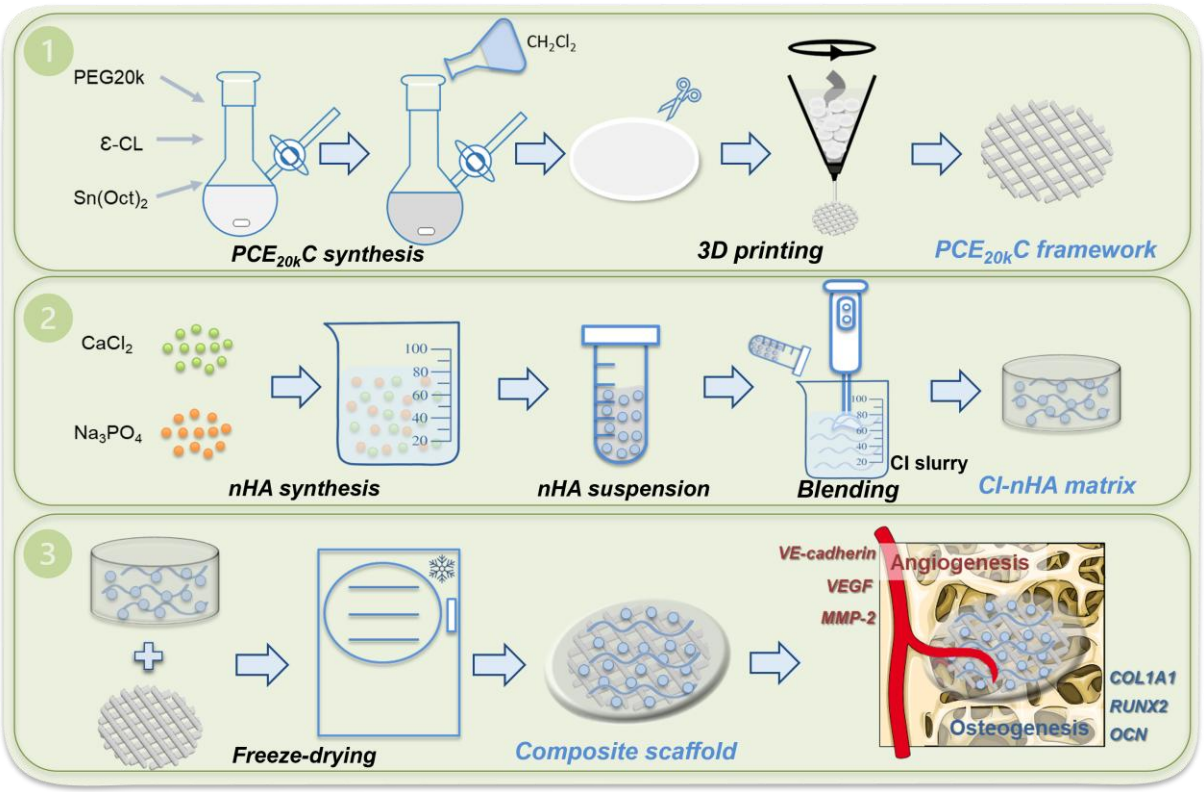

Figure 5.1: The fabrication process of CI-nHA@PCEC composite scaffold from $PCE_{20k}C$ framework and CI-nHA matrix.

The morphology of CI-nHA, $PCE_{20k}C$, and CI-nHA@PCEC composite scaffolds was first studied in terms of top and section views, as displayed in Figure 5.2. The CI-nHA matrix showed an even porous structure with a micropore size of around 100 µm [220]. In the 3D-printed $PCE_{20k}C$ framework, the printed filaments had smooth, regularly shaped cylindrical structures with a diameter of 550 µm. The interconnected macropores formed by 3D printing measured about 963 µm. After incorporation, the $PCE_{20k}C$ filaments were firmly surrounded by the CI-nHA matrix without any clamping or deformation.

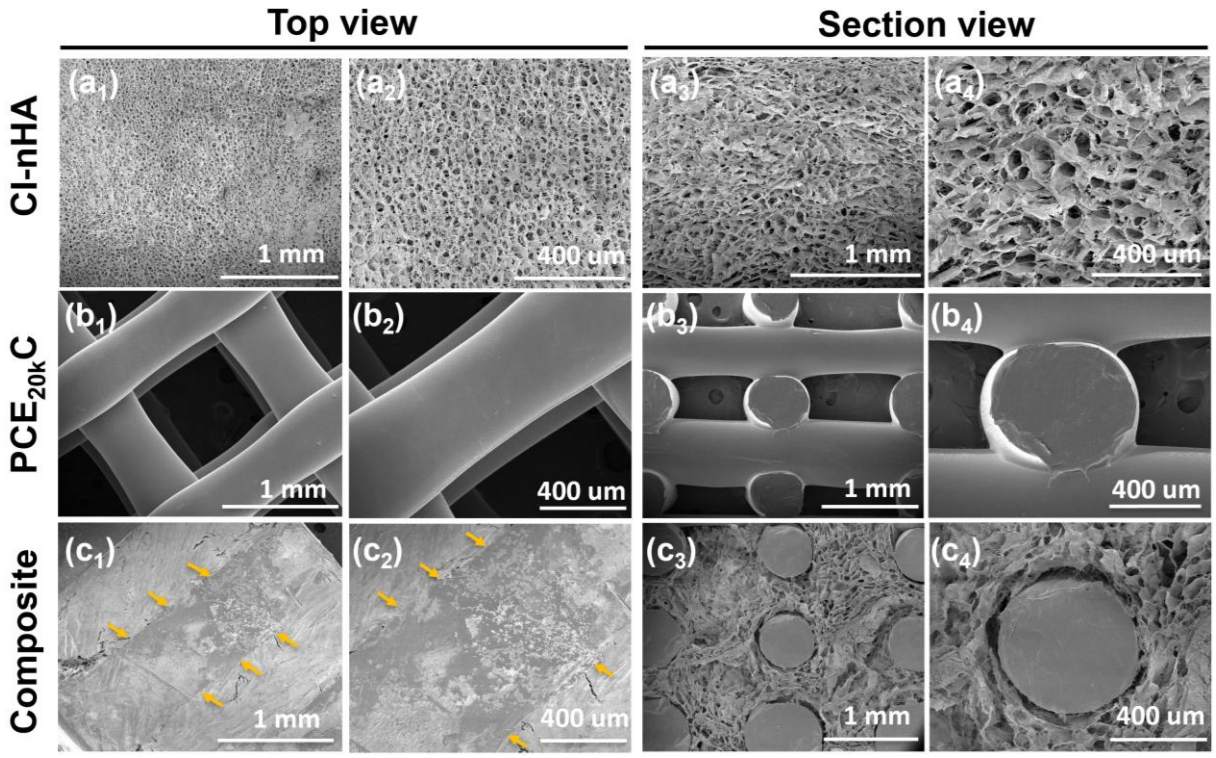

Figure 5.2: SEM images of (a) CI-nHA matrix, (b) $PCE_{20k}C$ framework and (c) CI-nHA@PCEC composite scaffold under top and section views.

Additionally, porosity plays a critical role in bone regeneration. It has been shown [104] that pore sizes between 300 - 1000 µm facilitate cell infiltration, proliferation, migration, and nutrient and waste transport. Among them, larger pore sizes can enhance vascularization and direct bone formation but reduce cell seeding efficiency. Therefore, a 3D-printed $PCE_{20k}C$ scaffold with macropores of 963 µm was used as a framework, filled with porous collagen matrix with micropores of ~ 100 µm facilitated cell adhesion. More importantly, the

microstructure of the CI-nHA matrix remained unchanged after integration, compared with previous study [189], confirming that the incorporation of $PCE_{20k}C$ framework did not alter its critical properties.

Furthermore, the calcium distribution in these scaffolds was then characterized by EDS, as shown in Figure 5.3. The EDS map of the CI-nHA@PCEC composite scaffold clearly shows a distinct dividing line, where calcium is evenly dispersed in the CI-nHA matrix, with almost no signal detected in the $PCE_{20k}C$ framework. These results confirm the successful fabrication of a biomimetic composite scaffold with hierarchical porosity and uniform calcium distribution.

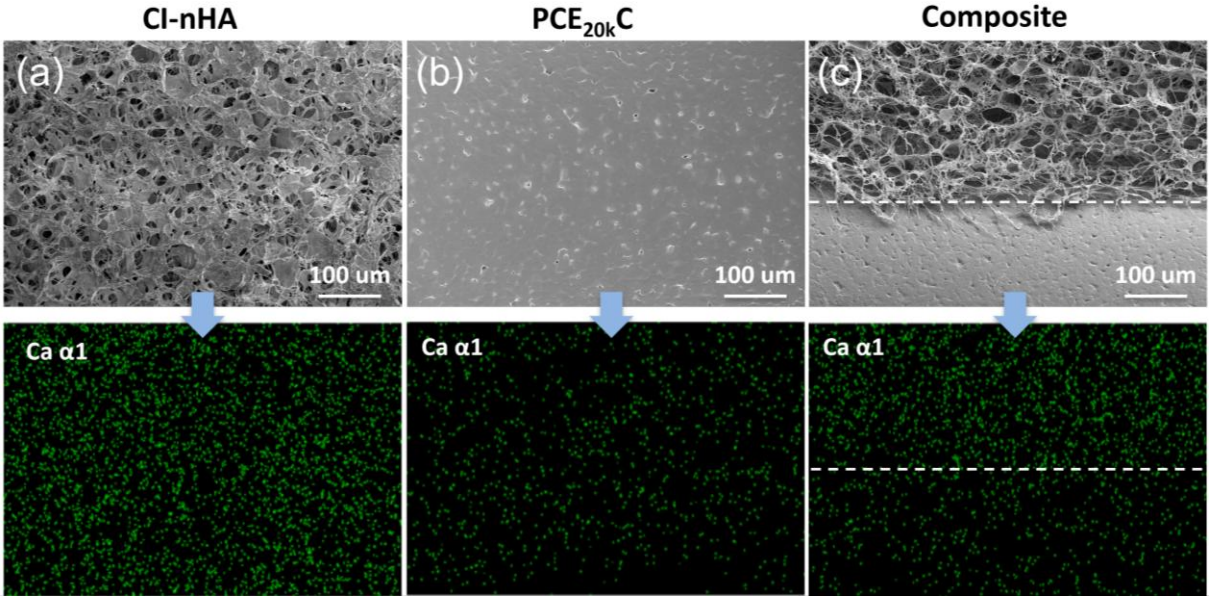

Figure 5.3: Scanning electron microscopic (SEM) images and energy dispersive X-ray spectroscopy (EDS) mapping of (a) CI-nHA, (b) $PCE_{20k}C$ and (c) CI-nHA@PCEC composite scaffolds.

5.3. Mechanical properties

The mechanical properties of CI-nHA, $PCE_{20k}C$ and CI-nHA@PCEC composite scaffolds were tested through compression tests under air (dry) and PBS solution (wet) conditions. Figure 5.4a shows the compression modulus of CI-nHA, $PCE_{20k}C$, and CI-nHA@PCEC composite scaffolds in air (dry) and PBS solution (wet). The modulus of CI-nHA scaffold is 26 kPa, which is much significantly lower ($p<0.0001$) than that of $PCE_{20k}C$ scaffold with 36.9 MPa in dry

condition. Therefore, the incorporation of CI-nHA matrix has no influence on the mechanical properties of the CI-nHA@PCEC composite scaffold with a modulus of 37.0 MPa and a stress of 8 MPa, which falls within the range of cancellous bone with a compressive modulus of 10 - 2000 MPa and stress of 2 - 12 MPa. Besides, although the modulus of CI-nHA decreases slightly in wet condition, the compression modulus of $PCE_{20k}C$ and CI-nHA@PCEC composite scaffolds are highly consistent with those in the dry condition, as shown in Table 5.1, which demonstrates the main mechanical enforcement in CI-nHA@PCEC composite scaffold comes from $PCE_{20k}C$ framework, and further confirms the mechanical stability in a wet environment, mimicking physiological conditions. These findings suggest that the CI-nHA@PCEC composite scaffold possesses suitable and stable mechanical properties for non-load bearing bone applications, such as subchondral bone.

Table 5.1: Compressive parameters of CI-nHA, $PCE_{20k}C$ and CI-nHA@PCEC composite scaffolds in dry and wet conditions

Sample	Compressive modulus (MPa)	Compressive stress (MPa)
CI-nHA	0.026 ± 0.004	0.020 ± 0.002
CI-nHA wet	0.017 ± 0.006	0.005 ± 0.001
$PCE_{20k}C$	36.9 ± 0.82	5.24 ± 0.28
$PCE_{20k}C$ wet	37.1 ± 2.12	7.04 ± 0.17
Composite	37.0 ± 5.50	7.75 ± 1.20
Composite wet	35.1 ± 8.10	6.49 ± 0.70

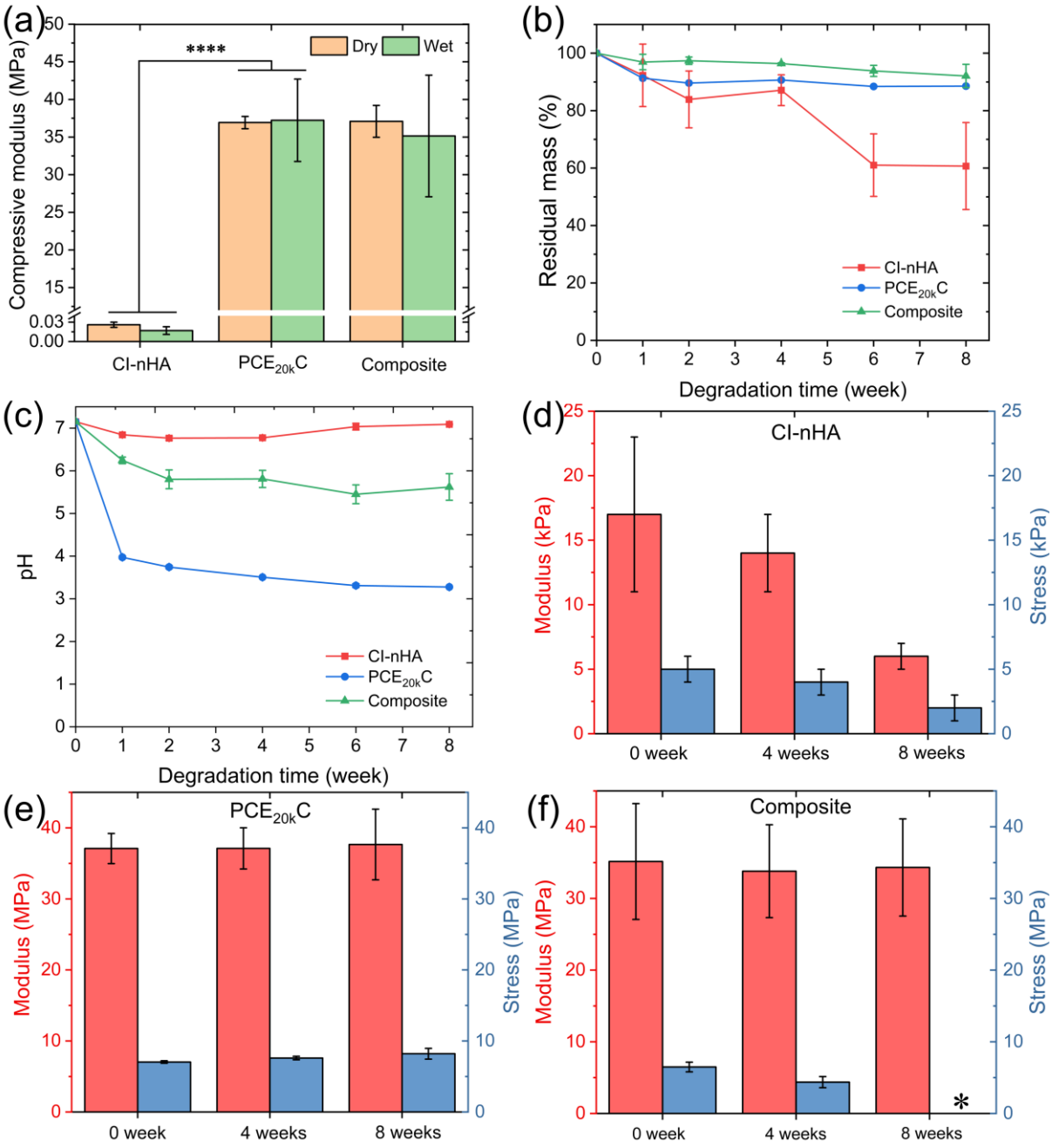

Figure 5.4: (a) compressive modulus in dry and wet conditions, (b) pH change and (c) residual mass of CI-nHA, $PCE_{20k}C$ and CI-nHA@PCEC composite scaffolds; compressive modulus and stress change of (d) CI-nHA, (e) $PCE_{20k}C$ and (f) CI-nHA@PCEC composite scaffolds after degradation for 0 week, 4 weeks and 8 weeks.

5.4. Degradation behaviour

The degradation behaviour of CI-nHA, $PCE_{20k}C$, and CI-nHA@PCEC composite scaffolds was studied by immersion in PBS solution at 37 °C for 8 weeks.

All scaffolds showed macrostructural stability during the degradation time of 8 weeks, as shown in Figure 5.5.

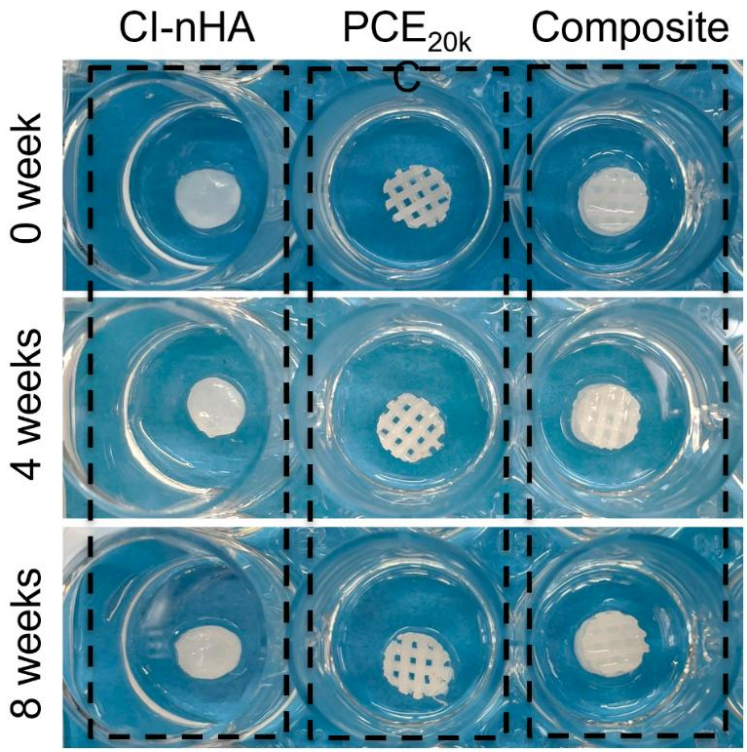

Figure 5.5: Digital images of CI-nHA, $PCE_{20k}C$ and CI-nHA@PCEC composite scaffolds after degradation for 0 week, 4 weeks and 8 weeks.

Figure 5.4b and c show the real-time record on residual mass and pH value of these scaffolds during degradation. It is clear to see that the mass of CI-nHA, $PCE_{20k}C$, and CI-nHA@PCEC composite scaffolds all gradually decreased over time, with residues of 60.7%, 88.5% and 92.1% after 8 weeks, respectively. Notably, the pH value of the $PCE_{20k}C$ scaffold dropped rapidly from 7.15 to 3.97 in the first week and continued to decrease gradually to 3.28 at 8 weeks, resulting in an acidic environment. This is because the degradation mechanism of $PCE_{20k}C$ copolymer. The PEG20k blocks within molecular chains were initially dissolved and released, resulting in a rapid mass loss and the formation of a localized acidic environment. Subsequently, degradation was predominantly driven by PCL blocks, leading to a gradual slowdown in mass loss [42]. However, for the CI-nHA@PCEC composite scaffold, the $PCE_{20k}C$ filaments were firmly wrapped by the CI-nHA matrix, which limited the release of dissolved $PEG_{20}k$, resulting in a slower mass loss than

$PCE_{20k}C$ alone. Moreover, the release of nHA particles along matrix degradation also helped neutralize acidity, further stabilizing the degradation environment.

Besides, the degradation behaviour was further investigated by monitoring the compressive modulus and stress change over time, as shown in Figure 5.4d, e, and f. For CI-nHA matrix, the modulus and stress gradually decreased with degradation time, while $PCE_{20k}C$ maintained mechanical stability without any obvious change on modulus and stress. It is interesting to note that, the modulus of CI-nHA@PCEC composite scaffold remained unchanged with degradation time, while the scaffold at 8 weeks was broken after compressed to around 20%, as shown in the stress-stain curve (Figure 5.6). It is because although the release of $PCE_{20k}C$ was restricted, the hydrophilicity of the CI-nHA matrix accelerated internal $PEG_{20}k$ dissolution, forming voids within the $PCE_{20k}C$ filaments, leading to the fracture under 20% compression strain after 8 weeks.

Overall, CI-nHA matrix accelerated the degradation of the $PCE_{20k}C$ framework and improved the degradation microenvironment, which endow the CI-nHA@PCEC composite scaffold an appropriate degradation rate aligned with the native regeneration timeline of cancellous bone (6–8 weeks) [221], making it a promising candidate for bone regeneration.

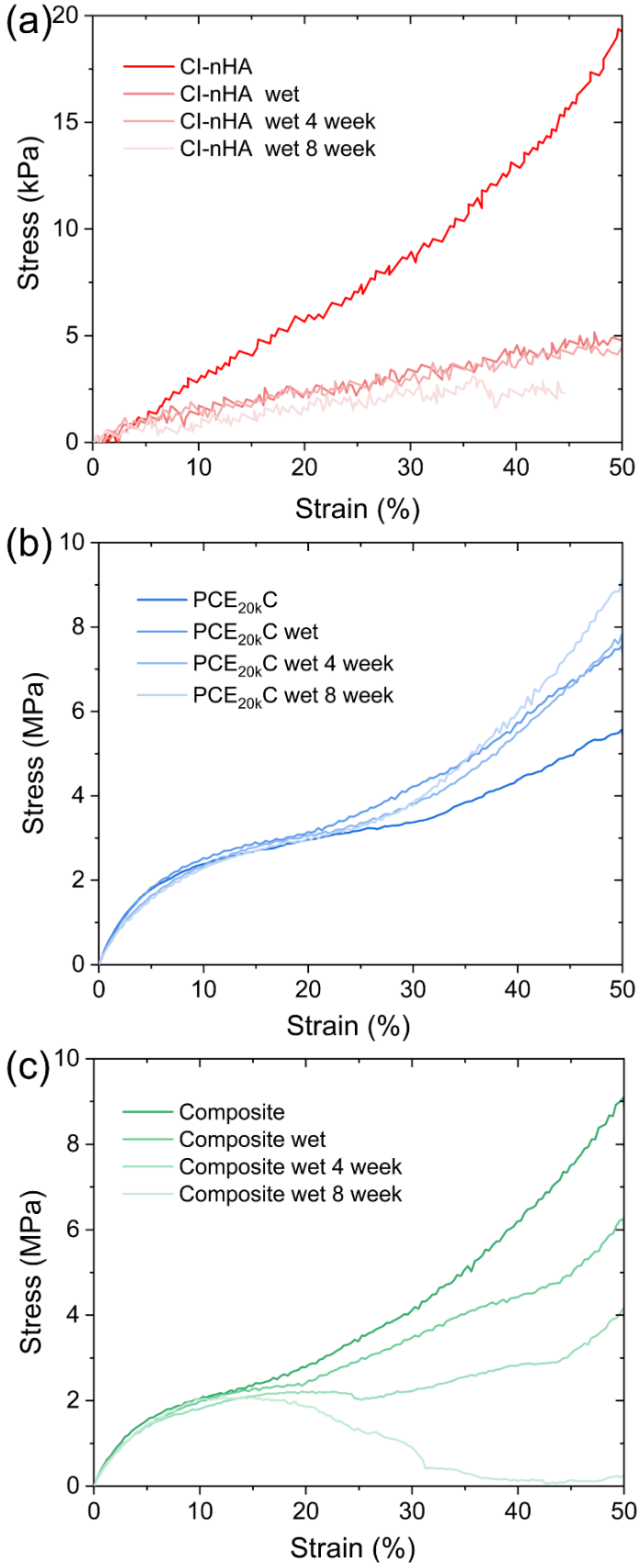

Figure 5.6: Compressive stress-strain curves of (a) CI-nHA, (b) $PCE_{20k}C$ and (c) CI-nHA@PCEC composite scaffolds in dry condition, wet conditions and wet conditions of degradation for 0 week, 4 weeks and 8 weeks.

5.5. Biological performance

5.5.1. Biocompatibility

To assess biocompatibility, the effect of the $PCE_{20k}C$ framework on cell viability and infiltration was evaluated by seeding MC3T3 pre-osteoblast cells onto CI-nHA and CI-nHA@PCEC composite scaffolds. The $PCE_{20k}C$ framework alone was not included in this chapter, as its 3D-printed surface is too smooth to effectively support cell adhesion and growth. Results of metabolic activity over time show that $PCE_{20k}C$ framework did not affect MC3T3 cell viability, evidenced by no negative trend during the cell culture in CI-nHA@PCEC composite scaffold, as shown in Figure 5.7a.

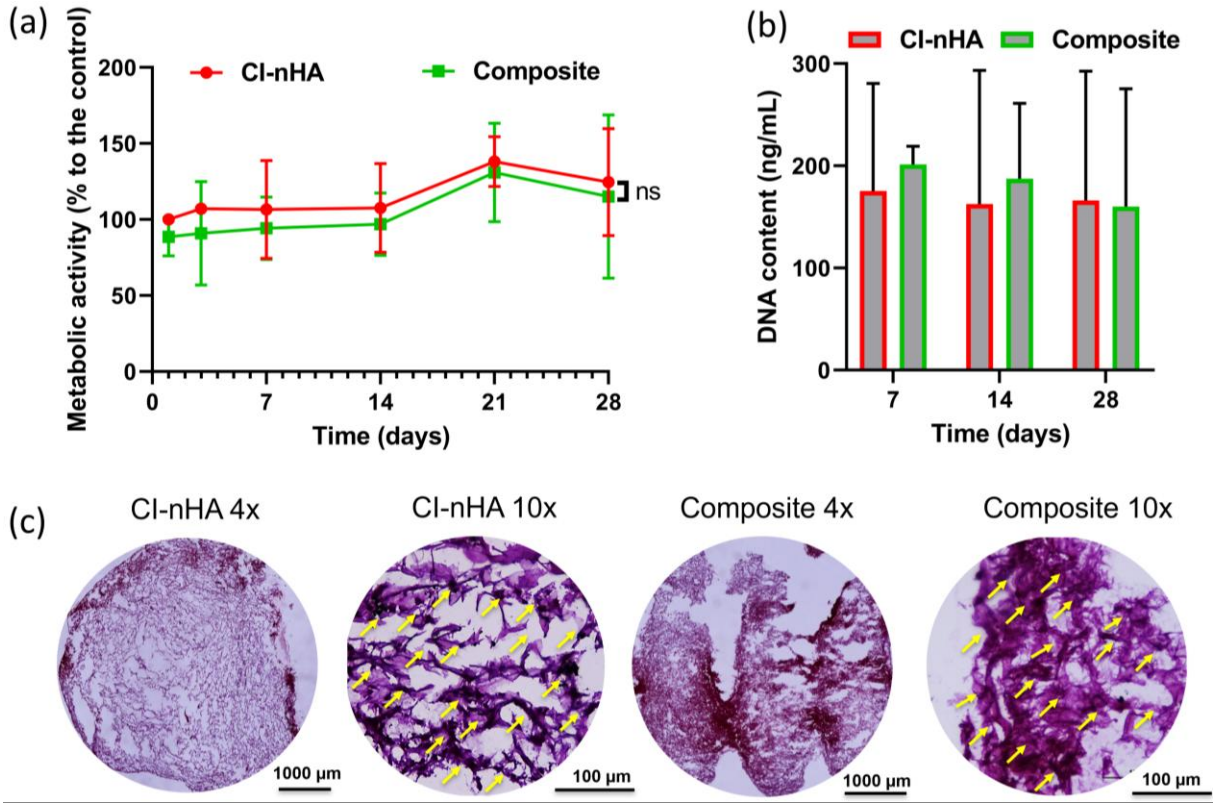

Figure 5.7: (a) Cellular metabolic activity (normalized to CI-nHA scaffold at day 1) measured over 1, 3, 7, 14, 21, and 28 days, (b) DNA content per scaffold after 7, 14, and 28 days of culture and (c) H&E histological staining of both scaffolds after 28 days in culture.

This was further confirmed by no significant difference observed between the CI-nHA and CI-nHA@PCEC composite groups in metabolic activity and DNA

content (Figure 5.7b). More importantly, after culturing for 28 days, the CI-nHA@PCEC composite scaffold exhibited a DNA content of 160.2 ng/mL, which is comparable to that of CI-nHA scaffold (166.1 ng/mL), indicating that the $PCE_{20k}C$ framework does not compromise the biocompatibility.

Additionally, H&E staining revealed cell infiltration within these scaffolds. As shown in Figure 5.7c, cells were primarily localized at edges and gradually migrated inward in CI-nHA scaffold. In contrast, in the CI-nHA@PCEC composite scaffold, cell infiltration was observed not only along the scaffold edges but also in areas in direct contact with $PCE_{20k}C$ filaments. This is because 3D-printed $PCE_{20k}C$ framework helped to increase stiffness and expand internal space of CI-nHA matrix in CI-nHA@PCEC composite scaffold, compared to CI-nHA scaffold alone, leading to a better cell infiltration. Overall, these findings indicate that the integration of the $PCE_{20k}C$ framework had no adverse effects on the biocompatibility, in terms of cell metabolic activity, viability and infiltration over 28 days of culture.

5.5.2. Osteogenesis

Having established the biocompatibility, the osteogenic potential of the composite scaffold was evaluated using the CI-nHA scaffold as a reference. Osteogenesis was confirmed through tests for early bone formation marker ALP, late matrix maturation marker calcium, and bone-related genes expression (COLI, RUNX2, OCN, and BMP-2).

As shown in Figure 5.8a, the quantitative analysis of ALP activity shows no significant difference between the CI-nHA and CI-nHA@PCEC composite groups, where ALP activity significantly increased from 89.7 mg/DNA on day 7 to 593.4 mg/DNA on day 14 in the CI-nHA scaffold ($p < 0.0001$), and from 79.6 mg/DNA on day 7 to 465.3 mg/DNA on day 14 in the CI-nHA@PCEC composite scaffold ($p < 0.001$). Additionally, as a late-stage osteogenic marker, mineralization was further assessed by calcium deposition content (Figure 5.8b). Due to the presence of nHA, original calcium content was 239.6 µg/mL in cell-free CI-nHA scaffold and 261.9 µg/mL in cell-free CI-nHA@PCEC composite scaffold. Notably, significantly

enhanced mineralization by MC3T3 cells was observed, evidenced by the increased calcium content in both cell-seeded scaffolds on day 21 ($p < 0.01$) and day 28 ($p < 0.0001$), where highest calcium levels appeared on day 28, reaching 500.9 μg/mL in CI-nHA scaffold and 495.0 μg/mL in CI-nHA@PCEC composite scaffold. Mineralization was further assessed using Alizarin Red S staining (Figure 5.8c). After 28 days of differentiation, dark red mineral deposits were evenly distributed in both the CI-nHA matrix and composite scaffold, with no notable differences in distribution. These results all indicate the ability to support effective ALP activity and mineralization.

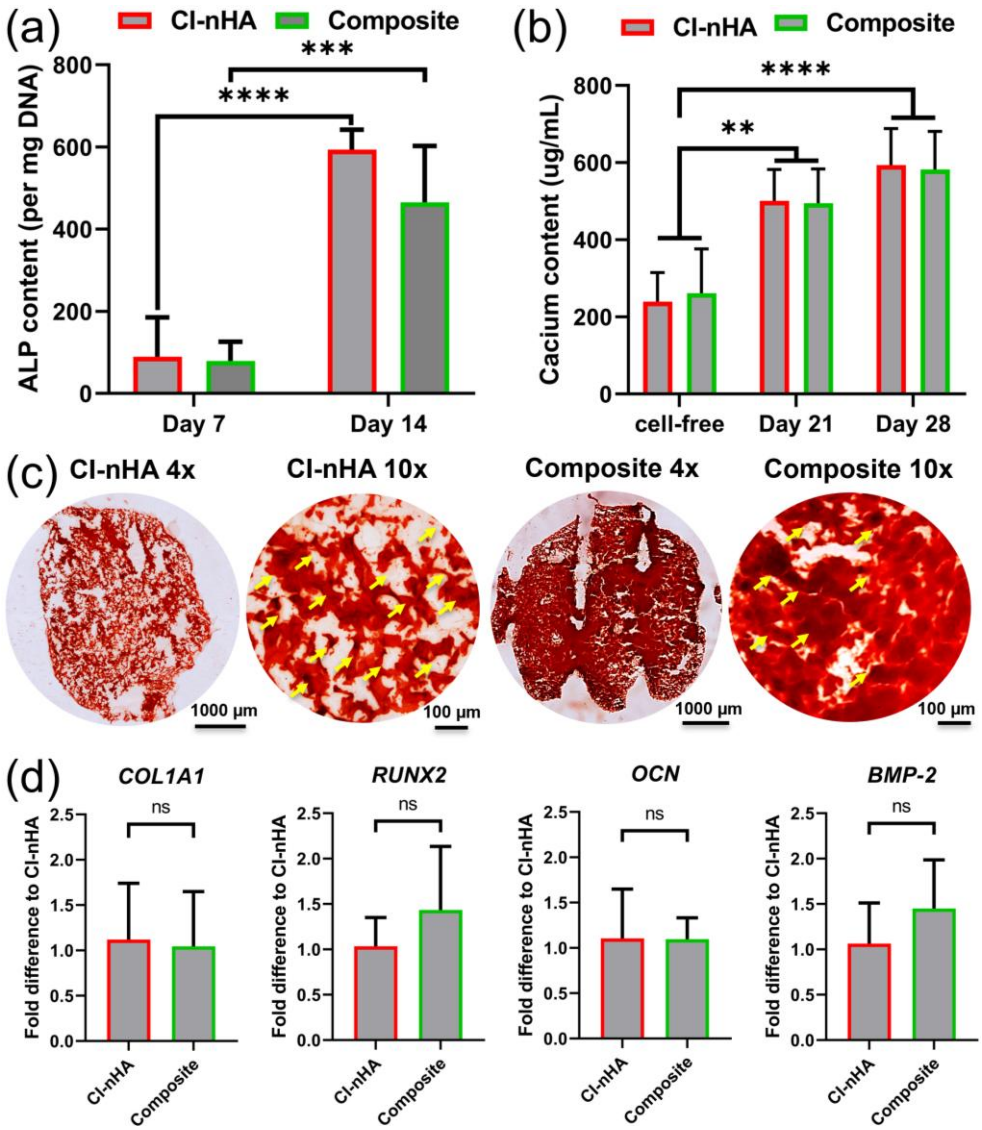

Figure 5.8: Osteogenic differentiation of MC3T3 cells on CI-nHA and composite scaffolds. (a) ALP content in MC3T3 cells cultured on scaffolds at day 7 and 14, (b) calcium content in MC3T3 cells on scaffolds at days 21 and 28, (c) Alizarin Red S histological staining at day 28, and (d) relative gene expression of COL1A1, RUNX2, OCN and BMP-2 at day 21.

Moreover, Figure 5.8d illustrates the relative expression of osteogenesis-related genes COL1A1, RUNX2, OCN, and BMP-2 after 21 days of differentiation. Gene expression levels in the CI-nHA@PCEC composite scaffold were comparable to those in the CI-nHA scaffold, with no significant differences observed. Notably, higher expression of RUNX2 and BMP-2 genes observed in CI-nHA@PCEC composite scaffold. This is because the 3D-printed $PCE_{20k}C$ framework helped to increase stiffness and expand internal space of CI-nHA matrix in CI-nHA@PCEC composite scaffold, compared to CI-nHA scaffold alone, leading to the activation of mechanotransduction through the YAP/TAZ and Wnt signalling pathways [222]. This also can be confirmed by the increased cell infiltration shown in H&E staining compared to CI-nHA scaffold (Figure 5.7c).

Overall, these results demonstrate that the CI-nHA@PCEC composite scaffold effectively supports ALP activity, mineralization, and bone-related gene expression, all of which shows consistent results with CI-nHA scaffold studies [223].

5.5.3. Angiogenesis

Bone tissue is highly vascularized. In the early stages of bone repair, vascularization plays a crucial role by supplying osteocytes with essential nutrients and supporting subsequent bone formation [45]. Previous studies have shown that CI-nHA-based scaffolds effectively stimulate MSC vascularization [43]. Therefore, the angiogenic potential of these scaffolds was evaluated by culturing EA.hy 926 endothelial cells on CI-nHA and CI-nHA@PCEC composite scaffolds for five days.

Cell proliferation increased steadily from day 1 to day 5, with tube-like structures forming on both scaffolds, as shown in Figure 5.9a-d. Moreover, after 5 days in culture, the expression levels of key vascular-related genes of VEGF, VE-cadherin, and MMP-2, remained comparable between the composite and CI-nHA scaffolds, with no significant differences (Figure 5.8e, f and g), suggesting the presence of early angiogenic signals within this period. These findings confirm that the CI-nHA@PCEC composite scaffold fully preserves the angiogenic properties of

the CI-nHA matrix, supporting endothelial cell proliferation and vascularization. Overall, it can be confirmed that the CI-nHA@PCEC composite scaffold holds great potential to promote bone defect repair through osteogenic-angiogenic coupling.

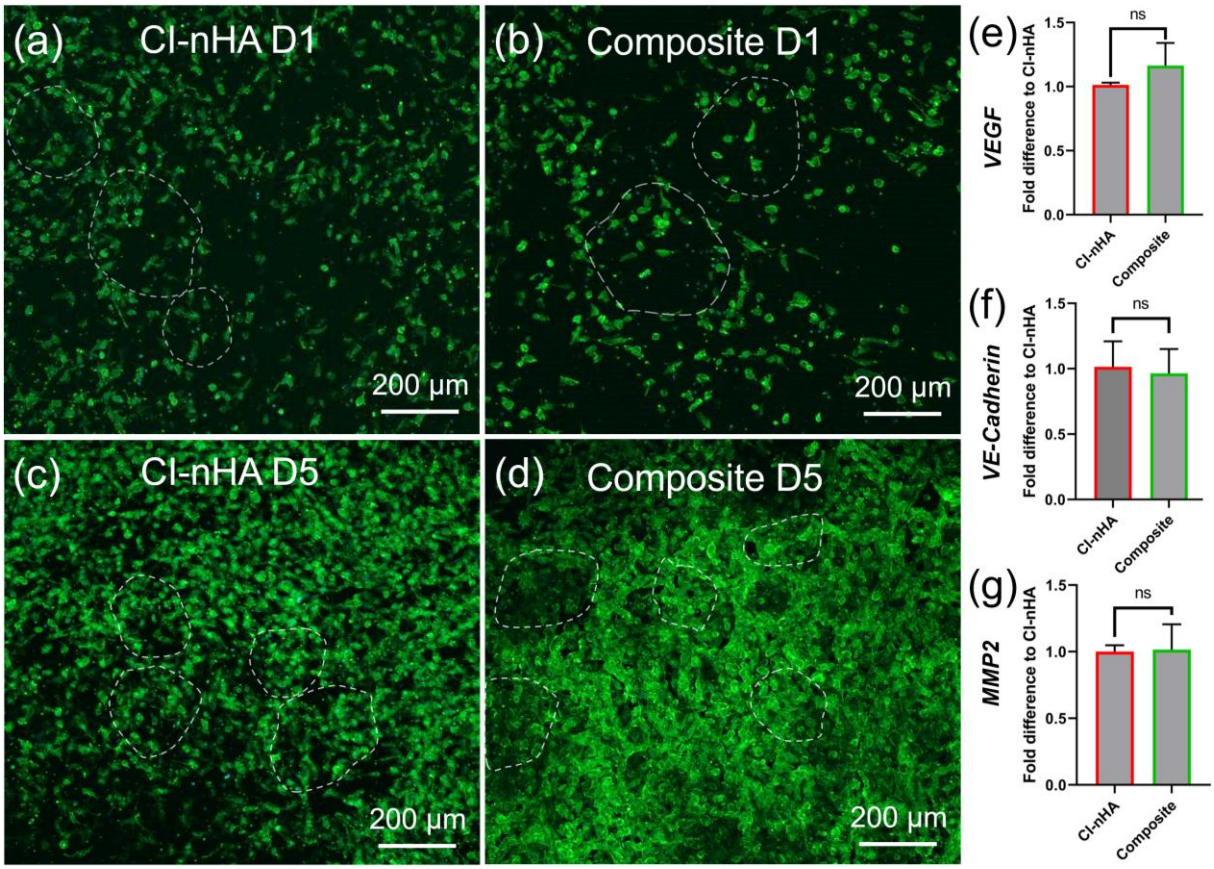

Figure 5.9: Angiogenic differentiation of EA.hy 926 cells on scaffolds. Confocal images of (a) cells on the CI-nHA scaffold at day 1, (b) cells on the composite scaffold at day 1, (c) cells on the CI-nHA scaffold at day 5, and (d) cells on the composite scaffolds at day 5; Relative gene expression of (e) VEGF, (f) VE-cadherin, and (g) MMP-2 of EA.hy 926 cells on both scaffolds after 5 days.

5.6. Conclusions

In this chapter, a novel biomimetic composite scaffold (CI-nHA@PCEC) was fabricated, in which the 3D-printed $PCE_{20k}C$ framework served as mechanical reinforcement for tissue growth, and the CI-nHA matrix served as biological cues for tissue regeneration. It exhibited hierarchical architecture, mechanical properties similar to cancellous bone, degradation rate matching with bone regeneration rate, and a mild degradation environment. The CI-nHA@PCEC

composite scaffold sustained the ability of osteogenic-angiogenic coupling from CI-nHA matrix, while mechanotransduction induced by 3D-printed $PCE_{20k}C$ framework promoted osteogenesis, which are both expected to achieve effective bone repair efficiency. Therefore, this biomimetic composite scaffold has broad application prospects as a promising scaffold for enhanced bone defect repair.

6. Processing, structure and properties of bilayer composite scaffold

6.1. Introduction

Osteochondral defect repair involves articular cartilage repair and underlying subchondral bone repair. It remains a great challenge in clinical treatment due to the gradient in structure and properties across different tissue layers [173][224]. Specifically, subchondral bone is highly vascularized and undergoes continuous remodelling, allowing for relatively faster healing. In contrast, articular cartilage is avascular, with chondrocytes that exhibit low metabolic activity and limited proliferative capacity, resulting in poor repair efficiency. Despite their distinct properties, subchondral bone and cartilage are closely interconnected and communicated in osteochondral tissue through micro vessels and channels [225][96]. Current treatments, such as microfracture, autologous transplantation, and allograft transplantation, often fail to restore the native structure and function of the osteochondral unit [226][227]. Therefore, tissue engineering has emerged as a promising approach aimed at regenerating complex tissue interfaces by integrating biomaterials, cells, and bioactive factors.

Recent advances in 3D printing technology have enabled the fabrication of scaffolds with precisely controlled architecture, porosity, and spatial composition. This capability is particularly important for osteochondral tissue engineering because it allows to reproduce the structural and functional gradients in the native tissue [228]. Common strategies involve the development of multiphase scaffolds that integrate both cartilage and bone regeneration approaches within a single construct [229]. These scaffolds aim to provide localized chemical, mechanical, and biological cues to support cell proliferation, differentiation, and tissue formation in a layer-specific manner, and they have shown promising outcomes in preclinical animal studies, such as rabbits [192] and caprine [193]. Despite some progress, most designs fall short in providing appropriate

mechanical support and degradation rates that match those of the native tissue, leading to potential risk of compromised structural integrity during treatment, such as hydrogel-based scaffolds [230]. Additionally, poor interface bonding between layers can result in delamination or phase separation, hindering the overall performance [231]. Therefore, there is an urgent need to develop novel multiphasic scaffolds with continuous architecture, appropriate mechanical properties, and matched degradation rates to enhance osteochondral tissue repair efficiency.

This chapter aims to obtain a bilayer scaffold with continuous structure, appropriate mechanical properties, degradation behaviour and biological performance for osteochondral tissue engineering. This will be achieved by bonding the CI/II-HyA@PGS scaffold developed in Chapter 4 as the cartilage layer and the CI-nHA@PCEC scaffold developed in Chapter 5 as the subchondral bone layer. The mechanical properties in wet conditions will be studied under compression, while cyclic compression under different applied strains will be performed simultaneously to evaluate the fatigue behaviour. Finally, real-time mass and pH evaluation will be analysed by immersion in PBS solution for up to 8 weeks to assess the degradation behaviour.

6.2. Processing and Structure

An innovative biomimetic bilayer composite scaffold was fabricated with a continuous structure consisting of a soft cartilage layer and a stiff subchondral bone layer. Briefly, PGS and PCEC scaffolds with porous structures were obtained by 3D printing. Then, two biomimetic composite scaffolds were made by incorporation with CI/II-HyA and CI-nHA matrices, respectively. Finally, the surface of the CI-nHA@PCEC scaffold was dissolved with CH_2Cl_2 and pressed onto the CI/II-HyA@PGS scaffold to obtain a bilayer composite scaffold. The CI/II-HyA@PGS scaffold was used as the top cartilage layer and the CI-nHA@PCEC scaffold was used as the bottom subchondral bone layer, as shown in Figure 6.1.

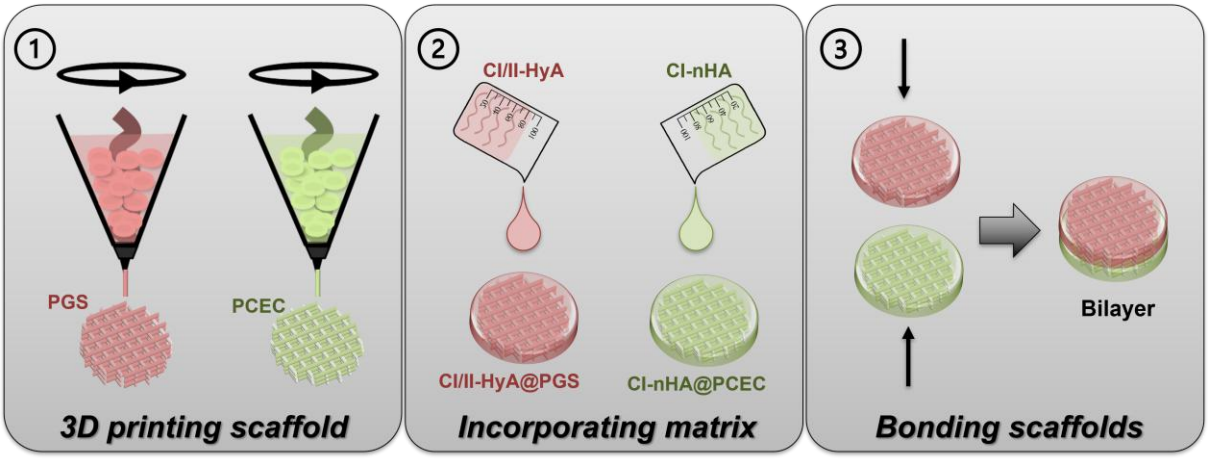

Figure 6.1: The fabrication process of bilayer composite scaffold consisting of CI/II-HyA@PGS scaffold as the cartilage layer and CI-nHA@PCEC as the subchondral bone layer.

The morphology of CI/II-HyA@PGS, CI-nHA@PCEC and bilayer composite scaffolds is shown in Figure 6.2. SEM images revealed distinct morphologies between top and bottom layers, with a clear boundary observed at the bonding interface. The upper layer, made up of the CI/II-HyA@PGS scaffold, exhibited rough and porous PGS filaments embedded within a porous CI/II-HyA matrix. The lower layer, made up of the CI-nHA@PCEC scaffold, displayed smooth and dense PCEC filaments surrounded by a porous CI-nHA matrix. Notably, the pore sizes of matrices differed between the two layers, where the size of the CI/II-HyA matrix pores was approximately 155 μm, suitable for cartilage regeneration [191], while the CI-nHA matrix exhibited smaller pores of around 100 μm, favourable for bone regeneration [220]. Importantly, the polymer dissolution for bonding was only localized at the interface, and the bilayer scaffold retained the original printed porous structure and maintained the continuity of the interface. These results confirm the successful integration of both scaffolds to obtain the bilayer scaffold with different compositions and morphology in each layer.

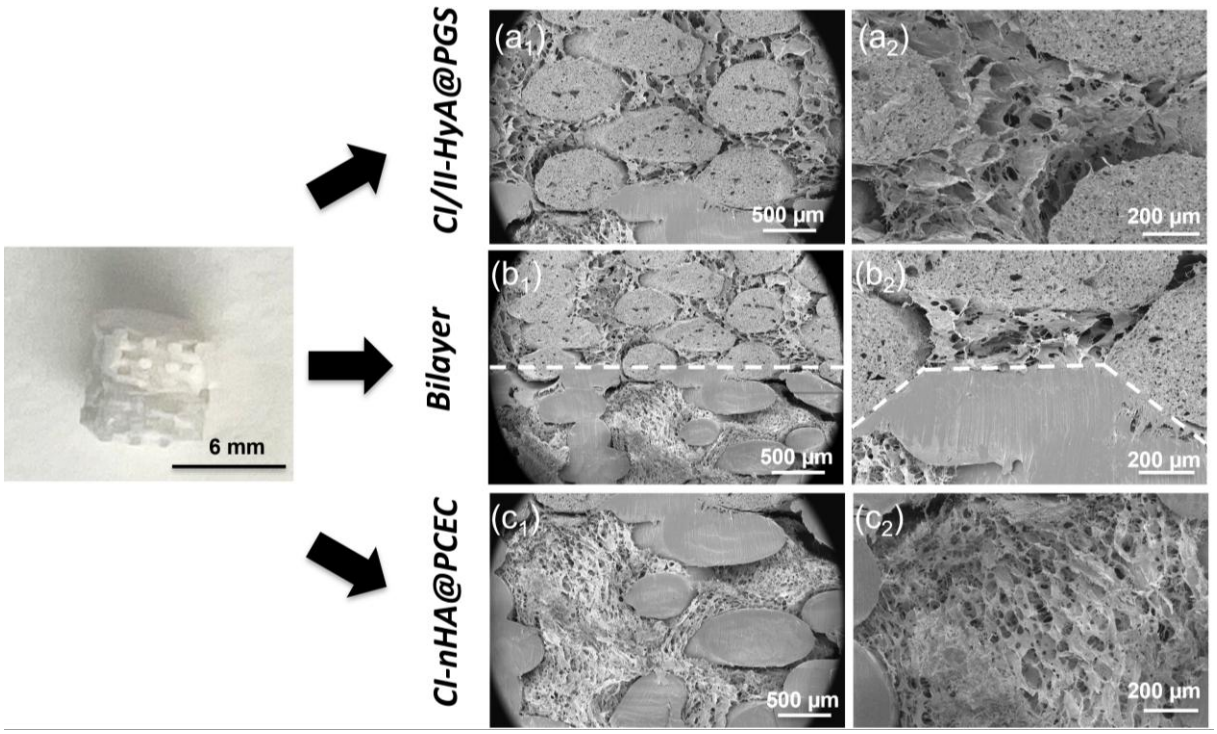

Figure 6.2: Optical images of the bilayer composite scaffold and SEM images of (a) CI/II-HyA@PGS, (b) bilayer and (c) CI-nHA@PCEC composite scaffolds.

6.3. Mechanical properties

The mechanical properties of osteochondral tissue gradually change from soft to stiff from the cartilage to the subchondral bone regions, depending on their composition and structure. In this section, the mechanical properties of CI/II-HyA@PGS scaffold for cartilage repair and CI-nHA@PCEC scaffold for subchondral repair, as well as of the bilayer composite scaffold for osteochondral tissue regeneration were measured through compression tests under PBS solution (wet) conditions.

Figure 6.3a, c, and d present the stress-strain curves in compression, as well as the corresponding elastic modulus and compressive strength of the CI/II-HyA@PGS, CI-nHA@PCEC, and bilayer composite scaffolds. As shown in Figure 6.3a, the soft upper layer composed of CI/II-HyA@PGS scaffold was initially compressed, resulting in a compression modulus of 0.142 MPa, which closely matched that of the CI/II-HyA@PGS scaffold alone (0.141 MPa), as depicted in Figure 6.3c. When the strain reached approximately 20%, the stiffer lower layer

of CI-nHA@PCEC began to bear the load, leading to a rapid increase in stiffness and strength. Ultimately, the bilayer scaffold exhibited a compressive strength at 50% that is in between those of the individual layers (Figure 6.3d).

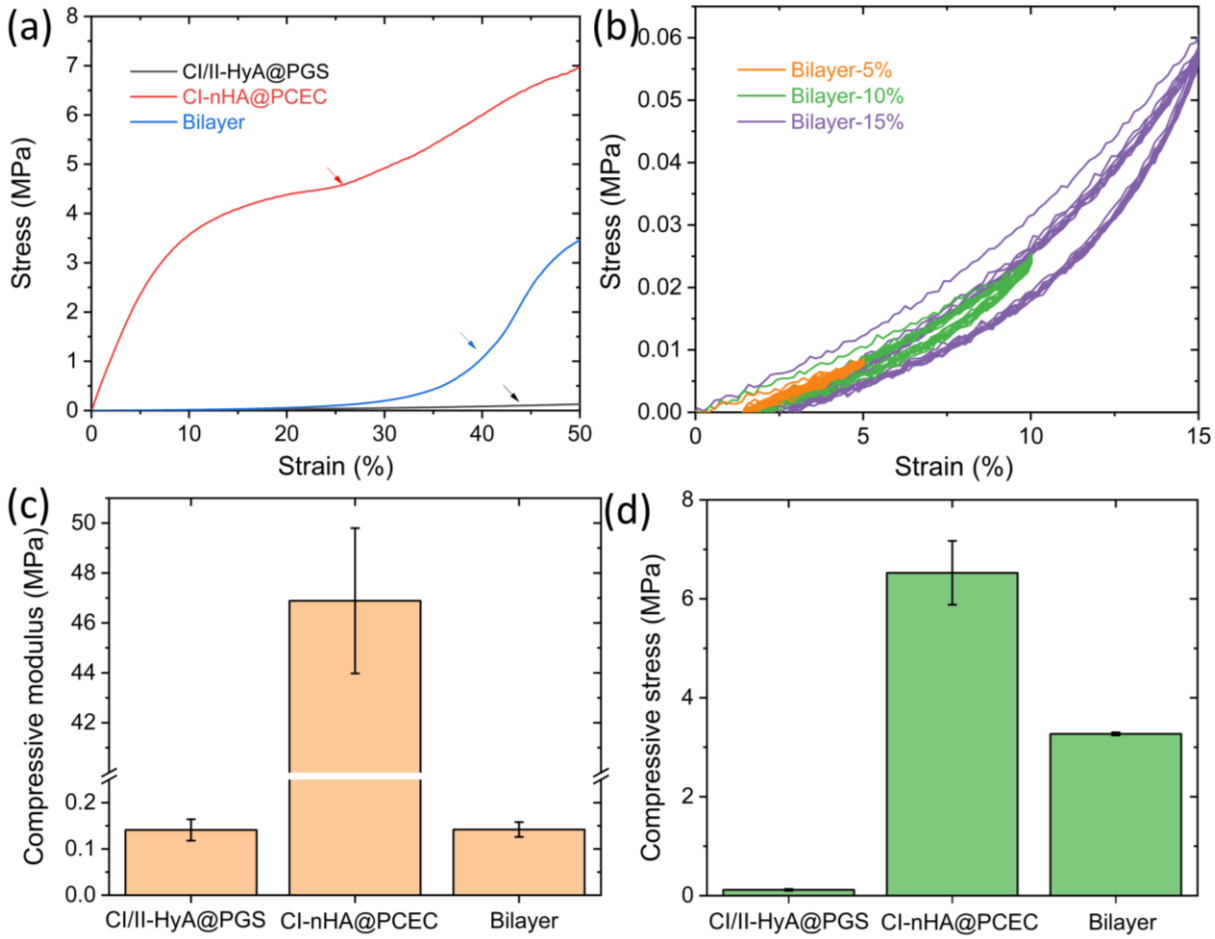

Figure 6.3: (a) Stress-strain curves in compression, (b) cyclic stress-strain curves in compression of bilayer composite scaffold at strains of 5%, 10% and 15%, (c) elastic modulus and (d) compressive strength of CI/II-HyA@PGS, CI-nHA@PCEC, and bilayer composite scaffolds.

More importantly, as shown in Table 6.1, the elastic modulus of the CI/II-HyA@PGS scaffold is 0.141 MPa, which is within the range of native cartilage (0.1-2 MPa). Similarly, the CI-nHA@PCEC scaffold exhibited an elastic modulus of 48.8 MPa, within the range of native cancellous bone (10-3,000 MPa). These findings confirm that each layer of the scaffold mimics the mechanical properties of its corresponding native tissue. Moreover, other investigations have shown that the cartilage deformation in osteochondral tissue under normal loading conditions

is about 2% - 9% of its height, while bone deformation is below 1% [232]. Therefore, ensuring good elasticity in a safe deformation range is crucial for osteochondral tissue regeneration.

Cyclic compression tests under dynamic strains of 5%, 10%, and 15% were conducted to evaluate the elasticity of the bilayer composite scaffold. As shown in Figure 6.3b, a complete elastic recovery was found at all strains, while some hysteresis was observed at a high strain of 15%, indicating a good elasticity in the physiological environment. Overall, these results demonstrate that the bilayer composite scaffold exhibits a successful transition from soft to hard mechanical properties as well as an elastic response up to large strains, making it a promising candidate for osteochondral tissue engineering.

Table 6.1: Compressive parameters of CI/II-HyA@PGS, CI-nHA@PCEC, and bilayer composite scaffolds in wet conditions

Sample	Elastic modulus (MPa)	Compressive strength (MPa)
CI/II-HyA@PGS	0.141 ± 0.023	0.117 ± 0.018
CI-nHA@PCEC	46.9 ± 2.9	6.53 ± 0.65
Bilayer	0.142 ± 0.016	3.27 ± 0.03

6.4. Degradation behaviour

The degradation behaviour of CI/II-HyA@PGS, CI-nHA@PCEC and bilayer composite scaffolds was studied by immersion in PBS solution at 37 °C for 8 weeks. Figure 6.4 presents the evolution of the residual mass and pH of these scaffolds during *in vitro* degradation. As shown in Figure 6.4a, the mass of CI/II-HyA@PGS, CI-nHA@PCEC and bilayer composite scaffolds gradually decreased over time, and the residual mass after 8 weeks was 94.1%, 92.1% and 92.6%, respectively. Notably, the residual mass of all scaffolds remained above 90% within this period, indicating that all scaffolds maintained structural stability during the critical early period of osteochondral repair, while allowing for gradual degradation over time.

Moreover, although the pH changes followed a similar trend to that shown in the previous chapters, the bilayer composite scaffold exhibited a milder degradation, compared to the other single scaffolds after degradation for 2 weeks (Figure 6.4b). This can be attributed to the initial release of PEG20k in CI-nHA@PCEC layer, which formed a transient local acidic environment. Subsequently, the release of nHA particles from the matrix helped to neutralize the acidity, thereby stabilizing the pH. In contrast, the hydrolysis of ester bonds in PGS and the release of hyaluronic acid in the CI/II-HyA@PGS scaffold generated a localized acidic environment, without any compound to buffer the pH. Therefore, by integrating both layers, the bilayer scaffold effectively overcame the limitations of single-layer systems, achieving a more balanced and mild degradation environment. These findings demonstrate that the bilayer scaffold not only retains structural integrity over time but also provides a more favourable degradation microenvironment, making it a suitable candidate for supporting early-stage osteochondral tissue regeneration.

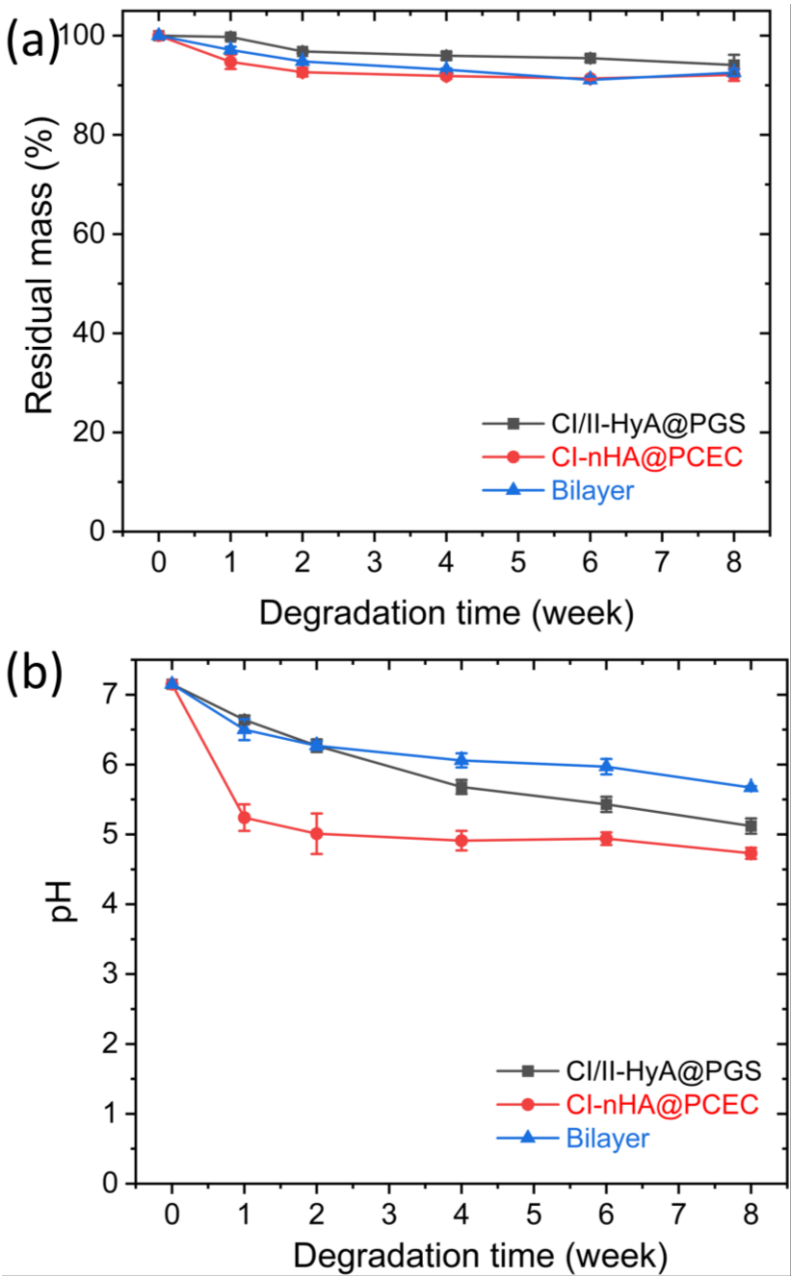

Figure 6.4: *In vitro* degradation behaviour with time on (a) residual mass, (b) pH change of CI/II-HyA@PGS, CI-nHA@PCEC and bilayer composite scaffolds.

6.5. Conclusions

A novel biomimetic bilayer composite combining CI/II-HyA@PGS (cartilage layer) and CI-nHA@PCEC (subchondral bone layer) was successfully fabricated via in-situ bonding. It showed different composition and morphology in each layer and was able to reproduce the mechanical properties of the cartilage and the subchondral bone layers. More importantly, it exhibits a transition from soft to

hard mechanical properties and elasticity under physiological conditions. Additionally, it maintained structural stability and a mild environment during the degradation in early period of osteochondral repair, while allowing for gradual degradation over time. Based on the chondrogenic analysis in Chapter 4 and osteogenic analysis in Chapter 5, it can be assumed that the bilayer composite scaffold with appropriate structure, mechanical properties, degradation behaviour, and biological performance shows potential to be used for osteochondral tissue defect repair.

7. Conclusions and future work

7.1. Conclusions

This thesis aimed to develop 3D-printed biodegradable polymer scaffolds with biomimetic structure, appropriate mechanical properties, matched degradation rates and effective biological performance with respect to native osteochondral tissue. The main conclusions of the results presented in this thesis are the following:

- Biodegradable PCEC triblock co-polymers with high molecular weight were synthesized from PEG with a wide range of molecular weights (from 0.6 kg/mol to 35 kg/mol) as macroinitiators. PCEC copolymers exhibited tunable mechanical properties with an elastic modulus in the range 338-705 MPa and a degradation rate from 60% mass loss after 8 h up to 70% mass loss after 23 days in accelerated tests, as well as excellent cytocompatibility and cell attachment after culture with mouse fibroblast L929 cells. Furthermore, it was shown that it is possible to manufacture PCEC scaffolds by 3D printing with excellent dimensional accuracy and controlled microporosity.

- A novel composite scaffold (CI/II-HyA@PGS) with hierarchical porosity was manufactured by incorporating a pro-chondrogenic collagen type I/II-hyaluronic acid (CI/II-HyA) matrix to a 3D-printed poly (glycerol sebacate) (PGS) framework. Based on the mechanical properties of PGS framework, the CI/II-HyA@PGS composite scaffold exhibited an elastic modulus of 167.0 kPa, similar to that of native cartilage, as well as excellent fatigue resistance, similar to that of the native joint tissue. *In vitro* degradation tests demonstrated that the CI/II-HyA@PGS composite scaffold maintained structural, mass, and mechanical stability during the initial cartilage regeneration period of 4 weeks, while degraded linearly over time. *In vitro* biological tests with rat-derived mesenchymal stem cell (MSC) revealed that the CI/II-HyA@PGS composite scaffold displayed increased cell loading efficiency and improved overall cell viability due to the incorporation of the CI/II-HyA matrix. Additionally, it also sustained MSC chondrogenesis and *de-novo*

cartilage-like matrix deposition up to day 28. These results demonstrate that the biomimetic CI/II-HyA@PGS composite scaffold presents a great potential for cartilage defect repair.

- Another novel biomimetic composite scaffold (CI-nHA@PCEC) was fabricated by incorporating a bioactive matrix including bone components of collagen type I and nano-hydroxyapatite (CI-nHA) into a 3D-printed porous framework manufactured by a $PCE_{20k}C$ triblock copolymer. The CI-nHA@PCEC composite scaffold showed a highly porous and hierarchical structure, as well as an elastic modulus of 37.0 MPa, similar to that of native cancellous bone. In addition, it maintained structural and mass stability during the initial repair period of bone regeneration of 8 weeks, while gradually degraded afterwards. *In vitro* biological experiments demonstrated that, based on the bioactivity of CI-nHA matrix, the CI-nHA@PCEC composite scaffold sustained osteogenesis and mineralization of pre-osteoblast cells (MC3T3) up to 28 days, as well as supported luminal formation and angiogenesis of endothelial cells (EA.hy 926) after 5 days. In addition, the increased stiffness and internal space from 3D-printed $PCE_{20k}C$ framework, slightly upregulated the expression of RUNX2 and BMP-2 genes through mechanotransduction to promote osteogenesis. These results demonstrate that this novel biomimetic CI-nHA@PCEC composite scaffold shows potential as candidate for critical-size bone defect repair.

- Finally, a biomimetic bilayer scaffold manufactured by in-situ bonding the CI/II-HyA@PGS scaffold (targeting the cartilage layer) and the CI-nHA@PCEC scaffold (targeting the subchondral bone layer). The bilayer composite scaffold presented different compositions and porous morphologies at top and bottom layers, with a distinct boundary at the bonding interface. The elastic modulus of 0.141 MPa in the top layer was in the range of native cartilage (0.1-2 MPa) while that of in the bottom layer (48.8 MPa) was in the range of cancellous bone (10-3,000 MPa). Additionally, it showed an excellent elasticity within the range of osteochondral deformation under normal loading conditions. Besides, *in vitro* degradation tests demonstrated that the bilayer composite scaffold maintained mass stability during the initial osteochondral regeneration period of 8 weeks, while provided a more

favourable degradation microenvironment than both single layer scaffolds. Taking together the biological performance results of both single layers, the bilayer composite scaffold shows great potential for osteochondral tissue engineering.

7.2. Future work

The following activities are proposed as future work:

- Biological tests were only conducted in two single-layer scaffolds, lacking research on the overall biological performance of the bilayer composite scaffold. Future work will focus on studying cell behaviour of MSC seeded on bilayer scaffold to observe the synergistic effect of both layers on biological performance.

- Osteochondral tissue is frequently exposed to complex stress environments *in vivo* due to the host movements, including unstable compression and shear forces. This thesis only tested mechanical properties under normal compression. Investigations into long-term fatigue behaviour under more complex, dynamic stress conditions need to be considered in the future.

- Beyond scaffold composition, external mechanical stimulation also plays a crucial role in osteochondral defect repair. Prior to the *in vivo* test, the cell-seeded bilayer composite scaffold should be introduced in a bioreactor with simulated physiological motive conditions to understand the effects and mechanisms of mechanical stimulations on osteochondral tissue regeneration.

- Investigations on *in vivo* degradation and *in vivo* biological performance of tissue-engineered implants are critical for assessing their clinical potential. Future research will focus on implanting the bilayer composite scaffold into animal models such as rabbits or goats, to monitor and record degradation behaviour and tissue regeneration over time.

Bibliography

[1] R. Zhang, Donor-specific antibodies in kidney transplant recipients, Clinical Journal of the American Society of Nephrology 13 (2018) 182–192. https://doi.org/10.2215/CJN.00700117.

[2] F. Zhang, M.W. King, Biodegradable Polymers as the Pivotal Player in the Design of Tissue Engineering Scaffolds, Adv Healthc Mater 9 (2020) 1901358. https://doi.org/https://doi.org/10.1002/adhm.201901358.

[3] I. Cockerill, Y. Su, S. Sinha, Y.X. Qin, Y. Zheng, M.L. Young, D. Zhu, Porous zinc scaffolds for bone tissue engineering applications: A novel additive manufacturing and casting approach, Materials Science and Engineering C 110 (2020). https://doi.org/10.1016/j.msec.2020.110738.

[4] M. Mohammadi Zerankeshi, S. Mofakhami, E. Salahinejad, 3D porous HA/TCP composite scaffolds for bone tissue engineering, Ceram Int 48 (2022) 22647–22663. https://doi.org/10.1016/j.ceramint.2022.05.103.

[5] M.M. Pérez-Madrigal, J.E. Shaw, M.C. Arno, J.A. Hoyland, S.M. Richardson, A.P. Dove, Robust alginate/hyaluronic acid thiol-yne click-hydrogel scaffolds with superior mechanical performance and stability for load-bearing soft tissue engineering, Biomater Sci 8 (2020) 405–412. https://doi.org/10.1039/c9bm01494b.

[6] D. Aki, S. Ulag, S. Unal, M. Sengor, N. Ekren, C.C. Lin, H. Yılmazer, C.B. Ustundag, D.M. Kalaskar, O. Gunduz, 3D printing of PVA/hexagonal boron nitride/bacterial cellulose composite scaffolds for bone tissue engineering, Mater Des 196 (2020). https://doi.org/10.1016/j.matdes.2020.109094.

[7] H.S. Han, S. Loffredo, I. Jun, J. Edwards, Y.C. Kim, H.K. Seok, F. Witte, D. Mantovani, S. Glyn-Jones, Current status and outlook on the clinical translation of biodegradable metals, Materials Today 23 (2019) 57–71. https://doi.org/10.1016/j.mattod.2018.05.018.

[8] N. Sezer, Z. Evis, M. Koç, Additive manufacturing of biodegradable magnesium implants and scaffolds: Review of the recent advances and research trends, Journal of Magnesium and Alloys 9 (2021) 392–415. https://doi.org/10.1016/j.jma.2020.09.014.

[9] Y. Li, H. Jahr, K. Lietaert, P. Pavanram, A. Yilmaz, L.I. Fockaert, M.A. Leeflang, B. Pouran, Y. Gonzalez-Garcia, H. Weinans, J.M.C. Mol, J. Zhou, A.A. Zadpoor, Additively manufactured biodegradable porous iron, Acta Biomater 77 (2018) 380–393. https://doi.org/10.1016/j.actbio.2018.07.011.

[10] C. Shuai, S. Li, S. Peng, P. Feng, Y. Lai, C. Gao, Biodegradable metallic bone implants, Mater Chem Front 3 (2019) 544–562. https://doi.org/10.1039/c8qm00507a.

[11] H. Ma, C. Feng, J. Chang, C. Wu, 3D-printed bioceramic scaffolds: From bone tissue engineering to tumor therapy, Acta Biomater 79 (2018) 37–59. https://doi.org/10.1016/j.actbio.2018.08.026.

[12] A. Kirillova, T.R. Yeazel, D. Asheghali, S.R. Petersen, S. Dort, K. Gall, M.L. Becker, Fabrication of Biomedical Scaffolds Using Biodegradable Polymers, Chem Rev 121 (2021) 11238–11304. https://doi.org/10.1021/acs.chemrev.0c01200.

[13] C. Pei, H. Zhang, Y. Li, Z. Gu, X. Chen, T. Kuang, Robust and durable biodegradable polymer-based triboelectric nanogenerators enabled by trace amounts of melanin-like nanoparticles, Nano Energy 135 (2025). https://doi.org/10.1016/j.nanoen.2025.110643.

[14] T. Kuang, J. Zhang, G.M. Huang, T. Liu, Z.X. Huang, Multifunctional biopolymer poly (lactic acid)-based triboelectric nanogenerator via controlled construction of secondary electron path, Nano Energy 128 (2024). https://doi.org/10.1016/j.nanoen.2024.109877.

[15] B. Huzum, B. Puha, R. Necoara, S. Gheorghevici, G. Puha, A. Filip, P. Sirbu, O. Alexa, Biocompatibility assessment of biomaterials used in orthopedic devices: An overview (Review), Exp Ther Med 22 (2021). https://doi.org/10.3892/etm.2021.10750.

[16] M.S.B. Reddy, D. Ponnamma, R. Choudhary, K.K. Sadasivuni, A comparative review of natural and synthetic biopolymer composite scaffolds, Polymers (Basel) 13 (2021). https://doi.org/10.3390/polym13071105.

[17] I.M. Adel, M.F. Elmeligy, N.A. Elkasabgy, Conventional and Recent Trends of Scaffolds Fabrication: A Superior Mode for Tissue Engineering, Pharmaceutics 14 (2022). https://doi.org/10.3390/pharmaceutics14020306.

[18] M.P. Nikolova, M.S. Chavali, Recent advances in biomaterials for 3D scaffolds: A review, Bioact Mater 4 (2019) 271–292. https://doi.org/10.1016/j.bioactmat.2019.10.005.

[19] A.-V. Do, B. Khorsand, S.M. Geary, A.K. Salem, 3D Printing of Scaffolds for Tissue Regeneration Applications, Adv Healthc Mater 4 (2015) 1742–1762. https://doi.org/https://doi.org/10.1002/adhm.201500168.

[20] A. Gaspar-Pintiliescu, A.M. Stanciuc, O. Craciunescu, Natural composite dressings based on collagen, gelatin and plant bioactive compounds for wound healing: A review, Int J Biol Macromol 138 (2019) 854–865. https://doi.org/10.1016/j.ijbiomac.2019.07.155.

[21] E. Sayin, R.H. Rashid, J.C. Rodríguez-Cabello, A. Elsheikh, E.T. Baran, V. Hasirci, Human adipose derived stem cells are superior to human osteoblasts (HOB) in bone tissue engineering on a collagen-fibroin-ELR blend, Bioact Mater 2 (2017) 71–81. https://doi.org/10.1016/j.bioactmat.2017.04.001.

[22] K.S. Tsai, S.Y. Kao, C.Y. Wang, Y.J. Wang, J.P. Wang, S.C. Hung, Type I collagen promotes proliferation and osteogenesis of human mesenchymal stem cells via activation of ERK and Akt pathways, J Biomed Mater Res A 94 (2010) 673–682. https://doi.org/10.1002/jbm.a.32693.

[23] B. Gurumurthy, A. V. Janorkar, Improvements in mechanical properties of collagen-based scaffolds for tissue engineering, Curr Opin Biomed Eng 17 (2021). https://doi.org/10.1016/j.cobme.2020.100253.

[24] K. Han, Q. Bai, W. Wu, N. Sun, N. Cui, T. Lu, Gelatin-based adhesive hydrogel with self-healing, hemostasis, and electrical conductivity, Int J Biol Macromol 183 (2021) 2142–2151. https://doi.org/10.1016/j.ijbiomac.2021.05.147.

[25] G. Mugnaini, R. Gelli, L. Mori, M. Bonini, How to Cross-Link Gelatin: The Effect of Glutaraldehyde and Glyceraldehyde on the Hydrogel Properties, ACS Appl Polym Mater 5 (2023) 9192–9202. https://doi.org/10.1021/acsapm.3c01676.

[26] Y. Zhu, X. Yu, H. Liu, J. Li, M. Gholipourmalekabadi, K. Lin, C. Yuan, P. Wang, Strategies of functionalized GelMA-based bioinks for bone regeneration: Recent advances and future perspectives, Bioact Mater 38 (2024) 346–373. https://doi.org/10.1016/j.bioactmat.2024.04.032.

[27] D. Gheorghiţă, H. Moldovan, A. Robu, A.I. Biţa, E. Grosu, A. Antoniac, I. Corneschi, I. Antoniac, A.D. Bodog, C.I. Băcilă, Chitosan-Based Biomaterials for Hemostatic Applications: A Review of Recent Advances, Int J Mol Sci 24 (2023). https://doi.org/10.3390/ijms241310540.

[28] G.I. Howling, P.W. Dettmar, P.A. Goddard, F.C. Hampson, M. Dornish, E.J. Wood, The e!ect of chitin and chitosan on the proliferation of human skin "broblasts and keratinocytes in vitro, 2001.

[29] M.M. Islam, M. Shahruzzaman, S. Biswas, M. Nurus Sakib, T.U. Rashid, Chitosan based bioactive materials in tissue engineering applications-A review, Bioact Mater 5 (2020) 164–183. https://doi.org/10.1016/j.bioactmat.2020.01.012.

[30] J. Lee, J. Hong, W.J. Kim, G.H. Kim, Bone-derived dECM/alginate bioink for fabricating a 3D cell-laden mesh structure for bone tissue engineering, Carbohydr Polym 250 (2020). https://doi.org/10.1016/j.carbpol.2020.116914.

[31] N. Kim, H. Lee, G. Han, M. Kang, S. Park, D.E. Kim, M. Lee, M.J. Kim, Y. Na, S.K. Oh, S.J. Bang, T.S. Jang, H.E. Kim, J. Park, S.R. Shin, H. Do Jung, 3D-Printed Functional Hydrogel by DNA-Induced Biomineralization for Accelerated Diabetic Wound Healing, Advanced Science 10 (2023). https://doi.org/10.1002/advs.202300816.

[32] C.H. Goh, P.W.S. Heng, L.W. Chan, Alginates as a useful natural polymer for microencapsulation and therapeutic applications, Carbohydr Polym 88 (2012) 1–12. https://doi.org/10.1016/j.carbpol.2011.11.012.

[33] Z. Li, H.R. Ramay, K.D. Hauch, D. Xiao, M. Zhang, Chitosan-alginate hybrid scaffolds for bone tissue engineering, Biomaterials 26 (2005) 3919–3928. https://doi.org/10.1016/j.biomaterials.2004.09.062.

[34] J. Li, S. Guan, J. Su, J. Liang, L. Cui, K. Zhang, The Development of Hyaluronic Acids Used for Skin Tissue Regeneration, Curr Drug Deliv 18 (2020) 836–846. https://doi.org/10.2174/1567201817666201202094513.

[35] H. Kim, H. Jeong, S. Han, S. Beack, B.W. Hwang, M. Shin, S.S. Oh, S.K. Hahn, Hyaluronate and its derivatives for customized biomedical applications, Biomaterials 123 (2017) 155–171. https://doi.org/10.1016/j.biomaterials.2017.01.029.

[36] S. Misra, P. Heldin, V.C. Hascall, N.K. Karamanos, S.S. Skandalis, R.R. Markwald, S. Ghatak, Hyaluronan-CD44 interactions as potential targets

for cancer therapy, FEBS Journal 278 (2011) 1429–1443. https://doi.org/10.1111/j.1742-4658.2011.08071.x.

[37] Y. He, Z. Hou, J. Wang, Z. Wang, X. Li, J. Liu, XiaolinYang, Q. Liang, J. Zhao, Assessment of biological properties of recombinant collagen-hyaluronic acid composite scaffolds, Int J Biol Macromol 149 (2020) 1275–1284. https://doi.org/10.1016/j.ijbiomac.2020.02.023.

[38] X. Yang, Y. Wang, Y. Zhou, J. Chen, Q. Wan, The application of polycaprolactone in three-dimensional printing scaffolds for bone tissue engineering, Polymers (Basel) 13 (2021). https://doi.org/10.3390/polym13162754.

[39] M. Gharibshahian, M. Salehi, N. Beheshtizadeh, M. Kamalabadi-Farahani, A. Atashi, M.S. Nourbakhsh, M. Alizadeh, Recent advances on 3D-printed PCL-based composite scaffolds for bone tissue engineering, Front Bioeng Biotechnol 11 (2023). https://doi.org/10.3389/fbioe.2023.1168504.

[40] B. Safari, M. Aghazadeh, L. Roshangar, A. Aghanejad, S. Davaran, A bioactive porous scaffold containing collagen/ phosphorous-modified polycaprolactone for osteogenesis of adipose-derived mesenchymal stem cells, Eur Polym J 171 (2022). https://doi.org/10.1016/j.eurpolymj.2022.111220.

[41] Q. Dong, M. Zhang, X. Zhou, Y. Shao, J. Li, L. Wang, C. Chu, F. Xue, Q. Yao, J. Bai, 3D-printed Mg-incorporated PCL-based scaffolds: A promising approach for bone healing, Materials Science and Engineering C 129 (2021). https://doi.org/10.1016/j.msec.2021.112372.

[42] H. Lee, D.S. Won, S. Park, Y. Park, J.W. Kim, G. Han, Y. Na, M.H. Kang, S.B. Kim, H. Kang, J.K. Park, T.S. Jang, S.J. Lee, S.A. Park, S.S. Lee, J.H. Park, H. Do Jung, 3D-printed versatile biliary stents with nanoengineered surface for anti-hyperplasia and antibiofilm formation, Bioact Mater 37 (2024) 172–190. https://doi.org/10.1016/j.bioactmat.2024.03.018.

[43] C. Garot, G. Bettega, C. Picart, Additive Manufacturing of Material Scaffolds for Bone Regeneration: Toward Application in the Clinics, Adv Funct Mater 31 (2021). https://doi.org/10.1002/adfm.202006967.

[44] P. Feng, J. Jia, M. Liu, S. Peng, Z. Zhao, C. Shuai, Degradation mechanisms and acceleration strategies of poly (lactic acid) scaffold for bone regeneration, Mater Des 210 (2021). https://doi.org/10.1016/j.matdes.2021.110066.

[45] B. Zhang, L. Wang, P. Song, X. Pei, H. Sun, L. Wu, C. Zhou, K. Wang, Y. Fan, X. Zhang, 3D printed bone tissue regenerative PLA/HA scaffolds with comprehensive performance optimizations, Mater Des 201 (2021) 109490. https://doi.org/10.1016/j.matdes.2021.109490.

[46] H. Lee, G. Han, Y. Na, M. Kang, S.J. Bang, H.S. Kang, T.S. Jang, J.H. Park, H.L. Jang, K. Yang, H. Kang, H. Do Jung, 3D-Printed Tissue-Specific Nanospike-Based Adhesive Materials for Time-Regulated Synergistic Tumor Therapy and Tissue Regeneration In Vivo, Adv Funct Mater (2024). https://doi.org/10.1002/adfm.202406237.

[47] Y.J. Low, A. Andriyana, B.C. Ang, N.I. Zainal Abidin, Bioresorbable and degradable behaviors of PGA: Current state and future prospects, Polym Eng Sci 60 (2020) 2657–2675. https://doi.org/10.1002/pen.25508.

[48] S.L.M. Dahl, A.P. Kypson, J.H. Lawson, J.L. Blum, J.T. Strader, Y. Li, R.J. Manson, W.E. Tente, L. DiBernardo, M.T. Hensley, R. Carter, T.P. Williams, H.L. Prichard, M.S. Dey, K.G. Begelman, L.E. Niklason, Readily Available Tissue-Engineered Vascular Grafts, Sci Transl Med 3 (2011) 68ra9-68ra9. https://doi.org/10.1126/scitranslmed.3001426.

[49] J. Zhang, B. Xie, Z. Xi, L. Zhao, L. Cen, Y. Yang, A comparable study of polyglycolic acid's degradation on macrophages' activation, Materials Science and Engineering C 109 (2020). https://doi.org/10.1016/j.msec.2019.110574.

[50] J. Li, C. Wang, G. Gao, X. Yin, X. Pu, B. Shi, Y. Liu, Z. Huang, J. Wang, J. Li, G. Yin, MBG/ PGA-PCL composite scaffolds provide highly tunable degradation and osteogenic features, Bioact Mater 15 (2022) 53–67. https://doi.org/10.1016/j.bioactmat.2021.11.034.

[51] N. Kohli, V. Sharma, S.J. Brown, E. García-Gareta, Synthetic polymers for skin biomaterials, in: Biomaterials for Skin Repair and Regeneration, Elsevier, 2019: pp. 125–149. https://doi.org/10.1016/B978-0-08-102546-8.00005-4.

[52] Y.C. Teo, A. Abbas, E.J. Park, C. Barbut, J. Guo, D. Goh, J.P.S. Yeong, W.L.J. Mok, P. Teo, 3D Printed Bioactive PLGA Dermal Scaffold for Burn Wound Treatment, ACS Materials Au 3 (2023) 265–272. https://doi.org/10.1021/acsmaterialsau.2c00079.

[53] Y. Tang, H. Wang, Y. Sun, Y. Jiang, S. Fang, Z. Kan, Y. Lu, S. Liu, X. Zhou, Z. Li, Using Platelet-Rich Plasma Hydrogel to Deliver Mesenchymal Stem

Cells into Three-Dimensional PLGA Scaffold for Cartilage Tissue Engineering, ACS Appl Bio Mater 4 (2021) 8607–8614. https://doi.org/10.1021/acsabm.1c01160.

[54] J. Babilotte, B. Martin, V. Guduric, R. Bareille, R. Agniel, S. Roques, V. Héroguez, M. Dussauze, M. Gaudon, D. Le Nihouannen, S. Catros, Development and characterization of a PLGA-HA composite material to fabricate 3D-printed scaffolds for bone tissue engineering, Materials Science and Engineering C 118 (2021). https://doi.org/10.1016/j.msec.2020.111334.

[55] E.J. Go, E.Y. Kang, S.K. Lee, S. Park, J.H. Kim, W. Park, I.H. Kim, B. Choi, D.K. Han, An osteoconductive PLGA scaffold with bioactive ß-TCP and anti-inflammatory Mg(OH)2 to improve: In vivo bone regeneration, Biomater Sci 8 (2020) 937–948. https://doi.org/10.1039/c9bm01864f.

[56] S. Barbon, M. Contran, E. Stocco, S. Todros, V. Macchi, R. De Caro, A. Porzionato, Enhanced biomechanical properties of polyvinyl alcohol-based hybrid scaffolds for cartilage tissue engineering, Processes 9 (2021). https://doi.org/10.3390/pr9050730.

[57] S. Mohanty, L.B. Larsen, J. Trifol, P. Szabo, H.V.R. Burri, C. Canali, M. Dufva, J. Emnéus, A. Wolff, Fabrication of scalable and structured tissue engineering scaffolds using water dissolvable sacrificial 3D printed moulds, Materials Science and Engineering C 55 (2015) 569–578. https://doi.org/10.1016/j.msec.2015.06.002.

[58] K. Kanimozhi, S. Khaleel Basha, V. Sugantha Kumari, Processing and characterization of chitosan/PVA and methylcellulose porous scaffolds for tissue engineering, Materials Science and Engineering C 61 (2016) 484–491. https://doi.org/10.1016/j.msec.2015.12.084.

[59] X. Yao, C. Qi, C. Sun, F. Huo, X. Jiang, Poly(ethylene glycol) alternatives in biomedical applications, Nano Today 48 (2023). https://doi.org/10.1016/j.nantod.2022.101738.

[60] M. Rajabi, J.D. Cabral, S. Saunderson, M. Gould, M.A. Ali, Development and optimisation of hydroxyapatite-polyethylene glycol diacrylate hydrogel inks for 3D printing of bone tissue engineered scaffolds, Biomed Mater 18 (2023). https://doi.org/10.1088/1748-605X/acf90a.

[61] S. Salehi, H. Ghomi, S.A. Hassanzadeh-Tabrizi, N. Koupaei, M. Khodaei, The effect of polyethylene glycol on printability, physical and mechanical

properties and osteogenic potential of 3D-printed poly (L-lactic acid)/polyethylene glycol scaffold for bone tissue engineering, Int J Biol Macromol 221 (2022) 1325–1334. https://doi.org/10.1016/j.ijbiomac.2022.09.027.

[62] J. Liang, Z. Guo, A. Timmerman, D. Grijpma, A. Poot, Enhanced mechanical and cell adhesive properties of photo-crosslinked PEG hydrogels by incorporation of gelatin in the networks, Biomedical Materials (Bristol) 14 (2019). https://doi.org/10.1088/1748-605X/aaf31b.

[63] S. Xiong, Materials, Application Status and Development Trends of Additive Manufacturing Technology, Mater Trans 61 (2020) 1191–1199. https://doi.org/10.2320/matertrans.MT-M2020023.

[64] A.M.E. Arefin, N.R. Khatri, N. Kulkarni, P.F. Egan, Polymer 3D Printing Review: Materials, Process, and Design Strategies for Medical Applications, Polymers (Basel) 13 (2021). https://doi.org/10.3390/polym13091499.

[65] S.C. Daminabo, S. Goel, S.A. Grammatikos, H.Y. Nezhad, V.K. Thakur, Fused deposition modeling-based additive manufacturing (3D printing): techniques for polymer material systems, Mater Today Chem 16 (2020). https://doi.org/10.1016/j.mtchem.2020.100248.

[66] G. Han, H. Lee, J.M. Kang, J.H. Park, E. Lee, E. Seong Lee, S. Park, Y. Na, M.H. Kang, N. Kim, S.J. Bang, K. Na, C.B. Yoon, S.K. Oh, B. Lei, J.D. Park, W. Park, H. Do Jung, 3D-printed NIR-responsive bullets as multifunctional nanodrug platforms for image-guided local chemo-photothermal therapy, Chemical Engineering Journal 477 (2023). https://doi.org/10.1016/j.cej.2023.147083.

[67] W. Wang, B. Zhang, M. Li, J. Li, C. Zhang, Y. Han, L. Wang, K. Wang, C. Zhou, L. Liu, Y. Fan, X. Zhang, 3D printing of PLA/n-HA composite scaffolds with customized mechanical properties and biological functions for bone tissue engineering, Compos B Eng 224 (2021) 109192. https://doi.org/https://doi.org/10.1016/j.compositesb.2021.109192.

[68] S. Radhakrishnan, S. Nagarajan, H. Belaid, C. Farha, I. Iatsunskyi, E. Coy, L. Soussan, V. Huon, J. Bares, K. Belkacemi, C. Teyssier, S. Balme, P. Miele, D. Cornu, N. Kalkura, V. Cavaillès, M. Bechelany, Fabrication of 3D printed antimicrobial polycaprolactone scaffolds for tissue engineering applications,

Materials Science and Engineering C 118 (2021). https://doi.org/10.1016/j.msec.2020.111525.

[69] K. Liu, L. Zhu, S. Tang, W. Wen, L. Lu, M. Liu, C. Zhou, B. Luo, Fabrication and evaluation of a chitin whisker/poly(l-lactide) composite scaffold by the direct trisolvent-ink writing method for bone tissue engineering, Nanoscale 12 (2020) 18225–18239. https://doi.org/10.1039/d0nr04204h.

[70] M.A.S.R. Saadi, A. Maguire, N.T. Pottackal, M.S.H. Thakur, M.Md. Ikram, A.J. Hart, P.M. Ajayan, M.M. Rahman, Direct Ink Writing: A 3D Printing Technology for Diverse Materials, Advanced Materials 34 (2022) 2108855. https://doi.org/https://doi.org/10.1002/adma.202108855.

[71] F. Chen, J. Han, Z. Guo, C. Mu, C. Yu, Z. Ji, L. Sun, Y. Wang, J. Wang, Antibacterial 3D-Printed Silver Nanoparticle/Poly Lactic-Co-Glycolic Acid (PLGA) Scaffolds for Bone Tissue Engineering, Materials 16 (2023). https://doi.org/10.3390/ma16113895.

[72] Z. Yahay, H. Tolabi, F. Delavar, S.A. Poursamar, S.M. Mirhadi, F. Tavangarian, Fabrication of meso/macroporous TiO2/PCL composite scaffolds by direct ink writing: The effects of porogen content on the compressive modulus and in vitro behavior, Mater Today Commun 35 (2023). https://doi.org/10.1016/j.mtcomm.2023.105769.

[73] Y. Li, X. Zhang, X. Zhang, Y. Zhang, D. Hou, Recent Progress of the Vat Photopolymerization Technique in Tissue Engineering: A Brief Review of Mechanisms, Methods, Materials, and Applications, Polymers (Basel) 15 (2023). https://doi.org/10.3390/polym15193940.

[74] C.A. Murphy, K.S. Lim, T.B.F. Woodfield, Next Evolution in Organ-Scale Biofabrication: Bioresin Design for Rapid High-Resolution Vat Polymerization, Advanced Materials 34 (2022). https://doi.org/10.1002/adma.202107759.

[75] L. Elomaa, E. Keshi, I.M. Sauer, M. Weinhart, Development of GelMA/PCL and dECM/PCL resins for 3D printing of acellular in vitro tissue scaffolds by stereolithography, Materials Science and Engineering C 112 (2020). https://doi.org/10.1016/j.msec.2020.110958.

[76] M. Zanon, D. Baruffaldi, M. Sangermano, C.F. Pirri, F. Frascella, A. Chiappone, Visible light-induced crosslinking of unmodified gelatin with

PEGDA for DLP-3D printable hydrogels, Eur Polym J 160 (2021). https://doi.org/10.1016/j.eurpolymj.2021.110813.

[77] E.M. Wilts, T.E. Long, Sustainable additive manufacturing: predicting binder jettability of water-soluble, biodegradable and recyclable polymers, Polym Int 70 (2021) 958–963. https://doi.org/10.1002/pi.6108.

[78] P. Szymczyk-Ziółkowska, M.B. Łabowska, J. Detyna, I. Michalak, P. Gruber, A review of fabrication polymer scaffolds for biomedical applications using additive manufacturing techniques, Biocybern Biomed Eng 40 (2020) 624–638. https://doi.org/10.1016/j.bbe.2020.01.015.

[79] J. Zhang, B.J. Allardyce, R. Rajkhowa, X. Wang, X. Liu, 3D printing of silk powder by Binder Jetting technique, Addit Manuf 38 (2021). https://doi.org/10.1016/j.addma.2020.101820.

[80] W. Huang, Q. Zheng, W. Sun, H. Xu, X. Yang, Levofloxacin implants with predefined microstructure fabricated by three-dimensional printing technique, Int J Pharm 339 (2007) 33–38. https://doi.org/10.1016/j.ijpharm.2007.02.021.

[81] R. Singh, A. Gupta, O. Tripathi, S. Srivastava, B. Singh, A. Awasthi, S.K. Rajput, P. Sonia, P. Singhal, K.K. Saxena, Powder bed fusion process in additive manufacturing: An overview, in: Mater Today Proc, Elsevier Ltd, 2019: pp. 3058–3070. https://doi.org/10.1016/j.matpr.2020.02.635.

[82] N.K. Roy, D. Behera, O.G. Dibua, C.S. Foong, M.A. Cullinan, A novel microscale selective laser sintering (μ-SLS) process for the fabrication of microelectronic parts, Microsyst Nanoeng 5 (2019). https://doi.org/10.1038/s41378-019-0116-8.

[83] W. Han, L. Kong, M. Xu, Advances in selective laser sintering of polymers, International Journal of Extreme Manufacturing 4 (2022). https://doi.org/10.1088/2631-7990/ac9096.

[84] X. Cui, J. Li, Y. Hartanto, M. Durham, J. Tang, H. Zhang, G. Hooper, K. Lim, T. Woodfield, Advances in Extrusion 3D Bioprinting: A Focus on Multicomponent Hydrogel-Based Bioinks, Adv Healthc Mater 9 (2020). https://doi.org/10.1002/adhm.201901648.

[85] S. V. Murphy, A. Atala, 3D bioprinting of tissues and organs, Nat Biotechnol 32 (2014) 773–785. https://doi.org/10.1038/nbt.2958.

[86] A. Lee, A.R. Hudson, D.J. Shiwarski, J.W. Tashman, T.J. Hinton, S. Yerneni, J.M. Bliley, P.G. Campbell, A.W. Feinberg, 3D bioprinting of collagen to rebuild components of the human heart, Science (1979) 365 (2019) 482–487. https://doi.org/10.1126/science.aav9051.

[87] K.C.R. Kolan, J.A. Semon, B. Bromet, D.E. Day, M.C. Leu, Bioprinting with human stem cell-laden alginate-gelatin bioink and bioactive glass for tissue engineering, Int J Bioprint 5 (2019) 3–15. https://doi.org/10.18063/ijb.v5i2.2.204.

[88] T. Agarwal, I. Chiesa, M. Costantini, A. Lopamarda, M.C. Tirelli, O.P. Borra, S.V.S. Varshapally, Y.A.V. Kumar, G. Koteswara Reddy, C. De Maria, L.G. Zhang, T.K. Maiti, Chitosan and its derivatives in 3D/4D (bio) printing for tissue engineering and drug delivery applications, Int J Biol Macromol 246 (2023). https://doi.org/10.1016/j.ijbiomac.2023.125669.

[89] Q. Mao, Y. Wang, Y. Li, S. Juengpanich, W. Li, M. Chen, J. Yin, J. Fu, X. Cai, Fabrication of liver microtissue with liver decellularized extracellular matrix (dECM) bioink by digital light processing (DLP) bioprinting, Materials Science and Engineering C 109 (2020). https://doi.org/10.1016/j.msec.2020.110625.

[90] J. Karvinen, M. Kellomäki, Design aspects and characterization of hydrogel-based bioinks for extrusion-based bioprinting, Bioprinting 32 (2023). https://doi.org/10.1016/j.bprint.2023.e00274.

[91] R.D. Ventura, An Overview of Laser-assisted Bioprinting (LAB) in Tissue Engineering Applications, Medical Lasers 10 (2021) 76–81. https://doi.org/10.25289/ml.2021.10.2.76.

[92] X. Yang, S. Li, Y. Ren, L. Qiang, Y. Liu, J. Wang, K. Dai, 3D printed hydrogel for articular cartilage regeneration, Compos B Eng 237 (2022). https://doi.org/10.1016/j.compositesb.2022.109863.

[93] H. Zhang, M. Wang, R. Wu, J. Guo, A. Sun, Z. Li, R. Ye, G. Xu, Y. Cheng, From materials to clinical use: advances in 3D-printed scaffolds for cartilage tissue engineering, Physical Chemistry Chemical Physics 25 (2023) 24244–24263. https://doi.org/10.1039/d3cp00921a.

[94] X. Gui, Z. Peng, P. Song, L. Chen, X. Xu, H. Li, P. Tang, Y. Wang, Z. Su, Q. Kong, Z. Zhang, Z. Li, Y. Cen, C. Zhou, Y. Fan, X. Zhang, 3D printing of personalized polylactic acid scaffold laden with GelMA/autologous auricle

cartilage to promote ear reconstruction, Biodes Manuf 6 (2023) 451–463. https://doi.org/10.1007/s42242-023-00242-6.

[95] C.H. Chen, V.B.H. Shyu, J.P. Chen, M.Y. Lee, Selective laser sintered poly-ε-caprolactone scaffold hybridized with collagen hydrogel for cartilage tissue engineering, Biofabrication 6 (2014). https://doi.org/10.1088/1758-5082/6/1/015004.

[96] S.A. Schoonraad, K.M. Fischenich, K.N. Eckstein, V. Crespo-Cuevas, L.M. Savard, A. Muralidharan, A.A. Tomaschke, A.C. Uzcategui, M.A. Randolph, R.R. McLeod, V.L. Ferguson, S.J. Bryant, Biomimetic and mechanically supportive 3D printed scaffolds for cartilage and osteochondral tissue engineering using photopolymers and digital light processing, Biofabrication 13 (2021). https://doi.org/10.1088/1758-5090/ac23ab.

[97] Y. Cao, P. Cheng, S. Sang, C. Xiang, Y. An, X. Wei, Y. Yan, P. Li, 3D printed PCL/GelMA biphasic scaffold boosts cartilage regeneration using co-culture of mesenchymal stem cells and chondrocytes: In vivo study, Mater Des 210 (2021). https://doi.org/10.1016/j.matdes.2021.110065.

[98] A. Maihemuti, H. Zhang, X. Lin, Y. Wang, Z. Xu, D. Zhang, Q. Jiang, 3D-printed fish gelatin scaffolds for cartilage tissue engineering, Bioact Mater 26 (2023) 77–87. https://doi.org/10.1016/j.bioactmat.2023.02.007.

[99] M. Ding, C.C. Danielsen, I. Hvid, Bone density does not reflect mechanical properties in early-stage arthrosis, Acta Orthop 72 (2001) 181–185. https://doi.org/10.1080/000164701317323444.

[100] Z. Xu, Y. Zhang, Y. Wu, Z. Zhang, D. Jiang, R. Jia, X. Wang, Z. Liu, In Vitro and in Vivo Analysis of the Effects of 3D-Printed Porous Titanium Alloy Scaffold Structure on Osteogenic Activity, Biomed Res Int 2022 (2022). https://doi.org/10.1155/2022/8494431.

[101] A.R. Amini, C.T. Laurencin, S.P. Nukavarapu, Bone Tissue Engineering: Recent Advances and Challenges, Critical Reviews™ in Biomedical Engineering 40 (2012) 363–408.

[102] M. Mirkhalaf, Y. Men, R. Wang, Y. No, H. Zreiqat, Personalized 3D printed bone scaffolds: A review, Acta Biomater 156 (2023) 110–124. https://doi.org/10.1016/j.actbio.2022.04.014.

[103] A. Zimmerling, Z. Yazdanpanah, D.M.L. Cooper, J.D. Johnston, X. Chen, 3D printing PCL/nHA bone scaffolds: exploring the influence of material

synthesis techniques, Biomater Res 25 (2021). https://doi.org/10.1186/s40824-021-00204-y.

[104] R. Dong, M. Kang, Y. Qu, T. Hou, J. Zhao, X. Cheng, Incorporating Hydrogel (with Low Polymeric Content) into 3D-Printed PLGA Scaffolds for Local and Sustained Release of BMP2 in Repairing Large Segmental Bone Defects, Adv Healthc Mater (2024). https://doi.org/10.1002/adhm.202403613.

[105] J. Shen, W. Wang, X. Zhai, B. Chen, W. Qiao, W. Li, P. Li, Y. Zhao, Y. Meng, S. Qian, X. Liu, P.K. Chu, K.W.K. Yeung, 3D-printed nanocomposite scaffolds with tunable magnesium ionic microenvironment induce in situ bone tissue regeneration, Appl Mater Today 16 (2019) 493–507. https://doi.org/10.1016/j.apmt.2019.07.012.

[106] M. Cha, Y.Z. Jin, J.W. Park, K.M. Lee, S.H. Han, B.S. Choi, J.H. Lee, Three-dimensional printed polylactic acid scaffold integrated with BMP-2 laden hydrogel for precise bone regeneration, Biomater Res 25 (2021). https://doi.org/10.1186/s40824-021-00233-7.

[107] D. Lei, Y. Yang, Z. Liu, S. Chen, B. Song, A. Shen, B. Yang, S. Li, Z. Yuan, Q. Qi, L. Sun, Y. Guo, H. Zuo, S. Huang, Q. Yang, X. Mo, C. He, B. Zhu, E.M. Jeffries, F.L. Qing, X. Ye, Q. Zhao, Z. You, A general strategy of 3D printing thermosets for diverse applications, Mater Horiz 6 (2019) 394–404. https://doi.org/10.1039/c8mh00937f.

[108] Y. Wang, G.A. Ameer, B.J. Sheppard, R. Langer, A tough biodegradable elastomer, 2002. http://biotech.nature.com.

[109] G. Yin, D. Zhao, X. Wang, Y. Ren, L. Zhang, X. Wu, S. Nie, Q. Li, Bio-compatible poly(ester-urethane)s based on PEG-PCL-PLLA copolymer with tunable crystallization and bio-degradation properties, RSC Adv 5 (2015) 79070–79080. https://doi.org/10.1039/c5ra15531b.

[110] C. Intini, M. Lemoine, T. Hodgkinson, S. Casey, J.P. Gleeson, F.J. O'Brien, A highly porous type II collagen containing scaffold for the treatment of cartilage defects enhances MSC chondrogenesis and early cartilaginous matrix deposition, Biomater Sci 10 (2022) 970–983. https://doi.org/10.1039/d1bm01417j.

[111] M.G. Haugh, C.M. Murphy, F.J. O'Brien, Novel Freeze-Drying Methods to Produce a Range of Collagen–Glycosaminoglycan Scaffolds with Tailored

Mean Pore Sizes, Tissue Eng Part C Methods 16 (2009) 887–894. https://doi.org/10.1089/ten.tec.2009.0422.

[112] G.M. Cunniffe, C.M. Curtin, E.M. Thompson, G.R. Dickson, F.J. O'Brien, Content-Dependent Osteogenic Response of Nanohydroxyapatite: An in Vitro and in Vivo Assessment within Collagen-Based Scaffolds, ACS Appl Mater Interfaces 8 (2016) 23477–23488. https://doi.org/10.1021/acsami.6b06596.

[113] I.S.O., Implants for surgery-Homopolymers, copolymers and blends on poly(lactide)-In vitro degradation testing, (2017). https://www.iso.org/standard/64565.html.

[114] C. Thompson, G. Domínguez, P. Bardisa, Y. Liu, J.P. Fernández-Blázquez, J.S. del Río, M. Echeverry-Rendon, C. González, J. Llorca, Medical grade 3D printable bioabsorbable PLDL/Mg and PLDL/Zn composites for biomedical applications, J Biomed Mater Res A 112 (2024) 798–811. https://doi.org/10.1002/jbm.a.37660.

[115] R.M. Raftery, E.G. Tierney, C.M. Curtin, S.A. Cryan, F.J. O'Brien, Development of a gene-activated scaffold platform for tissue engineering applications using chitosan-pDNA nanoparticles on collagen-based scaffolds, Journal of Controlled Release 210 (2015) 84–94. https://doi.org/10.1016/j.jconrel.2015.05.005.

[116] R.M. Raftery, I. Mencía Castaño, G. Chen, B. Cavanagh, B. Quinn, C.M. Curtin, S.A. Cryan, F.J. O'Brien, Translating the role of osteogenic-angiogenic coupling in bone formation: Highly efficient chitosan-pDNA activated scaffolds can accelerate bone regeneration in critical-sized bone defects, Biomaterials 149 (2017) 116–127. https://doi.org/10.1016/j.biomaterials.2017.09.036.

[117] C. Intini, L.B. Ferreras, S. Casey, J.E. Dixon, J.P. Gleeson, F.J. O'Brien, An Innovative miR-Activated Scaffold for the Delivery of a miR-221 Inhibitor to Enhance Cartilage Defect Repair, Adv Ther (Weinh) 6 (2023). https://doi.org/10.1002/adtp.202200329.

[118] X. Zhang, Z. Li, P. Yang, G. Duan, X. Liu, Z. Gu, Y. Li, Polyphenol scaffolds in tissue engineering, Mater Horiz 8 (2021) 145–167. https://doi.org/10.1039/d0mh01317j.

[119] J. Malda, J. Visser, F.P. Melchels, T. Jüngst, W.E. Hennink, W.J.A. Dhert, J. Groll, D.W. Hutmacher, 25th anniversary article: Engineering hydrogels for biofabrication, Advanced Materials 25 (2013) 5011–5028. https://doi.org/10.1002/adma.201302042.

[120] B.D. Ulery, L.S. Nair, C.T. Laurencin, Biomedical applications of biodegradable polymers, J Polym Sci B Polym Phys 49 (2011) 832–864. https://doi.org/10.1002/polb.22259.

[121] S.H. Hsu, K.C. Hung, C.W. Chen, Biodegradable polymer scaffolds, J Mater Chem B 4 (2016) 7493–7505. https://doi.org/10.1039/c6tb02176j.

[122] C. Ning, P. Li, C. Gao, L. Fu, Z. Liao, G. Tian, H. Yin, M. Li, X. Sui, Z. Yuan, S. Liu, Q. Guo, Recent advances in tendon tissue engineering strategy, Front Bioeng Biotechnol 11 (2023). https://doi.org/10.3389/fbioe.2023.1115312.

[123] M. Gasik, A. Zühlke, A.M. Haaparanta, V. Muhonen, K. Laine, Y. Bilotsky, M. Kellomäki, I. Kiviranta, The importance of controlled mismatch of biomechanical compliances of implantable scaffolds and native tissue for articular cartilage regeneration, Front Bioeng Biotechnol 6 (2018). https://doi.org/10.3389/fbioe.2018.00187.

[124] B.S. Heidari, P. Chen, R. Ruan, S.M. Davachi, H. Al-Salami, E. De Juan Pardo, M. Zheng, B. Doyle, B.S. Heidari, A novel biocompatible polymeric blend for applications requiring high toughness and tailored degradation rate, J Mater Chem B 9 (2021) 2532–2546. https://doi.org/10.1039/d0tb02971h.

[125] E.J. Go, E.Y. Kang, S.K. Lee, S. Park, J.H. Kim, W. Park, I.H. Kim, B. Choi, D.K. Han, An osteoconductive PLGA scaffold with bioactive β-TCP and anti-inflammatory Mg(OH)2 to improve: In vivo bone regeneration, Biomater Sci 8 (2020) 937–948. https://doi.org/10.1039/c9bm01864f.

[126] H. Ben Amara, D.C. Martinez, F.A. Shah, A.J. Loo, L. Emanuelsson, B. Norlindh, R. Willumeit-Römer, T. Plocinski, W. Swieszkowski, A. Palmquist, O. Omar, P. Thomsen, Magnesium implant degradation provides immunomodulatory and proangiogenic effects and attenuates peri-implant fibrosis in soft tissues, Bioact Mater 26 (2023) 353–369. https://doi.org/10.1016/j.bioactmat.2023.02.014.

[127] L. Zhao, X. Pei, L. Jiang, C. Hu, J. Sun, F. Xing, C. Zhou, Y. Fan, X. Zhang, Bionic design and 3D printing of porous titanium alloy scaffolds for bone

tissue repair, Compos B Eng 162 (2019) 154–161. https://doi.org/10.1016/j.compositesb.2018.10.094.

[128] Z.U. Arif, M.Y. Khalid, R. Noroozi, A. Sadeghianmaryan, M. Jalalvand, M. Hossain, Recent advances in 3D-printed polylactide and polycaprolactone-based biomaterials for tissue engineering applications, Int J Biol Macromol 218 (2022) 930–968. https://doi.org/https://doi.org/10.1016/j.ijbiomac.2022.07.140.

[129] H. Ma, C. Feng, J. Chang, C. Wu, 3D-printed bioceramic scaffolds: From bone tissue engineering to tumor therapy, Acta Biomater 79 (2018) 37–59. https://doi.org/10.1016/j.actbio.2018.08.026.

[130] A.V. Do, B. Khorsand, S.M. Geary, A.K. Salem, 3D Printing of Scaffolds for Tissue Regeneration Applications, Adv Healthc Mater 4 (2015) 1742–1762. https://doi.org/10.1002/adhm.201500168.

[131] A. Kirillova, T.R. Yeazel, D. Asheghali, S.R. Petersen, S. Dort, K. Gall, M.L. Becker, Fabrication of Biomedical Scaffolds Using Biodegradable Polymers, Chem Rev 121 (2021) 11238–11304. https://doi.org/10.1021/acs.chemrev.0c01200.

[132] A.V. Do, B. Khorsand, S.M. Geary, A.K. Salem, 3D Printing of Scaffolds for Tissue Regeneration Applications, Adv Healthc Mater 4 (2015) 1742–1762. https://doi.org/10.1002/adhm.201500168.

[133] J. Zhang, D. Tong, H. Song, R. Ruan, Y. Sun, Y. Lin, J. Wang, L. Hou, J. Dai, J. Ding, H. Yang, Osteoimmunity-Regulating Biomimetically Hierarchical Scaffold for Augmented Bone Regeneration, Advanced Materials 34 (2022). https://doi.org/10.1002/adma.202202044.

[134] C. Wang, W. Huang, Y. Zhou, L. He, Z. He, Z. Chen, X. He, S. Tian, J. Liao, B. Lu, Y. Wei, M. Wang, 3D printing of bone tissue engineering scaffolds, Bioact Mater 5 (2020) 82–91. https://doi.org/10.1016/j.bioactmat.2020.01.004.

[135] S.C. Daminabo, S. Goel, S.A. Grammatikos, H.Y. Nezhad, V.K. Thakur, Fused deposition modeling-based additive manufacturing (3D printing): techniques for polymer material systems, Mater Today Chem 16 (2020). https://doi.org/10.1016/j.mtchem.2020.100248.

[136] S.C. Altıparmak, V.A. Yardley, Z. Shi, J. Lin, Extrusion-based additive manufacturing technologies: State of the art and future perspectives, J

Manuf Process 83 (2022) 607–636. https://doi.org/10.1016/j.jmapro.2022.09.032.

[137] B. Guo, P.X. Ma, Synthetic biodegradable functional polymers for tissue engineering: A brief review, Sci China Chem 57 (2014) 490–500. https://doi.org/10.1007/s11426-014-5086-y.

[138] C. Xu, Y. Hong, Rational design of biodegradable thermoplastic polyurethanes for tissue repair, Bioact Mater 15 (2022) 250–271. https://doi.org/10.1016/j.bioactmat.2021.11.029.

[139] X. Liu, J.M. Holzwarth, P.X. Ma, Functionalized Synthetic Biodegradable Polymer Scaffolds for Tissue Engineering, Macromol Biosci 12 (2012) 911–919. https://doi.org/10.1002/mabi.201100466.

[140] J. Kundu, F. Pati, Y. Hun Jeong, D.W. Cho, Biomaterials for Biofabrication of 3D Tissue Scaffolds, in: Biofabrication: Micro- and Nano-Fabrication, Printing, Patterning and Assemblies, Elsevier Inc., 2013: pp. 23–46. https://doi.org/10.1016/B978-1-4557-2852-7.00002-0.

[141] S. Stratton, N.B. Shelke, K. Hoshino, S. Rudraiah, S.G. Kumbar, Bioactive polymeric scaffolds for tissue engineering, Bioact Mater 1 (2016) 93–108. https://doi.org/10.1016/j.bioactmat.2016.11.001.

[142] D. Zhao, T. Zhu, J. Li, L. Cui, Z. Zhang, X. Zhuang, J. Ding, Poly(lactic-co-glycolic acid)-based composite bone-substitute materials, Bioact Mater 6 (2021) 346–360. https://doi.org/10.1016/j.bioactmat.2020.08.016.

[143] Y. Hou, W. Wang, P. Bartolo, Investigation of polycaprolactone for bone tissue engineering scaffolds: In vitro degradation and biological studies, Mater Des 216 (2022). https://doi.org/10.1016/j.matdes.2022.110582.

[144] S. Vijayavenkataraman, S. Thaharah, S. Zhang, W.F. Lu, J.Y.H. Fuh, Electrohydrodynamic jet 3D-printed PCL/PAA conductive scaffolds with tunable biodegradability as nerve guide conduits (NGCs) for peripheral nerve injury repair, Mater Des 162 (2019) 171–184. https://doi.org/10.1016/j.matdes.2018.11.044.

[145] S. Wang, R. Gu, F. Wang, X. Zhao, F. Yang, Y. Xu, F. Yan, Y. Zhu, D. Xia, Y. Liu, 3D-Printed PCL/Zn scaffolds for bone regeneration with a dose-dependent effect on osteogenesis and osteoclastogenesis, Mater Today Bio 13 (2022). https://doi.org/10.1016/j.mtbio.2021.100202.

[146] S. Murab, S.M.S. Gruber, C.Y.J. Lin, P. Whitlock, Elucidation of bio-inspired hydroxyapatie crystallization on oxygen-plasma modified 3D printed poly-caprolactone scaffolds, Materials Science and Engineering C 109 (2020). https://doi.org/10.1016/j.msec.2019.110529.

[147] Q. Dong, M. Zhang, X. Zhou, Y. Shao, J. Li, L. Wang, C. Chu, F. Xue, Q. Yao, J. Bai, 3D-printed Mg-incorporated PCL-based scaffolds: A promising approach for bone healing, Materials Science and Engineering C 129 (2021). https://doi.org/10.1016/j.msec.2021.112372.

[148] C. Vyas, J. Zhang, Ø. Øvrebø, B. Huang, I. Roberts, M. Setty, B. Allardyce, H. Haugen, R. Rajkhowa, P. Bartolo, 3D printing of silk microparticle reinforced polycaprolactone scaffolds for tissue engineering applications, Materials Science and Engineering C 118 (2021). https://doi.org/10.1016/j.msec.2020.111433.

[149] H. Ehtesabi, F. Massah, Improvement of hydrophilicity and cell attachment of polycaprolactone scaffolds using green synthesized carbon dots, Materials Today Sustainability 13 (2021). https://doi.org/10.1016/j.mtsust.2021.100075.

[150] H. Maleki-Ghaleh, M. Hossein Siadati, A. Fallah, A. Zarrabi, F. Afghah, B. Koc, E. Dalir Abdolahinia, Y. Omidi, J. Barar, A. Akbari-Fakhrabadi, Y. Beygi-Khosrowshahi, K. Adibkia, Effect of zinc-doped hydroxyapatite/graphene nanocomposite on the physicochemical properties and osteogenesis differentiation of 3D-printed polycaprolactone scaffolds for bone tissue engineering, Chemical Engineering Journal 426 (2021). https://doi.org/10.1016/j.cej.2021.131321.

[151] C. Cao, P. Huang, A. Prasopthum, A.J. Parsons, F. Ai, J. Yang, Characterisation of bone regeneration in 3D printed ductile PCL/PEG/hydroxyapatite scaffolds with high ceramic microparticle concentrations, Biomater Sci 10 (2022) 138–152. https://doi.org/10.1039/d1bm01645h.

[152] P.Y. Ni, Q.X. Ding, M. Fan, J.F. Liao, Z.Y. Qian, J.C. Luo, X.Q. Li, F. Luo, Z.M. Yang, Y.Q. Wei, Injectable thermosensitive PEG-PCL-PEG hydrogel/acellular bone matrix composite for bone regeneration in cranial defects, Biomaterials 35 (2014) 236–248. https://doi.org/10.1016/j.biomaterials.2013.10.016.

[153] C.P. Jiang, J.R. Huang, M.F. Hsieh, Fabrication of synthesized PCL-PEG-PCL tissue engineering scaffolds using an air pressure-aided deposition system, Rapid Prototyp J 17 (2011) 288–297. https://doi.org/10.1108/13552541111138414.

[154] N. Fu, J. Liao, S. Lin, K. Sun, T. Tian, B. Zhu, Y. Lin, PCL-PEG-PCL film promotes cartilage regeneration in vivo, Cell Prolif 49 (2016) 729–739. https://doi.org/10.1111/cpr.12295.

[155] M. Nagata, I. Kitazima, Photocurable biodegradable poly(ε-caprolactone)/poly(ethylene glycol) multiblock copolymers showing shape-memory properties, Colloid Polym Sci 284 (2006) 380–386. https://doi.org/10.1007/s00396-005-1393-3.

[156] J.Z. Bei, J.M. Li, Z.F. Wang, J.C. Le, S.G. Wang, Polycaprolactone-poly(ethylene-glycol) block copolymer. IV: Biodegradation behavior in vitro and in vivo, Polym Adv Technol 8 (1997) 693–696. https://doi.org/10.1002/(SICI)1099-1581(199711)8:11<693::AID-PAT702>3.0.CO;2-B.

[157] J. Sun, J. Yang, J. Ding, Controlled Synthesis of Polymers†, Chin J Chem 41 (2023) 1235–1248. https://doi.org/10.1002/cjoc.202200850.

[158] R. Il Kim, G. Lee, J.H. Lee, J.J. Park, A.S. Lee, S.S. Hwang, Structure-Property Relationships of 3D-Printable Chain-Extended Block Copolymers with Tunable Elasticity and Biodegradability, ACS Appl Polym Mater 3 (2021) 4708–4716. https://doi.org/10.1021/acsapm.1c00860.

[159] Y. Huang, L. Li, G. Li, An enzyme-catalysed access to amphiphilic triblock copolymer of PCL-b-PEG-b-PCL: synthesis, characterization and self-assembly properties, Des Monomers Polym 18 (2015) 799–806. https://doi.org/10.1080/15685551.2015.1078113.

[160] K.C. Ang, K.F. Leong, C.K. Chua, M. Chandrasekaran, Compressive properties and degradability of poly(ε-caprolatone)/ hydroxyapatite composites under accelerated hydrolytic degradation, J Biomed Mater Res A 80 (2007) 655–660. https://doi.org/10.1002/jbm.a.30996.

[161] M. Bartnikowski, T.R. Dargaville, S. Ivanovski, D.W. Hutmacher, Degradation mechanisms of polycaprolactone in the context of chemistry, geometry and environment, Prog Polym Sci 96 (2019) 1–20. https://doi.org/10.1016/j.progpolymsci.2019.05.004.

[162] F. Von Burkersroda, L. Schedl, A.G. Opferich, Why degradable polymers undergo surface erosion or bulk erosion, 2002.

[163] X. Yan, B. Yang, Y. Chen, Y. Song, J. Ye, Y. Pan, B. Zhou, Y. Wang, F. Mao, Y. Dong, D. Liu, J. Yu, Anti-Friction MSCs Delivery System Improves the Therapy for Severe Osteoarthritis, Advanced Materials 33 (2021). https://doi.org/10.1002/adma.202104758.

[164] M.K. Mamidi, A.K. Das, Z. Zakaria, R. Bhonde, Mesenchymal stromal cells for cartilage repair in osteoarthritis, Osteoarthritis Cartilage 24 (2016) 1307–1316. https://doi.org/10.1016/j.joca.2016.03.003.

[165] S. Camarero-Espinosa, B. Rothen-Rutishauser, E.J. Foster, C. Weder, Articular cartilage: From formation to tissue engineering, Biomater Sci 4 (2016) 734–767. https://doi.org/10.1039/c6bm00068a.

[166] Z.H. Deng, Y.S. Li, X. Gao, G.H. Lei, J. Huard, Bone morphogenetic proteins for articular cartilage regeneration, Osteoarthritis Cartilage 26 (2018) 1153–1161. https://doi.org/10.1016/j.joca.2018.03.007.

[167] J.M. Patel, K.S. Saleh, J.A. Burdick, R.L. Mauck, Bioactive factors for cartilage repair and regeneration: Improving delivery, retention, and activity, Acta Biomater 93 (2019) 222–238. https://doi.org/10.1016/j.actbio.2019.01.061.

[168] D. Gonzalez-Rodriguez, K. Guevorkian, S. Douezan, F. Brochard-Wyart, Soft matter models of developing tissues and tumors, Science (1979) 338 (2012) 910–917. https://doi.org/10.1126/science.1226418.

[169] X. Nie, Y.J. Chuah, W. Zhu, P. He, Y. Peck, D.A. Wang, Decellularized tissue engineered hyaline cartilage graft for articular cartilage repair, Biomaterials 235 (2020). https://doi.org/10.1016/j.biomaterials.2020.119821.

[170] F. Migliorini, N. Maffulli, A. Baroncini, J. Eschweiler, M. Knobe, M. Tingart, H. Schenker, Allograft Versus Autograft Osteochondral Transplant for Chondral Defects of the Talus: Systematic Review and Meta-analysis, American Journal of Sports Medicine 50 (2022) 3447–3455. https://doi.org/10.1177/03635465211037349.

[171] A. Maihemuti, H. Zhang, X. Lin, Y. Wang, Z. Xu, D. Zhang, Q. Jiang, 3D-printed fish gelatin scaffolds for cartilage tissue engineering, Bioact Mater 26 (2023) 77–87. https://doi.org/10.1016/j.bioactmat.2023.02.007.

[172] P. Li, L. Fu, Z. Liao, Y. Peng, C. Ning, C. Gao, D. Zhang, X. Sui, Y. Lin, S. Liu, C. Hao, Q. Guo, Chitosan hydrogel/3D-printed poly(ε-caprolactone) hybrid scaffold containing synovial mesenchymal stem cells for cartilage regeneration based on tetrahedral framework nucleic acid recruitment, Biomaterials 278 (2021). https://doi.org/10.1016/j.biomaterials.2021.121131.

[173] W. Wei, H. Dai, Articular cartilage and osteochondral tissue engineering techniques: Recent advances and challenges, Bioact Mater 6 (2021) 4830–4855. https://doi.org/10.1016/j.bioactmat.2021.05.011.

[174] S. Wang, S. Zhao, J. Yu, Z. Gu, Y. Zhang, Advances in Translational 3D Printing for Cartilage, Bone, and Osteochondral Tissue Engineering, Small 18 (2022). https://doi.org/10.1002/smll.202201869.

[175] B.A.G. de Melo, Y.A. Jodat, S. Mehrotra, M.A. Calabrese, T. Kamperman, B.B. Mandal, M.H.A. Santana, E. Alsberg, J. Leijten, S.R. Shin, 3D Printed Cartilage-Like Tissue Constructs with Spatially Controlled Mechanical Properties, Adv Funct Mater 29 (2019). https://doi.org/10.1002/adfm.201906330.

[176] Y.Y. Liu, J.P.F. Blazquez, G.Z. Yin, D.Y. Wang, J. Llorca, M. Echeverry-Rendón, A strategy to tailor the mechanical and degradation properties of PCL-PEG-PCL based copolymers for biomedical application, Eur Polym J 198 (2023). https://doi.org/10.1016/j.eurpolymj.2023.112388.

[177] Y. Cao, P. Cheng, S. Sang, C. Xiang, Y. An, X. Wei, Y. Yan, P. Li, 3D printed PCL/GelMA biphasic scaffold boosts cartilage regeneration using co-culture of mesenchymal stem cells and chondrocytes: In vivo study, Mater Des 210 (2021). https://doi.org/10.1016/j.matdes.2021.110065.

[178] Y. Tang, H. Wang, Y. Sun, Y. Jiang, S. Fang, Z. Kan, Y. Lu, S. Liu, X. Zhou, Z. Li, Using Platelet-Rich Plasma Hydrogel to Deliver Mesenchymal Stem Cells into Three-Dimensional PLGA Scaffold for Cartilage Tissue Engineering, ACS Appl Bio Mater 4 (2021) 8607–8614. https://doi.org/10.1021/acsabm.1c01160.

[179] L. Vogt, F. Ruther, S. Salehi, A.R. Boccaccini, Poly(Glycerol Sebacate) in Biomedical Applications—A Review of the Recent Literature, Adv Healthc Mater 10 (2021). https://doi.org/10.1002/adhm.202002026.

[180] S. Huang, D. Lei, Q. Yang, Y. Yang, C. Jiang, H. Shi, B. Qian, Q. Long, W. Chen, Y. Chen, L. Zhu, W. Yang, L. Wang, W. Hai, Q. Zhao, Z. You, X. Ye, A

perfusable, multifunctional epicardial device improves cardiac function and tissue repair, Nat Med 27 (2021) 480–490. https://doi.org/10.1038/s41591-021-01279-9.

[181] Y. Yang, D. Lei, S. Huang, Q. Yang, B. Song, Y. Guo, A. Shen, Z. Yuan, S. Li, F.L. Qing, X. Ye, Z. You, Q. Zhao, Elastic 3D-Printed Hybrid Polymeric Scaffold Improves Cardiac Remodeling after Myocardial Infarction, Adv Healthc Mater 8 (2019). https://doi.org/10.1002/adhm.201900065.

[182] S. Wang, H. Chen, J. Huang, S. Shen, Z. Tang, X. Tan, D. Lei, G. Zhou, Gelatin-modified 3D printed PGS elastic hierarchical porous scaffold for cartilage regeneration, APL Bioeng 7 (2023). https://doi.org/10.1063/5.0152151.

[183] S. Wang, B. Luo, B. Bai, Q. Wang, H. Chen, X. Tan, Z. Tang, S. Shen, H. Zhou, Z. You, G. Zhou, D. Lei, 3D Printed Chondrogenic Functionalized PGS Bioactive Scaffold for Cartilage Regeneration, Adv Healthc Mater 12 (2023). https://doi.org/10.1002/adhm.202301006.

[184] M. Chen, Y.Y. Li, S. Liu, Z. Feng, H. Wang, D. Yang, W. Guo, Z. Yuan, S. Gao, Y. Zhang, K. Zha, B. Huang, F. Wei, X. Sang, Q. Tian, X. Yang, X. sui, Y. Zhou, Y. Zheng, Q. Guo, Hierarchical macro-microporous WPU-ECM scaffolds combined with Microfracture Promote in Situ Articular Cartilage Regeneration in Rabbits, Bioact Mater 6 (2021) 1932–1944. https://doi.org/10.1016/j.bioactmat.2020.12.009.

[185] Z. Yang, T. Zhao, C. Gao, F. Cao, H. Li, Z. Liao, L. Fu, P. Li, W. Chen, Z. Sun, S. Jiang, Z. Tian, G. Tian, K. Zha, T. Pan, X. Li, X. Sui, Z. Yuan, S. Liu, Q. Guo, 3D-Bioprinted Difunctional Scaffold for in Situ Cartilage Regeneration Based on Aptamer-Directed Cell Recruitment and Growth Factor-Enhanced Cell Chondrogenesis, ACS Appl Mater Interfaces 13 (2021) 23369–23383. https://doi.org/10.1021/acsami.1c01844.

[186] M. Joyce, T. Hodgkinson, C. Intini, J. Dixon, D. Kelly, F. O'Brien, Gene activated reinforced scaffolds for SOX9 delivery to enhance repair of large load bearing articular cartilage defects, Eur Cell Mater 47 (2024) 91–108. https://doi.org/10.22203/ecm.v047a07.

[187] P. Salahshour, NANOBIOMATERIALS/BIOINKS BASED SCAFFOLDS IN 3D BIOPRINTING FOR TISSUE ENGINEERING AND ARTIFICIAL

HUMAN ORGANS, Advances in Biology & Earth Sciences 9 (2024) 97–104. https://doi.org/10.62476/abes9s97.

[188] F. Zhang, M.W. King, Biodegradable Polymers as the Pivotal Player in the Design of Tissue Engineering Scaffolds, Adv Healthc Mater 9 (2020). https://doi.org/10.1002/adhm.201901358.

[189] T.J. Levingstone, A. Matsiko, G.R. Dickson, F.J. O'Brien, J.P. Gleeson, A biomimetic multi-layered collagen-based scaffold for osteochondral repair, Acta Biomater 10 (2014) 1996–2004. https://doi.org/10.1016/j.actbio.2014.01.005.

[190] E. Ahmadian, A. Eftekhari, D. Janas, P. Vahedi, Nanofiber scaffolds based on extracellular matrix for articular cartilage engineering: A perspective, Nanotheranostics 7 (2023) 61–69. https://doi.org/10.7150/ntno.78611.

[191] C. Intini, T. Hodgkinson, S.M. Casey, J.P. Gleeson, F.J. O'brien, Highly Porous Type II Collagen-Containing Scaffolds for Enhanced Cartilage Repair with Reduced Hypertrophic Cartilage Formation, Bioengineering 9 (2022). https://doi.org/10.3390/bioengineering9060232.

[192] T.J. Levingstone, E. Thompson, A. Matsiko, A. Schepens, J.P. Gleeson, F.J. O'brien, Multi-layered collagen-based scaffolds for osteochondral defect repair in rabbits, Acta Biomater 32 (2016) 149–160. https://doi.org/10.1016/j.actbio.2015.12.034.

[193] T.J. Levingstone, A. Ramesh, R.T. Brady, P.A.J. Brama, C. Kearney, J.P. Gleeson, F.J. O'Brien, Cell-free multi-layered collagen-based scaffolds demonstrate layer specific regeneration of functional osteochondral tissue in caprine joints, Biomaterials 87 (2016) 69–81. https://doi.org/10.1016/j.biomaterials.2016.02.006.

[194] J.D. Stack, T.J. Levingstone, W. Lalor, R. Sanders, C. Kearney, F.J. O'Brien, F. David, Repair of large osteochondritis dissecans lesions using a novel multilayered tissue engineered construct in an equine athlete, J Tissue Eng Regen Med 11 (2017) 2785–2795. https://doi.org/https://doi.org/10.1002/term.2173.

[195] C.M. Murphy, M.G. Haugh, F.J. O'Brien, The effect of mean pore size on cell attachment, proliferation and migration in collagen-glycosaminoglycan scaffolds for bone tissue engineering, Biomaterials 31 (2010) 461–466. https://doi.org/10.1016/j.biomaterials.2009.09.063.

[196] H. Chen, G. Gonnella, J. Huang, L. Di-Silvio, Fabrication of 3D Bioprinted Bi-Phasic Scaffold for Bone–Cartilage Interface Regeneration, Biomimetics 8 (2023). https://doi.org/10.3390/biomimetics8010087.

[197] C.H. Chen, C.Y. Kuo, J.P. Chen, Effect of cyclic dynamic compressive loading on chondrocytes and adipose-derived stem cells co-cultured in highly elastic cryogel scaffolds, Int J Mol Sci 19 (2018). https://doi.org/10.3390/ijms19020370.

[198] J.T. Bingham, R. Papannagari, S.K. Van de velde, C. Gross, T.J. Gill, D.T. Felson, H.E. Rubash, G. Li, In vivo cartilage contact deformation in the healthy human tibiofemoral joint, Rheumatology 47 (2008) 1622–1627. https://doi.org/10.1093/rheumatology/ken345.

[199] C. Herberhold, S. Faber, T. Stammberger, M. Steinlechner, R. Putz, K.H. Englmeier, M. Reiser, F. Eckstein, In situ measurement of articular cartilage deformation in intact femoropatellar joints under static loading, 1999.

[200] W.Y. Lin, Y.H. Chang, H.Y. Wang, T.C. Yang, T.K. Chiu, S. Bin Huang, M.H. Wu, The study of the frequency effect of dynamic compressive loading on primary articular chondrocyte functions using a microcell culture system, Biomed Res Int 2014 (2014). https://doi.org/10.1155/2014/762570.

[201] Y. Liu, K. Tian, J. Hao, T. Yang, X. Geng, W. Zhang, Biomimetic poly(glycerol sebacate)/polycaprolactone blend scaffolds for cartilage tissue engineering, J Mater Sci Mater Med 30 (2019). https://doi.org/10.1007/s10856-019-6257-3.

[202] S. Critchley, E.J. Sheehy, G. Cunniffe, P. Diaz-Payno, S.F. Carroll, O. Jeon, E. Alsberg, P.A.J. Brama, D.J. Kelly, 3D printing of fibre-reinforced cartilaginous templates for the regeneration of osteochondral defects, Acta Biomater 113 (2020) 130–143. https://doi.org/10.1016/j.actbio.2020.05.040.

[203] J. Hauptstein, T. Böck, M. Bartolf-Kopp, L. Forster, P. Stahlhut, A. Nadernezhad, G. Blahetek, A. Zernecke-Madsen, R. Detsch, T. Jüngst, J. Groll, J. Teßmar, T. Blunk, Hyaluronic Acid-Based Bioink Composition Enabling 3D Bioprinting and Improving Quality of Deposited Cartilaginous Extracellular Matrix, Adv Healthc Mater 9 (2020). https://doi.org/10.1002/adhm.202000737.

[204] E.H. Schemitsch, Size Matters: Defining Critical in Bone Defect Size!, J Orthop Trauma 31 (2017) S20–S22. https://doi.org/10.1097/BOT.0000000000000978.

[205] B. Chen, Z. Lin, Q. Saiding, Y. Huang, Y. Sun, X. Zhai, Z. Ning, H. Liang, W. Qiao, B. Yu, K.W.K. Yeung, J. Shen, Enhancement of critical-sized bone defect regeneration by magnesium oxide-reinforced 3D scaffold with improved osteogenic and angiogenic properties, J Mater Sci Technol 135 (2023) 186–198. https://doi.org/10.1016/j.jmst.2022.06.036.

[206] A. Syahrom, M.R. Abdul Kadir, M.N. Harun, A. Öchsner, Permeability study of cancellous bone and its idealised structures, Med Eng Phys 37 (2015) 77–86. https://doi.org/10.1016/j.medengphy.2014.11.001.

[207] X. Hu, Z. Lin, J. He, M. Zhou, S. Yang, Y. Wang, K. Li, Recent progress in 3D printing degradable polylactic acid-based bone repair scaffold for the application of cancellous bone defect, MedComm - Biomaterials and Applications 1 (2022). https://doi.org/10.1002/mba2.14.

[208] G.L. Koons, M. Diba, A.G. Mikos, Materials design for bone-tissue engineering, Nat Rev Mater 5 (2020) 584–603. https://doi.org/10.1038/s41578-020-0204-2.

[209] C. Xu, Z. Liu, X. Chen, Y. Gao, W. Wang, X. Zhuang, H. Zhang, X. Dong, Bone tissue engineering scaffold materials: Fundamentals, advances, and challenges, Chinese Chemical Letters 35 (2024). https://doi.org/10.1016/j.cclet.2023.109197.

[210] B. Zhang, J. Li, L. He, H. Huang, J. Weng, Bio-surface coated titanium scaffolds with cancellous bone-like biomimetic structure for enhanced bone tissue regeneration, Acta Biomater 114 (2020) 431–448. https://doi.org/10.1016/j.actbio.2020.07.024.

[211] D. Carluccio, A.G. Demir, M.J. Bermingham, M.S. Dargusch, Challenges and Opportunities in the Selective Laser Melting of Biodegradable Metals for Load-Bearing Bone Scaffold Applications, Metall Mater Trans A Phys Metall Mater Sci 51 (2020) 3311–3334. https://doi.org/10.1007/s11661-020-05796-z.

[212] G. Turnbull, J. Clarke, F. Picard, P. Riches, L. Jia, F. Han, B. Li, W. Shu, 3D bioactive composite scaffolds for bone tissue engineering, Bioact Mater 3 (2018) 278–314. https://doi.org/10.1016/j.bioactmat.2017.10.001.

[213] L. Zhang, G. Yang, B.N. Johnson, X. Jia, Three-dimensional (3D) printed scaffold and material selection for bone repair, Acta Biomater 84 (2019) 16–33. https://doi.org/10.1016/j.actbio.2018.11.039.

[214] L.A. Bosworth, S. Downes, Physicochemical characterisation of degrading polycaprolactone scaffolds, Polym Degrad Stab 95 (2010) 2269–2276. https://doi.org/10.1016/j.polymdegradstab.2010.09.007.

[215] Y.Y. Liu, C. Intini, M. Dobricic, F.J. O'Brien, J. LLorca, M. Echeverry-Rendon, Collagen-based 3D printed poly (glycerol sebacate) composite scaffold with biomimicking mechanical properties for enhanced cartilage defect repair, Int J Biol Macromol 280 (2024). https://doi.org/10.1016/j.ijbiomac.2024.135827.

[216] C.M. Murphy, A. Schindeler, J.P. Gleeson, N.Y.C. Yu, L.C. Cantrill, K. Mikulec, L. Peacock, F.J. O'Brien, D.G. Little, A collagen-hydroxyapatite scaffold allows for binding and co-delivery of recombinant bone morphogenetic proteins and bisphosphonates, Acta Biomater 10 (2014) 2250–2258. https://doi.org/10.1016/j.actbio.2014.01.016.

[217] P. Nitti, S. Kunjalukkal Padmanabhan, S. Cortazzi, E. Stanca, L. Siculella, A. Licciulli, C. Demitri, Enhancing Bioactivity of Hydroxyapatite Scaffolds Using Fibrous Type I Collagen, Front Bioeng Biotechnol 9 (2021). https://doi.org/10.3389/fbioe.2021.631177.

[218] J.P. Gleeson, F. Lyons, S. Partap, F.J. O'Brien, COLLAGEN-HYDROXYAPATITE COMPOSITE SCAFFOLDS AS AN ALTERNATIVE TO AUTOGENOUS BONE GRAFTS, Orthopaedic Proceedings 94-B (2012) 8. https://doi.org/doi:10.1302/1358-992X.94BSUPP_XXXVIII.COA2011-008.

[219] T.J. Levingstone, C. Moran, H. V. Almeida, D.J. Kelly, F.J. O'Brien, Layer-specific stem cell differentiation in tri-layered tissue engineering biomaterials: Towards development of a single-stage cell-based approach for osteochondral defect repair, Mater Today Bio 12 (2021). https://doi.org/10.1016/j.mtbio.2021.100173.

[220] G.M. Cunniffe, G.R. Dickson, S. Partap, K.T. Stanton, F.J. O'Brien, Development and characterisation of a collagen nano-hydroxyapatite composite scaffold for bone tissue engineering., J Mater Sci Mater Med 21 (2010) 2293–2298. https://doi.org/10.1007/s10856-009-3964-1.

[221] C. Cheng, D. Shoback, Mechanisms Underlying Normal Fracture Healing and Risk Factors for Delayed Healing, Curr Osteoporos Rep 17 (2019) 36–47. https://doi.org/10.1007/s11914-019-00501-5.

[222] Q. Zhou, S. Lyu, A.A. Bertrand, A.C. Hu, C.H. Chan, X. Ren, M.J. Dewey, A.S. Tiffany, B.A.C. Harley, J.C. Lee, Stiffness of Nanoparticulate Mineralized Collagen Scaffolds Triggers Osteogenesis via Mechanotransduction and Canonical Wnt Signaling, Macromol Biosci 21 (2021). https://doi.org/10.1002/mabi.202000370.

[223] J.M. Sadowska, M. Ziminska, C. Ferreira, A. Matheson, A. Balouch, J. Bogle, S. Wojda, J. Redmond, A. Elkashif, N. Dunne, H.O. McCarthy, S. Donahue, F.J. O'Brien, Development of miR-26a-activated scaffold to promote healing of critical-sized bone defects through angiogenic and osteogenic mechanisms, Biomaterials 303 (2023). https://doi.org/10.1016/j.biomaterials.2023.122398.

[224] T.J. Levingstone, C. Moran, H. V. Almeida, D.J. Kelly, F.J. O'Brien, Layer-specific stem cell differentiation in tri-layered tissue engineering biomaterials: Towards development of a single-stage cell-based approach for osteochondral defect repair, Mater Today Bio 12 (2021). https://doi.org/10.1016/j.mtbio.2021.100173.

[225] X. Niu, Z. Xu, M. Di, D. Huang, X. Li, Bioreactor strategies for tissue-engineered osteochondral constructs: Advantages, present situations and future trends, Compos B Eng 259 (2023). https://doi.org/10.1016/j.compositesb.2023.110736.

[226] E. Solheim, J. Hegna, E. Inderhaug, Long-Term Survival after Microfracture and Mosaicplasty for Knee Articular Cartilage Repair: A Comparative Study Between Two Treatments Cohorts, Cartilage 11 (2020) 71–76. https://doi.org/10.1177/1947603518783482.

[227] E. V. Medvedeva, E.A. Grebenik, S.N. Gornostaeva, V.I. Telpuhov, A. V. Lychagin, P.S. Timashev, A.S. Chagin, Repair of damaged articular cartilage: Current approaches and future directions, Int J Mol Sci 19 (2018). https://doi.org/10.3390/ijms19082366.

[228] G. Liu, X. Wei, Y. Zhai, J. Zhang, J. Li, Z. Zhao, T. Guan, D. Zhao, 3D printed osteochondral scaffolds: design strategies, present applications and future perspectives, Front Bioeng Biotechnol 12 (2024). https://doi.org/10.3389/fbioe.2024.1339916.

[229] X. Lin, Y. Zhang, J. Li, B.G. Oliver, B. Wang, H. Li, K.T. Yong, J.J. Li, Biomimetic multizonal scaffolds for the reconstruction of zonal articular

cartilage in chondral and osteochondral defects, Bioact Mater 43 (2025) 510–549. https://doi.org/10.1016/j.bioactmat.2024.10.001.

[230] H. Chen, J. Huang, X. Li, W. Zhao, Y. Hua, Z. Song, X. Wang, Z. Guo, G. Zhou, W. Ren, Y. Sun, Trilayered biomimetic hydrogel scaffolds with dual-differential microenvironment for articular osteochondral defect repair, Mater Today Bio 26 (2024). https://doi.org/10.1016/j.mtbio.2024.101051.

[231] D.L. Dorcemus, H.S. Kim, S.P. Nukavarapu, Gradient scaffold with spatial growth factor profile for osteochondral interface engineering, Biomedical Materials (Bristol) 16 (2021). https://doi.org/10.1088/1748-605X/abd1ba.

[232] S. Davis, M. Roldo, G. Blunn, G. Tozzi, T. Roncada, Influence of the Mechanical Environment on the Regeneration of Osteochondral Defects, Front Bioeng Biotechnol 9 (2021). https://doi.org/10.3389/fbioe.2021.603408.